AD-A242 956

ALUMINUM ALLOYS FOR ALS CRYOGENIC TANKS: COMPARATIVE MEASUREMENTS OF CRYOGENIC MECHANICAL PROPERTIES OF A1-Li ALLOYS AND ALLOY 2219

R.P. Reed
P.T. Purtscher
N.J. Simon
J.D. McColskey
R.P. Walsh
J.R. Berger
E.S. Drexler
R.L. Santoyo

DTIC
ELECTE
NOV 1 1991
S
C
D

October 1991

Final Report

91-14641

PHILLIPS LABORATORY
Propulsion Directorate
AIR FORCE SYSTEMS COMMAND
EDWARDS AIR FORCE BASE CA 93523-5000

91 10 31 010

NOTICE

FOREWORD

This final report was submitted on completion of this phase of JON: 4SL13148 by the OLAC PL/RCC Branch, at the Phillips Laboratory (AFSC), Edwards AFB CA 93523-5000. OLAC PL Project Manager was Bruce Pham.

This report has been reviewed and is approved for release and distribution in accordance with the distribution statement on the cover and on the DD Form 298.

BRUCE T. PHAM
Project Manager

MICHAEL T. HUGGINS
Acting Chief, Components Branch

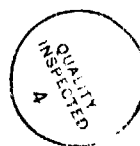WAYNE L. PRITZ
Deputy Director,
Component Engineering Division

RANNEY G. ADAMS
Public Affairs Director

REPORT DOCUMENTATION PAGE

Form Approved
OMB No. 0704-0188

1. AGENCY USE ONLY (Leave blank)	2. REPORT DATE	3. REPORT TYPE AND DATES COVERED
	October 1991	Final 08/89 to 03/90

4. TITLE AND SUBTITLE	5. FUNDING NUMBERS
Aluminum Alloys for ALS Cryogenic Tanks: Comparative Measurements of Cryogenic Mechanical Properties of Al-Li Alloys and Alloy 2219	MIPR-PL-99011 PR-45L1 TA-3148

6. AUTHOR(S)

R.P. Reed; P.T. Purtscher; N.J. Simon; J.D. McColskey;
R.P. Walsh; J.R. Berger; E.S. Drexler; R.L. Santoyo

7. PERFORMING ORGANIZATION NAME(S) AND ADDRESS(ES)	8. PERFORMING ORGANIZATION REPORT NUMBER
National Institute of Standards and Technology 325 Broadway Boulder, Colorado 80303	

9. SPONSORING/MONITORING AGENCY NAME(S) AND ADDRESS(ES)	10. SPONSORING/MONITORING AGENCY REPORT NUMBER
Phillips Laboratory Edwards AFB, CA 93523-5000	PL-TR-91-3073

11. SUPPLEMENTARY NOTES

COSATI CODES: 11/06; 12/06

12a. DISTRIBUTION/AVAILABILITY STATEMENT	12b. DISTRIBUTION CODE
Public Release, Distribution is Unlimited	

13. ABSTRACT (Maximum 200 words)

Tensile and plane-strain fracture toughness properties were obtained at cryogenic temperatures to compare the Al-Li alloys 8090, 2090, and WL049 and alloy 2219 in various tempers and specimen orientations. The strongest alloy at very low temperatures is WL049-T851, which is about 10% stronger than 2090-T81. Both alloys are considerably stronger than 2219-T87. Alloy 2090-T81 is tougher in the in-plane orientations (about 50%) than WL049-T851 at low temperatures; the higher in-plane toughness is attributed to the presence of less constituent particles and the tendancy to crack out-of-plane or delaminate at low temperatures. This delamination tends to divide the moving crack, thus separating it into smaller regions where plan stress (rather than plane strain) conditions are conducive to increased toughness. Thus, a dichotomy: reduced toughness in the through-thickness or out-of-plane orientations leads to increased toughness in the in-plane orientations. In service, a leak in the tank is considered failure, and a leak will be caused by a crack in the panels of the tankage growing through the panel thickness. To measure the resistance to crack growth under these conditions, surface-flawed panel tests are recommended.

14. SUBJECT TERMS Aluminum – Lithium Alloys, Cryogenic Mechanical Properties, Alloy 2219, Tensile Properties, Fracture Toughness, Delaminations, Surface Flaw	15. NUMBER OF PAGES 146
	16. PRICE CODE

17. SECURITY CLASSIFICATION OF REPORT	18. SECURITY CLASSIFICATION OF THIS PAGE	19. SECURITY CLASSIFICATION OF ABSTRACT	20. LIMITATION OF ABSTRACT
Unclassified	Unclassified	Unclassified	SAR

TABLE OF CONTENTS

LIST OF FIGURES

TABLES

1. EXECUTIVE SUMMARY

The cryogenic mechanical-property data presented here were obtained in a National Institute of Standards and Technology (NIST) program to assess new high-strength Al-Li alloys for use in the cryogenic tankage of the Advanced Launch System (ALS). Other parts of the program are discussed in the reports: "Aluminum Alloys for Cryogenic Tanks: Oxygen Compatibility (Volumes 1 and 2)[1]" and "Review of Cryogenic Mechanical and Thermal Properties of Al-Li Alloys and Alloy 2219".[2]

Tensile and fracture toughness were obtained at cryogenic temperatures to compare the Al-Li alloys 8090, 2090, and WL049, and alloy 2219 in various tempers and specimen orientations. The strongest alloy at very low temperatures is WL049-T851, which is about 10% stronger than 2090-T81. Both alloys are considerably stronger than 2219-T87. Alloy 2090-T81 is tougher (about 50%) than WL049-T851 at low temperatures; the higher toughness is attributed to the presence of fewer constituent particles and the tendency to delaminate at low temperatures. This delamination divides the moving crack, thus separating it into smaller regions where plane stress (rather than plane strain) conditions are conducive to increased toughness. Thus, a dichotomy: reduced toughness in the S orientations (crack running in the plane of the plate through the pancake-like grain structure) leads to increased toughness in the T-L and L-T orientations (crack running in the longitudinal or transverse rolling directions, normal to the plane of the plate)

In ALS cryogenic-tankage design, a leak-before-break failure criterion is used. A leak will be caused by a crack in the panels of the tankage growing through the panel thickness. To measure the resistance to crack growth under these conditions, surface-flawed panel tests are recommended. The plane-strain conditions of the compact-tension specimens (used for this program) are not replicated by panel tests; instead nearly plane stress conditions may be achieved. Since toughness under plane stress conditions more closely relates to tensile strength, WL049 is expected to compare more favorably to 2090 in surface-flawed panel tests. Such testing will permit comparison of the two alloys under conditions closely simulting service and should permit analysis of the role of intergranular delaminations and state of stress.

1

2. INTRODUCTION

The mechanical property studies reported here are part of a broader National Institute of Standards and Technology (NIST) program to assess new high-strength Al-Li alloys for use in the cryogenic tankage of the Advanced Launch System (ALS). This program is sponsored by the Air Force Systems Command, Astronautics Laboratory, Edwards Air Force Base, with Bao Nguyen and, more recently, Bruce Pham, Task Manager. It is part of the Materials and Processes Validation (3101) of the Structures, Materials, and Manufacturing (3000) portion of the ALS Advanced Development Program.

Selected mechanical properties of high-strength Al alloys for use in ALS cryogenic tankage have been measured. Various tempers of new commercial-grade Al-Li alloys (8090, 2090, and WL049) and the baseline alloy (2219), that was the structural alloy used in the cryogenic tankage of the space shuttle, were included in this program.

Program objectives are: (1) to provide tensile and fracture toughness data at room and cryogenic temperatures to use as criteria for alloy selection and, (2) to assess the influence of material anisotropy and temper on low temperature tensile and fracture toughness properties.

The test temperatures were 295 K (room temperature), 76 K (liquid nitrogen), 20 K (gaseous helium), and 4 K (liquid helium). Tensile and fracture toughness data were obtained in the T-L (longitudinal), L-T (transverse), S-T (short transverse) and S-L (short longitudinal) orientations. Both compact tension C(T) and chevron-notched short-bar techniques and associated specimens were used to measure fracture toughness. Additional tensile measurements were conducted to obtain data in an orientation 45° to the T-L or L-T orientations.

In another report,[2] the data obtained from this study are compared to other data from other programs. When making comparisons with previous data, one must realize that the development of Al-Li alloys is now in progress; therefore, it is likely that current alloys have improved quality compared to past alloys and may exhibit improved mechanical properties.

2

3. MATERIALS

A summary of the alloys, supplies, plate dimensions, and dates when the materials were received is found in Table 3.1. All alloys and tempers (8090-T8771, 8090-T8151, 8090-T3, 2090-T81, WL049-T851, WL049-T651, WL049-T351, 2219-T87, 2219-T8151, 2219-T37) were supplied as 13 mm (1/2 in) thick plate; 2090-T81 was also obtained as 19 mm (3/4 in) thick plate.

The chemical compositions of the alloys, as furnished by the suppliers, are summarized in Table 3.2. Compositions of 8090, 2090, and 2219 fall within the Aluminum Association specifications for each alloy. At the time of preparation of this report, a generic specification for Weldalite 049 was not available and the alloy was termed WL049; a generic specification of x2095 has now been adopted for this alloy.

The two 8090-T3 alloy plates (3516-301A and 3518-302A) have a similar pancake-grain morphology and size (Figure 3.1). The average grain length in the rolling plane is 0.6 mm, and the average grain thickness is about 0.02 mm. Some recrystallization is evident, but, in general, the structures of these alloys show unrecrystallized grains with equiaxed subgrain sizes ranging from 0.01 to 0.05 mm.

In this report, the term constituent particles is used to identify all precipitates and dispersoids that are large enough to be observed on a polished or etched surface with an optical microscope. Most of the precipitates have been deliberately added to provide increased strength and disperoids have been added to restrict grain growth. If present, nonmetallic particles, such as oxides, are also included. There is no attempt here to distinguish between these particles.

The distribution of constituent particles in the alloys is sometimes indicative of the as-cast structure. The constituent particles do not necessarily coincide with the grain boundary traces on the rolling plane. However, on planes perpendicular to the rolling plane, there is a much stronger correlation between the positions of grain boundaries and particles. This observation is generally valid for the Al-Li alloys covered in this report.

The grain structure of 8090-T8771 is shown in Figure 3.2. A finer structure is evident and apparent recrystallized grains are shown. However, the pancake-like appearance of grains is preserved.

Alloy 2090-T81 has a much larger grain size than alloys 8090, 2219, or WL049. The length of the grains ranges from approximately 1 to 3 mm (Figure 3.3). Also, from Figure 3.3, it is clear that the grains of the 13 mm (1/2 in) 2090 plate material are much thicker (0.2 mm) than those observed in the 19 mm (3/4 in) plate (0.1 mm). Small recrystallized grains are located almost exclusively at the boundaries between grains in the 13 mm (1/2 in) plate. The 19 mm (3/4 in) plate material has some recrystallization within the grains. The subgrain boundaries in both plates are not visible throughout much of the structure. The distribution of constituent particles indicates that the solidification structure had more closely spaced dendrites than alloy 8090.

Table 3.1 Inventory of Al and Al-Li Plate Material.

Date Received	Supplier	Alloy	Quantity	Plate Dimensions, cm	Lot Number
5/29/89	ALCAN	8090-T3	5	25 x 25 x 1.27	3508302A 3510301A 3516301A 3518302A 3519301A
7/12/89	Kaiser	2219-T851	4	122 x 122 x 1.27	429881
7/12/89	Kaiser	2219-T37	4	122 x 122 x 1.27	486341
8/10/89	ALCOA	2090-T81	1	122 x 244 x 1.27	103301
8/10/89	ALCOA	2090-T81	1	122 x 244 x 1.91	103299
9/22/89	ALCAN	8090-T8771	4	91.4 x 163 x 1.27	3503302B
10/11/89	ALCAN	8090-T8151	3	92 x 152 x 1.27	9A4552 9A4591
11/14/89	ALCOA	2219-T87	1	30.5 x 30.5 x 1.27	294592
11/27/89	Reynolds (Lot 1)	WL049-T851	1	122 x 122 x 1.27	0387250A
3/09/90	Reynolds (Lot 2)	WL049-T851	1	30.5 x 30.5 x 1.27	9002311A
3/14/90	NASA	2219-T87	4	30.5 x 30.5 x 2.54	484881

Table 3.2 Compositions of Al-Li Alloys and Alloy 2219, wt%

Alloy	Cu	Li	Mg	Zr	Si	Fe	Ti	Cr	Zn	Ag	Ni	B	Mn
8090-T3	1.18	2.23	0.63	0.110	0.02	0.040	0.024	0.001	0.02	--	0.004	0.0001	--
8090-T8151	1.20	2.36	0.70	0.110	0.02	0.060	--	--	--	--	--	--	--
8090-T3771	1.21	2.36	0.68	0.110	0.02	0.063	0.028	0.002	0.04	--	0.004	--	--
2090-T81 12.7 mm	2.70	2.30	0.03	0.120	--	0.080	0.190	<0.000	0.01	--	0.010	<0.0000	<0.00
2090-T81 19.1 mm	2.85	2.30	0.05	0.100	--	0.070	0.130	<0.000	0.02	--	0.010	0.0007	<0.00
WL049-T851 Lot 1	4.72	1.28	0.42	0.120	0.02	0.030	0.020	--	0.02	0.35	0.010	--	<0.00
WL049-T851 Lot 2	4.36	1.25	0.39	0.140	0.03	0.070	0.020	--	0.02	0.35	<0.010	--	<0.00
WL049-T651	4.72	1.28	0.42	0.120	0.02	0.030	0.020	<0.000	0.02	0.35	0.010	--	<0.00
2219-T87 Lot No. 294592	5.87	--	0.01	0.220	0.07	0.010	0.040	<0.000	--	--	<0.000	--	0.23
2219-T87 Lot No. 484881	5.71	--	<0.00	0.150	0.07	0.020	0.030	0.0100	--	--	<0.000	--	0.30
2219-T851	5.71	--	--	0.080	0.04	0.020	0.044	0.1800	--	--	0.016	--	0.24
2219-T37	5.72	--	--	0.028	0.04	0.018	0.030	0.0200	--	--	<0.000	--	0.22

4
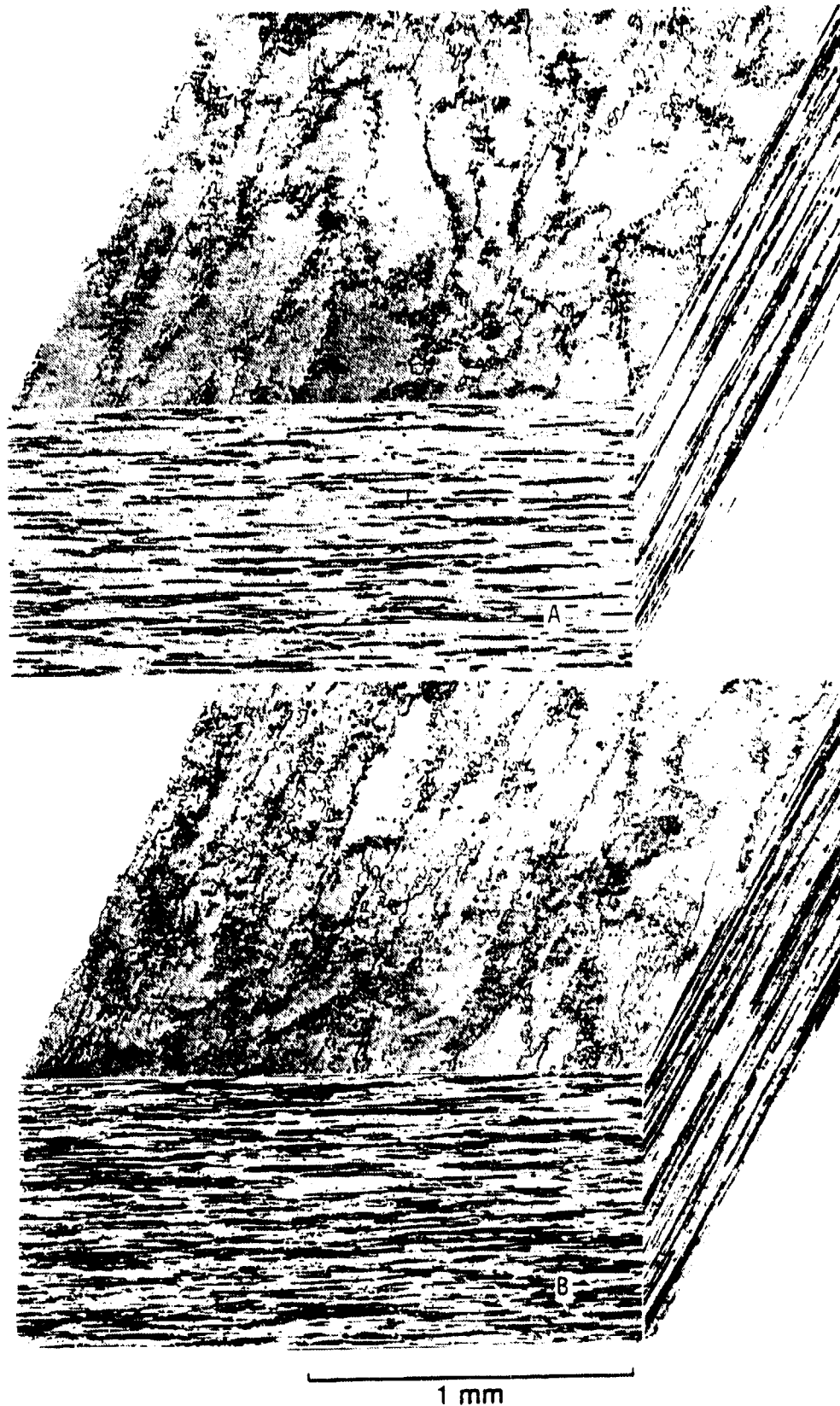
Figure 3.1 The grain size and morphologies of the two 8090-T3
13 mm (1/2 in) plates used to make test specimens were
similar: (a) 316 301A, (b) 3518 302A.
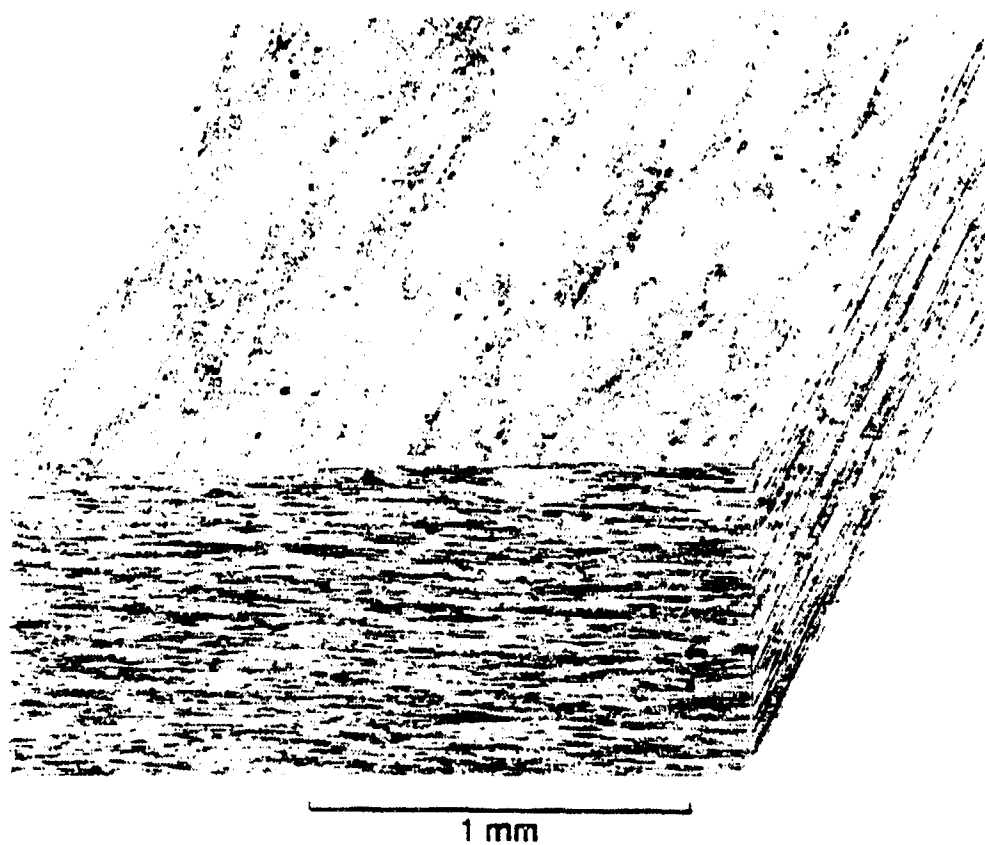
Figure 3.2   The grain size and morphology of 8090-T8771.

Figure 3.3   The grain size and morphology of the 2090-T81
            13 mm (1/2 in) plate (a) and 19 mm (3/4 in) plate (b).

The microstructures of the WL049 tempers (Figures 3.4 - 3.6) consist of large pancake grains that contain many small recrystallized grains. The pancake-grain sizes in the WL049-T851 (Lot 1 and Lot 2) temper are 3 to 5 mm long and up to 1 mm wide in the rolling plane. The WL049-T651 temper has a smaller pancake-grain size, often less than 1 mm long and 0.5 mm wide in the rolling plane. These materials also differ in recrystallized grain size and constituent particle content. The recrystallized grain sizes for the WL049-T651 and WL049-T851 (Lot 2) tempers were normally less than 10 μm. In the WL049-T851 (Lot 1) temper, areas of recrystallized grains have sizes greater than 100 μm (Figure 3.8).

The 2219 alloys (T851, T37) have grain lengths ranging from 0.05 to 0.3 mm in the rolling plane (Figure 3.7). The thickness of the grains is approximately equal to half their length (average grain thickness is 0.05 mm), so, compared to the Al-Li alloys, these grains are only slightly oriented in a pancake-like structure. The constituent particles are more randomly distributed in the 2219 alloy than in the Al-Li alloys and are usually not located at grain boundaries.

The as-received microstructure of the 2219-T87 alloy and temper has a grain size and morphology similar to that reported for the 2219-T851 and T37 tempers. The grains are slightly elongated in the rolling direction with lengths up to 0.3 mm and widths normally less than 0.05 mm (Figure 3.8).

A summary of estimated average grain sizes in the longitudinal (L), transverse (T), and through-thickness (S) orientation is given in Table 3.3. Alloy 2219 has smaller grains in the L and T orientation, but equivalent grain size in the S orientation.

Constituent particles were counted using an optical microscope (400X) equipped with an image analysis system. The procedure used included (1) polishing to a 1-μm diamond finish and light attack polishing in a dilute NaOH solution and 0.30-μm Al_2O_3; (2) measuring particles located in consecutive fields along paths perpendicular to the rolling direction (100 fields per alloy, 2-mm^2 total area); (3) approximating particle size using the area of each particle measured and assuming a circular shape to calculate a diameter; (4) separating particles into 10 bins based on diameter; and (5) approximating particle volumes using mean diameters for each bin and assuming a spherical particle shape.

The particle counts collected for the alloys with T8 tempers are given in Table 3.4. Alloy 2090-T81 has the fewest particles, followed by the T8151 and T8771 tempers of alloy 8090, WL049-T851 (Lot 2), 2219-T87 and, finally, WL049-T851 (Lot 1), with the most particles. A ranking by particle volume produces the same order. The distributions in particle sizes broaden as the particle content of the alloys increases; alloys having higher numbers of particles also have more large particles present in their microstructures. The most notable change in particle content for a given alloy type is the reduction in particle content for the second lot of WL049-T851.

8

Figure 3.4 The grain size and morphology of the WL049-T351 (a)
and WL049-T651 (b).

1 mm
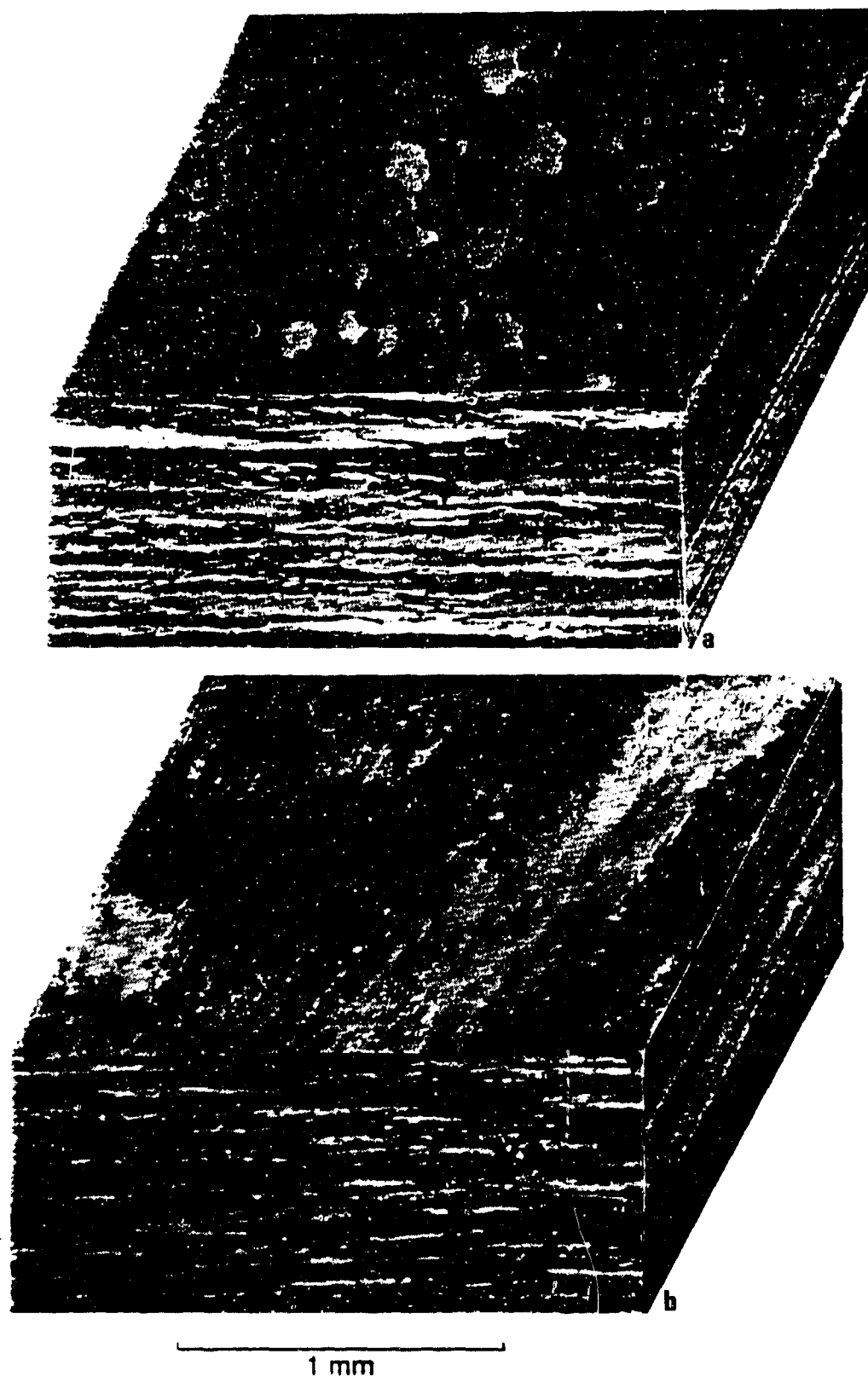
Figure 3.5   The grain size and morphology of (a) the WL049–T851
(Lot 1) temper and (b) the WL049–T651 temper.

10
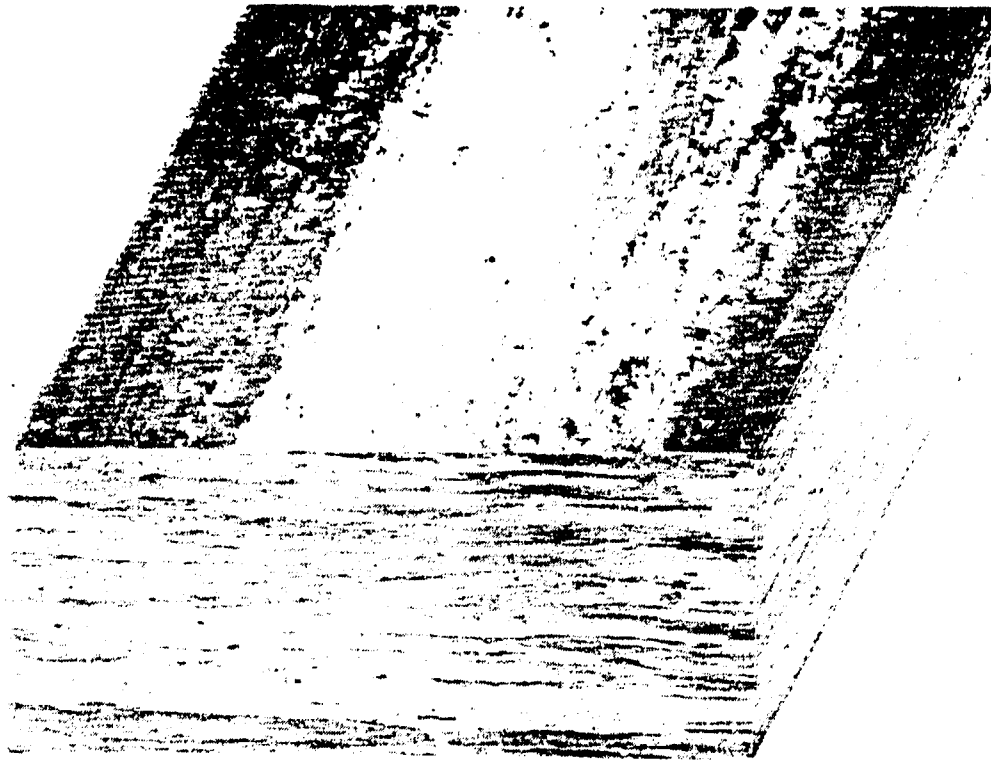
Figure 3.6   The grain size and morphology of WL049-T851 (Lot 2).
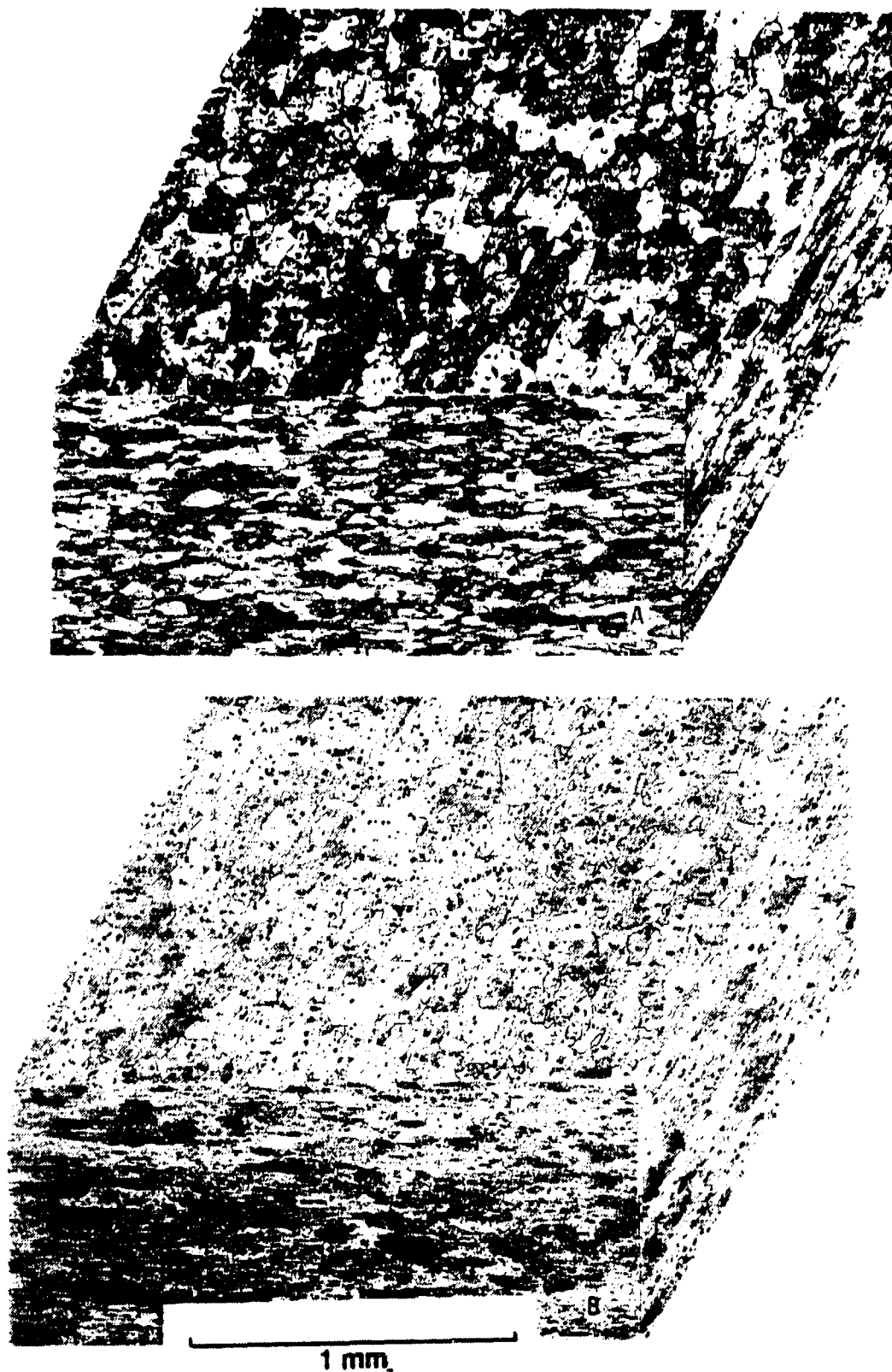
Figure 3.7   The grain size and morphology of the (a) 2219–T37
and (b) 2219–T851 plates.

12

Figure 3.8 The grain size and morphology of 2219–T87 alloy.

13

Table 3.3 Summary of Grain Size and Hardness Data

Alloy	Average Grain Size, μm			Hardness, R_b
	L	T	S	
8090-T3	600	380	20	35
8090-T8151	-	-	-	70
8090-Td771	-	-	-	74
2090-TS1 (12 mm)	~2000	1400	200	85
2090-T81 (19 mm)	~2000	1400	100	76
WL049-T351	~1000	1000	40	76
WL049-T651	~800	400	25	89
WL049-T851 (Lot 1)	~4000 to 100	800 to 100	30	88
WL049-T851 (Lot 2)	~4000	800	35	86
2219-T37	220	140	40	71
2219-T851	220	130	40	73
2219-T87	220	120	40	77

Table Table 3.4 Constituent Particle Counts on Al-Li Alloys and Alloy 2219.

Second Phase Particle Size Range, μm	Number of Second Phase Particles							
	8090-T8771	8090-T8151	2090-T81 13-mm (0.5-in) plate	2090-T81 19-mm (0.75-in) plate	WL049-T851 Lot 1	WL049-T851 Lot 2	2219-T87 (Lot No. 294592)	2219-T851
1-2	2,433	1,536	408	736	10,018	4,294	4,458	4,740
2-3	639	626	460	386	4,772	633	753	1,452
3-4	203	224	190	144	1,452	166	351	436
4-5	119	100	82	67	555	75	188	184
5-6	49	39	30	37	249	57	133	105
6-7	19	11	16	22	154	34	108	95
7-8	17	14	9	6	97	17	77	82
8-9	11	5	2	2	56	11	59	41
Total Count	3,490	2,555	1,697	1,400	17,415	5,287	6,127	7,135
Total Volume	37,016	29,714	22,876	20,798	216,110	40,795	100,366	99,899
Undersized*	6,358	2,496	2,998	766	9,000	8,913	23,531	27,122
Oversized**	12	19	4	0	68	17	*114	175

*inclusion size < 1 μm
**Inclusion size > 9 μm

14

We place little significance on the undersized particle counts (< 1 μm) because of the measurement errors possible for these small sizes. The variations in the oversized counts (> 9 μm), however, indicate significant differences in the alloys. For example, the frequency of particles with diameters greater than 9 μm is highest for alloy 2219. The values for total particle counts and volume, reported in Table 3.4 do not include data from the over- and undersized bins.

4. HARDNESS

Microhardness tests were conducted on both oxygen-compatibility specimens and in the through-thickness direction of alloy plates.

Vickers microhardness tests were conducted on samples of alloys 8090-T3, 2090-T81 (12.7 mm thick plate), 2219-T851 and 2219-T37 that had been machined into specimens for oxygen-compatibility tests.[1] Each sample was sectioned as shown in Figure 4.1 and mounted in epoxy. Hardness traverses were made across the specimen's top surface and across the specimen at approximately one-half of the thickness. For purposes of this discussion, the surface traverse is called "surface" and the mid-thickness traverse is called the "profile."

The variation in Vickers hardness with position is illustrated in Figure 4.2-4.5. In each figure the values from the "profile" traverse are above those from the "surface" traverse. All graphs have been plotted with a common y-axis so direct comparisons between the alloys can easily be made. Averages of standard deviations (S.D.'s) for the hardness of each alloy are summarized in Table 4.1.

The 2090-T81 alloy was the hardest of the four alloys. The two tempers of 2219 had lower hardness than the 2090-T81 but were higher than the 8090-T3. Under identical static loading conditions, therefore, we can expect the 8090-T3 alloy to undergo the most deformation with smaller deformations occurring in the 2090 and 2219 alloys. The dynamics of impact loading require consideration of the relative resiliencies of the alloys and absorbed energy to predict dynamic indentation behavior.

Microhardness profiles were obtained in the through-thickness direction for 8090-T3, 2090-T81, and 2219-T851 alloys using Vickers equipment with a 10 g load. Specimens were polished, on edge, and hardness indentations obtained at approximately 0.02 mm intervals from one as-received surface inward. The hardness remains constant for 2219-T851, independent of the depth. Data are plotted in Figure 4.6. In the Al-Li alloys, the hardness is less on the surface and increases to larger values as measurements are taken moving away from the as-received surface. The increase of hardness interior to the surface was found for all Al-Li alloys that were measured. At depths between 0.1 and 0.3 mm from the surface the hardness leveled off, and remained constant (within about ± 2 Vickers numbers) at greater depths. The reduction of hardness near the surface is thought to be associated with depletion of lithium.

A summary of Rockwell B hardness measurements for all alloys and tempers in the program is included in Table 3.3.

16
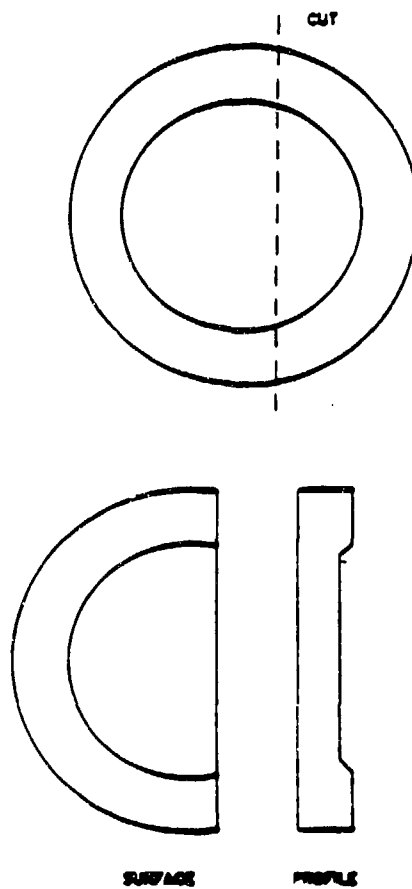
Figure 4.1 Sectioning of impact specimen for hardness testing.
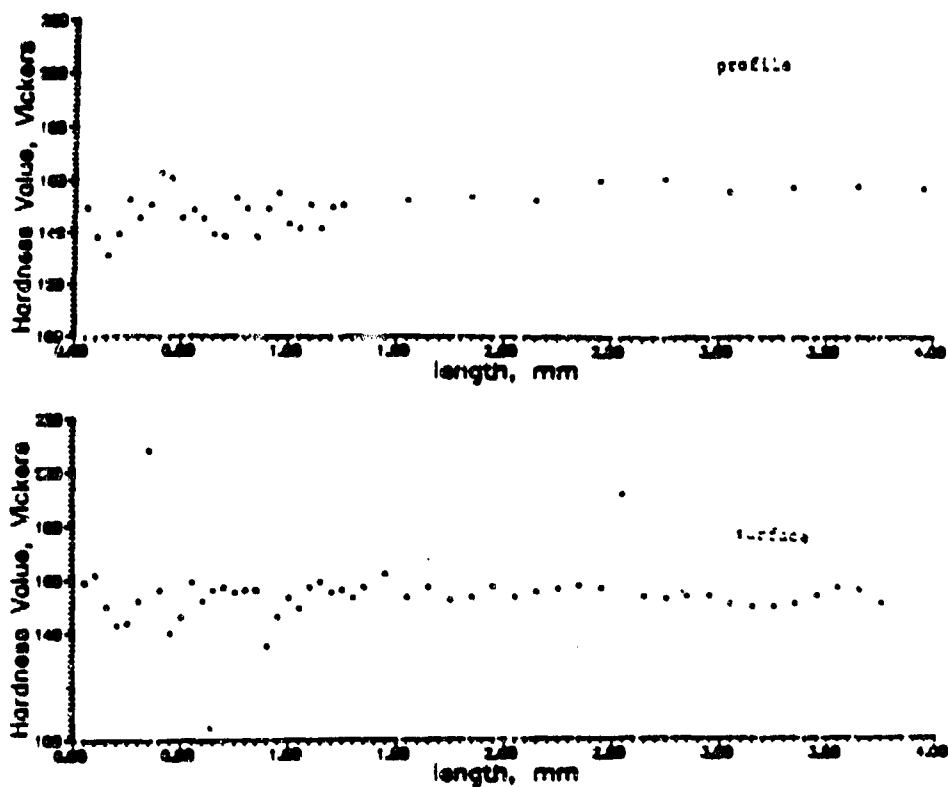
Figure 4.2 Hardness profiles: Nonimpacted 8090—T3 specimens.
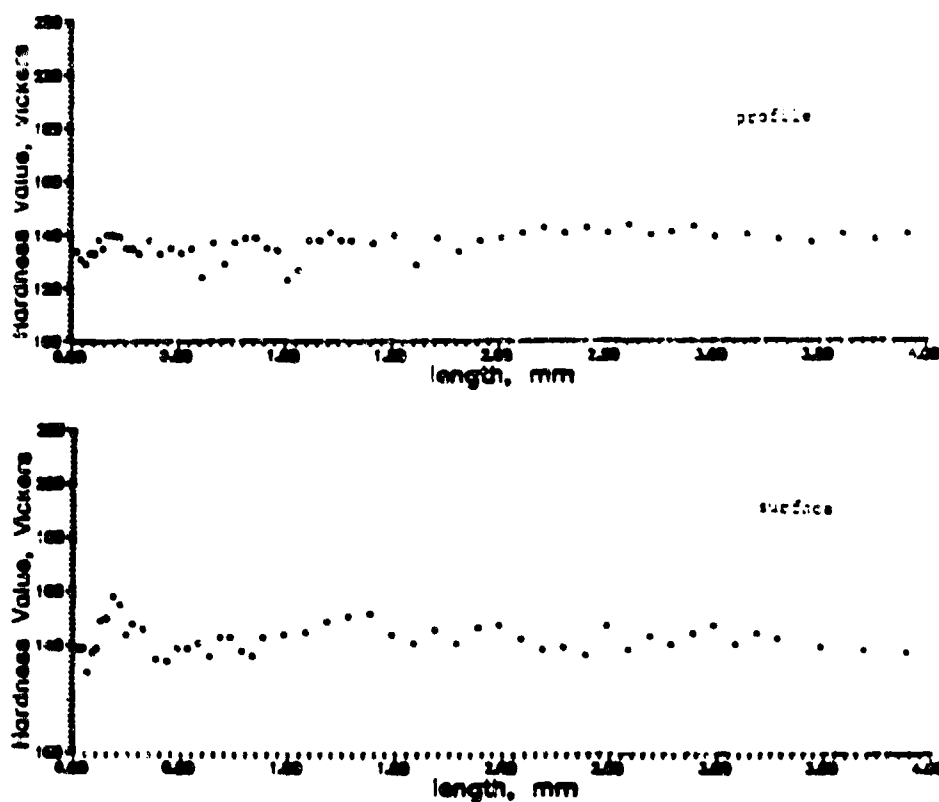
Figure 4.3 Hardness profiles: Nonimpacted 2090—T81 specimens.

18
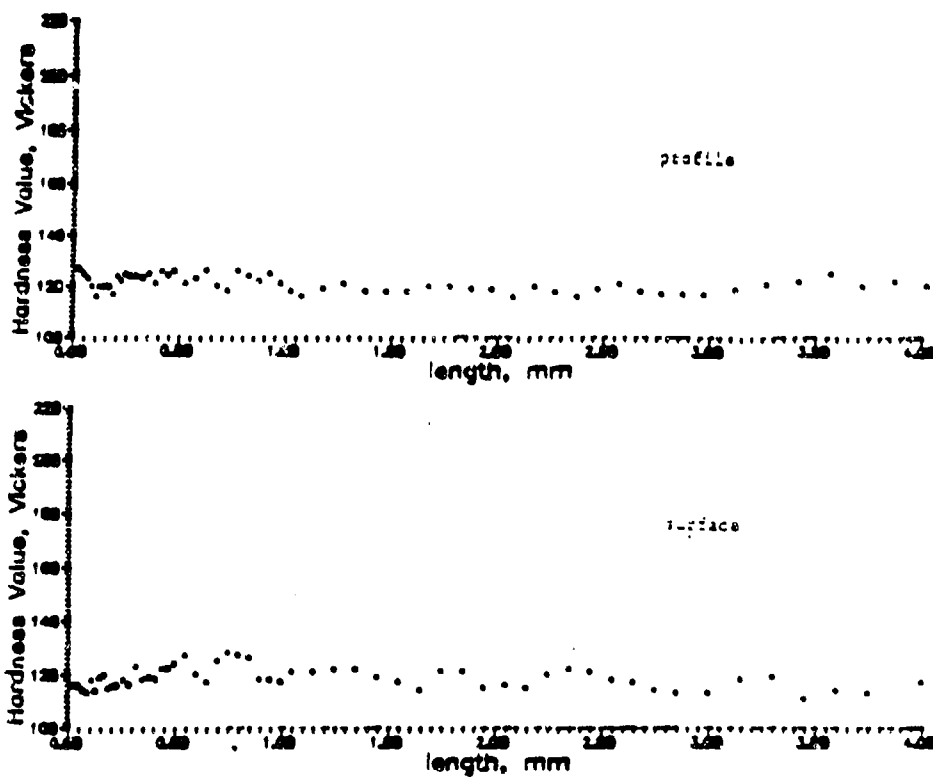
Figure 4.4 Hardness profiles: Nonimpacted 2219–T851 specimens.
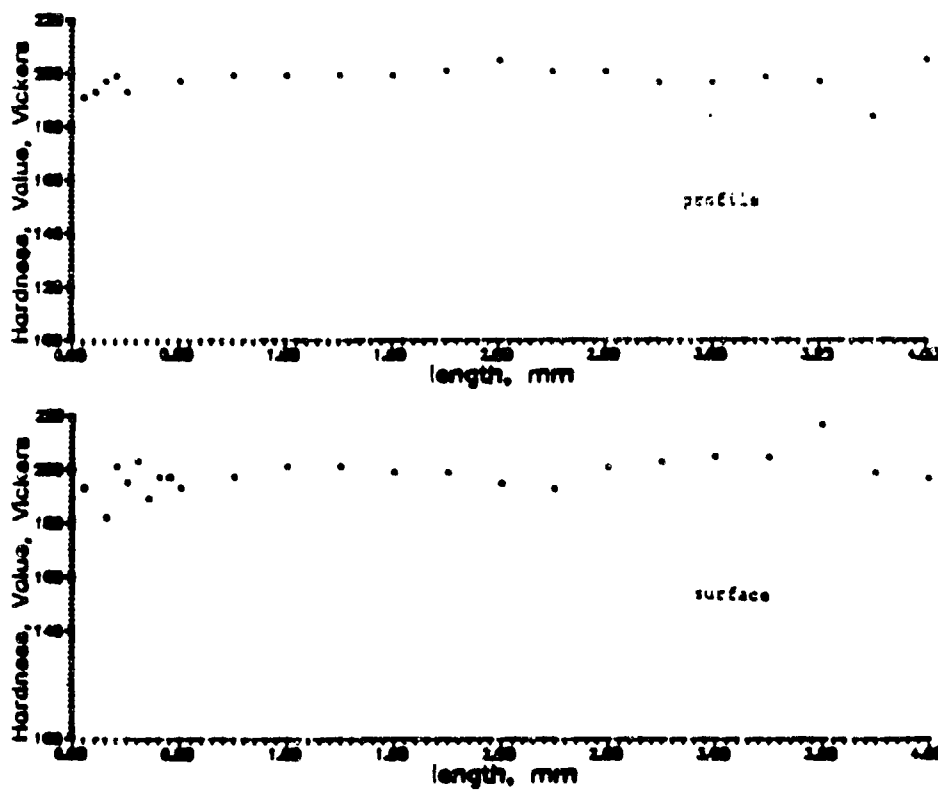
Figure 4.5 Hardness profiles: Nonimpacted 2219–T37 specimens.

Table 4.1   Vickers Hardness (10g load) Tests on Nonimpacted
Compatibility Specimens.

ALLOY	8090-T3		2090-T81 (19 mm plate)	
	Profile	Surface	Profile	Surface
Average	120.9	118.5	197.6	198.3
S.D.	3.0	3.9	4.6	6.5
Specimen Thickness (mm)	1.6	1.6	3.2	3.2
ALLOY	2219-T851		2219-T37	
	Profile	Surface	Profile	Surface
Average	148.8	154.8	136.6	142.9
S.D.	7.5	10.5	4.5	5.4
Specimen Thickness (mm)	1.6	1.6	1.6	1.6

MICROHARDNESS
Through thickness profiles
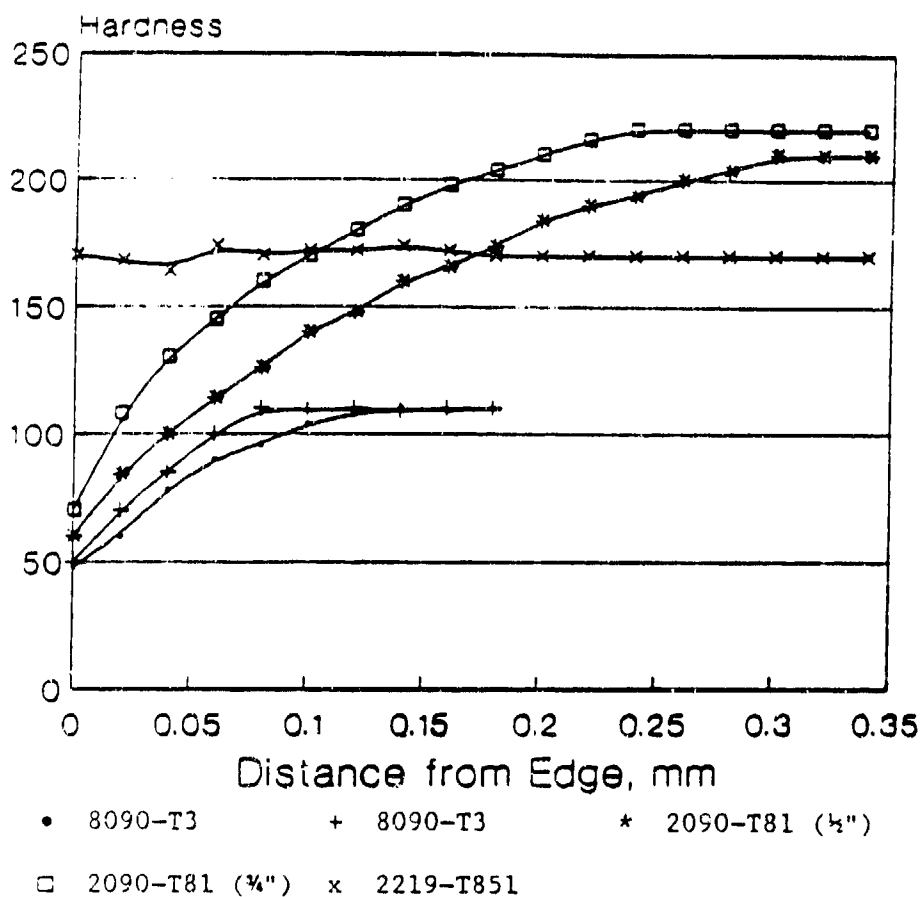
Figure 4.6 Microhardness, through-thickness of alloys 8090-T3
(• and +), 2090-T81, 12.7 mm thick plate (* and ▫),
and 2219-T851 (x). A Vickers machine with a 10g
load was used.

5. MECHANICAL PROPERTY TEST PROCEDURES

Three types of mechanical property tests were conducted: tensile, compact-tension fracture toughness, and chevron-notched short-bar fracture toughness. The procedures used in these tests are discussed below. For all alloys, tempers, and orientations, at least two tests were conducted at each temperature.

5.1. Tensile

Displacement-controled tensile tests were carried out at 295 K (ambient), 76 K (liquid nitrogen), 20 K (cold helium gas), and 4 K (liquid helium). At room temperature, tests were conducted following ASTM E8 standards. Tests at low temperatures conformed to the draft modifications (Tensile Testing of Structural Alloys at Liquid Helium Temperature) that the ASTM is in the process of adopting.

Round tensile specimens with a 6 mm (0.25 in) diameter by 38 mm (1.50 in) long reduced gage section were machined with the tensile axis oriented either transversely, longitudinally, or 45° to the plate rolling direction. All specimens were cut so that the gage section of the specimen was centered within the plate thickness. Specimen configuration is shown in Figure 5.1(a). Specimens were also produced to measure the through-thickness strength. Since most plates were only 12.7 mm (0.5 in) thick, the length of the reduced section of these specimens was limited to 7 mm (0.275 in). A drawing of this specimen is shown in Figure 5.1(b).

The cryostat is described by Reed and Walsh.[3] Temperatures of 20 K were achieved by testing in helium gas and automatically adjusting the gas flow and the heater input at the specimens grips with temperature controllers. Silicon diodes inserted into small drilled holes in both specimen grips permitted digital readout and control of temperatures at both the upper and lower grips. By these means, specimen temperature was maintained within $\pm$ 1 K during testing at 20 K. During discontinuous load drops while testing at 4 and 20 K, the specimen surface temperature increases. Specimen temperature returned to the desired control temperature during subsequent elastic deformation to the prior flow stress.

The specimens were loaded, using a screw-driven machine, at a low strain rate of 8.8×10^{-5} s^{-1} at constant temperature. Two types of strain-gage extensometers, developed for use at low temperatures, were used for most of these measurements. One set, capable of sensitivities of 10^{-5}, has three flexing Al beams, each with strain gages. Sensing of elongations over 30% were achieved with a single-beam (ring-type) extensometer. Four 350 ohm strain gages were mounted to the beam and wired in a Wheatstone bridge configuration. A 5-V dc power supply was used to adjust excitation. Elongations obtained with this extensometer agreed very closely with measurements before and after failure using scribed gage lengths on the specimens. The estimated measurement inaccuracies are Young's modulus, $\pm$ 3%; yield strength, $\pm$ 2%; ultimate strength, $\pm$ 1%; and elongation, $\pm$ 3%.
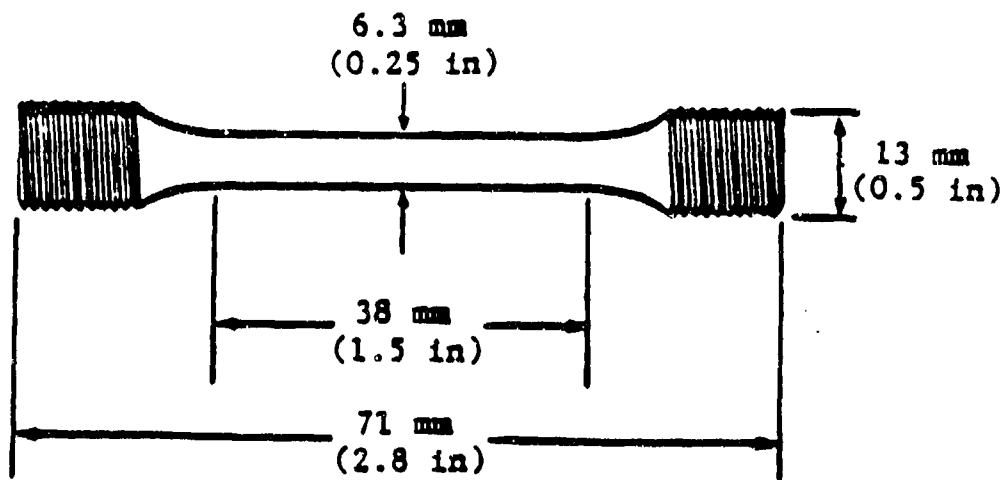
Figure 5.1(a)   Tensile specimen for L and T orientations.
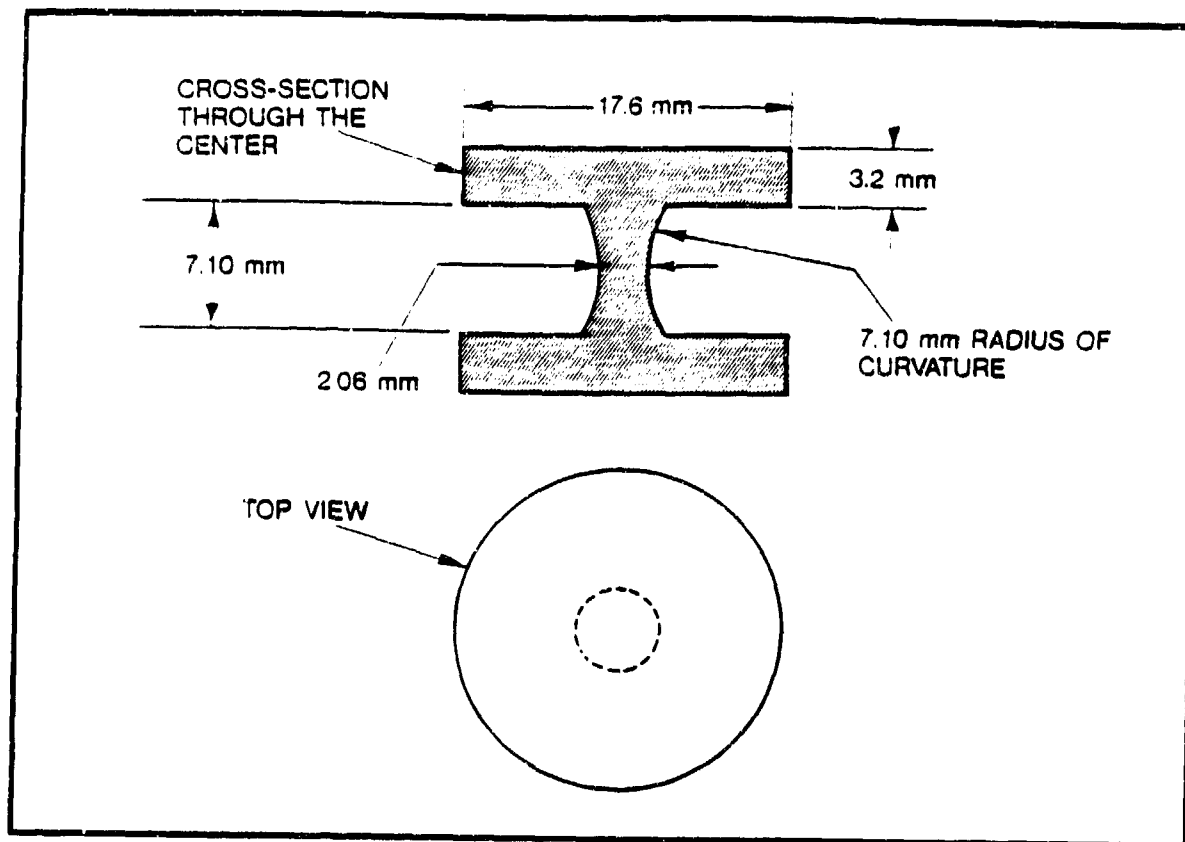
Figure 5.1(b)   Tensile specimen for through-thickness (S) orientation.

23

5.2. Fracture Toughness

To obtain fracture toughness data, both J-integral tests with compact tension C(T) specimens and short-bar tests were conducted. The tests are discussed below.

5.2.1. J-Integral

J-integral testing was carried out using compact-tension C(T) specimens with the thickness of the as-received plate. An exception was 2219-T87. For this alloy, 13 mm (1/2 in) thick specimens were machined from the center of the 25 mm (1 in) thick plate. The specimen width was 51 mm (2 in). The machined notch was modified with razor blades (shown in Figure 5.2) to permit attachment of a clip gage in the loadline. One-half of the specimens of each alloy were machined with chevrons to ensure faster precracking. The planar dimensions of the C(T) specimens used for these measurements are shown in Figure 5.2. Specimens were machined in L-T and T-L orientations; these are depicted schematically in Figure 5.3.

The J-integral specimens were precracked using a 100 kN (22.5 klb) fatigue-testing machine at room temperature for the room temperature tests and at 76 K (liquid nitrogen) for the cryogenic tests. All fatigue operations were conducted in load control using a sinusoidal load cycle at 30 Hz. After precracking, the specimens were removed from the test machine. The specimens precracked at 76 K were warmed to room temperature before testing at low temperatures.

The J-integral tests followed ASTM standard E 813-81, Standard Test Method for J_{Ic}, A Measure of Fracture Toughness[4] using the single specimen technique. The test was conducted using a computerized data acquisition system which calculated crack lengths from the elastic unloading, calculated J from the energy absorbed by the specimen, and simultaneously plotted the resistance curve (J vs. Δa). The estimated measurement inaccuracy for J_{Ic} is $\pm$ 5%.

The critical value of J (J_{Ic}, defined as the J value at the initiation of crack extension) was obtained using an algorithm following E 813-81. An estimation of the plane-strain fracture toughness, $K_{Ic}(J)$, was made using

$$K_{Ic}(J) = (EJ_{Ic})^{1/2},$$

where E is Young's modulus. Values of E used at each temperature were obtained from tensile tests.

63.5

28.58

Width, w = 50.8

12.70

Dimensions
in mm

13.08
Dia

6.35 Dia

13.97

12.70

60.69

60°

3.18

Razor
Blades

COMPACT SPECIMEN
Thickness = 24.4 mm
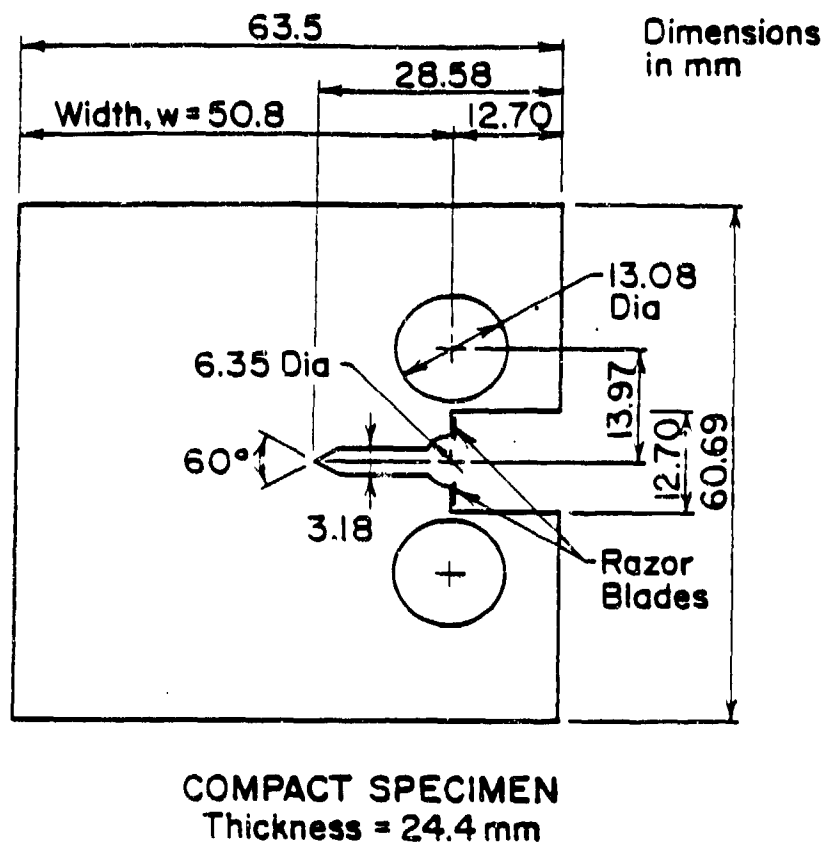
Figure 5.2 Compact-tension specimen for fracture toughness tests
in L-T and T-L orientations.
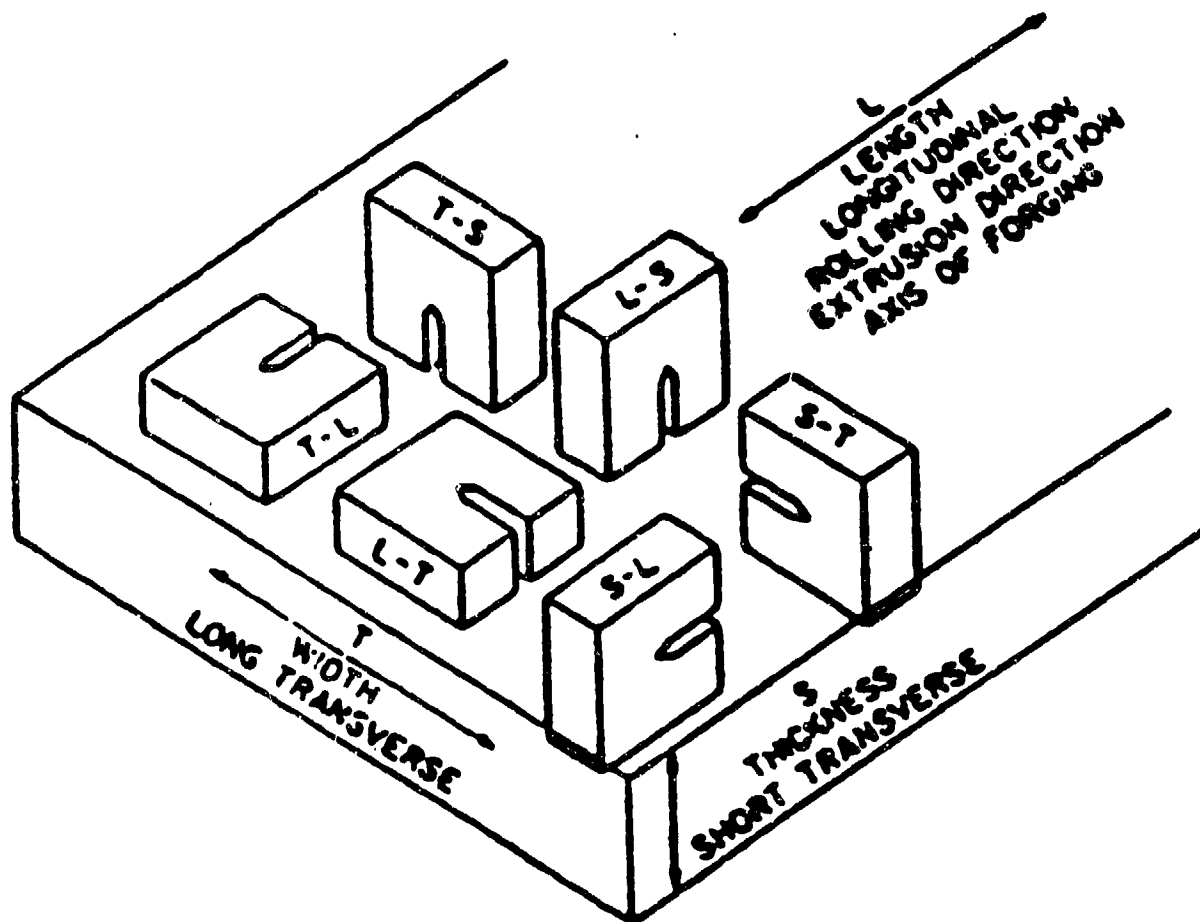
Figure 5.3 Compact-tension fracture toughness (K_{Ic}) specimen orientations.

26

5.2.2. Chevron-Notched Short-Bar

Chevron-notch short-bar fracture toughness specimens were used to determine K_{Iv} using the draft ASTM standard (E 1304)[5] for this test method. The method has a distinct advantage over K_{Ic} or J_{Ic} testing due to the relative simplicity of the test method and the ability to sample toughness through a plate thickness. For the Al-Li alloys, it is the most practical method to measure the toughness in the short-transverse (either S-T or S-L) specimen orientations. To obtain comparison with C(T) specimen data, chevron-notched short-bar specimens were also machined with T-L and L-T orientations.

The geometry of the short-bar specimens is shown in Figure 5.4. All dimensions followed those specified in the ASTM E 1304 draft standard. The specimens were 12.7 mm (0.5 in) thick and had a specimen width to thickness ratio of 1.45. The initial crack length was 5.9 mm. The specimens were tested in displacement control at 4, 76, and 295 K while monitoring the load vs. crack opening displacement. The estimated measurement inaccuracy for K_{Iv} is $\pm$ 5%.

In the various alloys tested, all three types of crack-growth behavior discussed in E 1304 were observed: smooth crack growth, crack advance by jumping (a sequence of run-arrest events), and rapid failure of the entire specimen. The analysis for the plane-strain (chevron-notch) fracture toughness was, therefore, dependent on the type of crack growth behavior observed. Details of the individual analysis procedures can be found in E 1304.

27
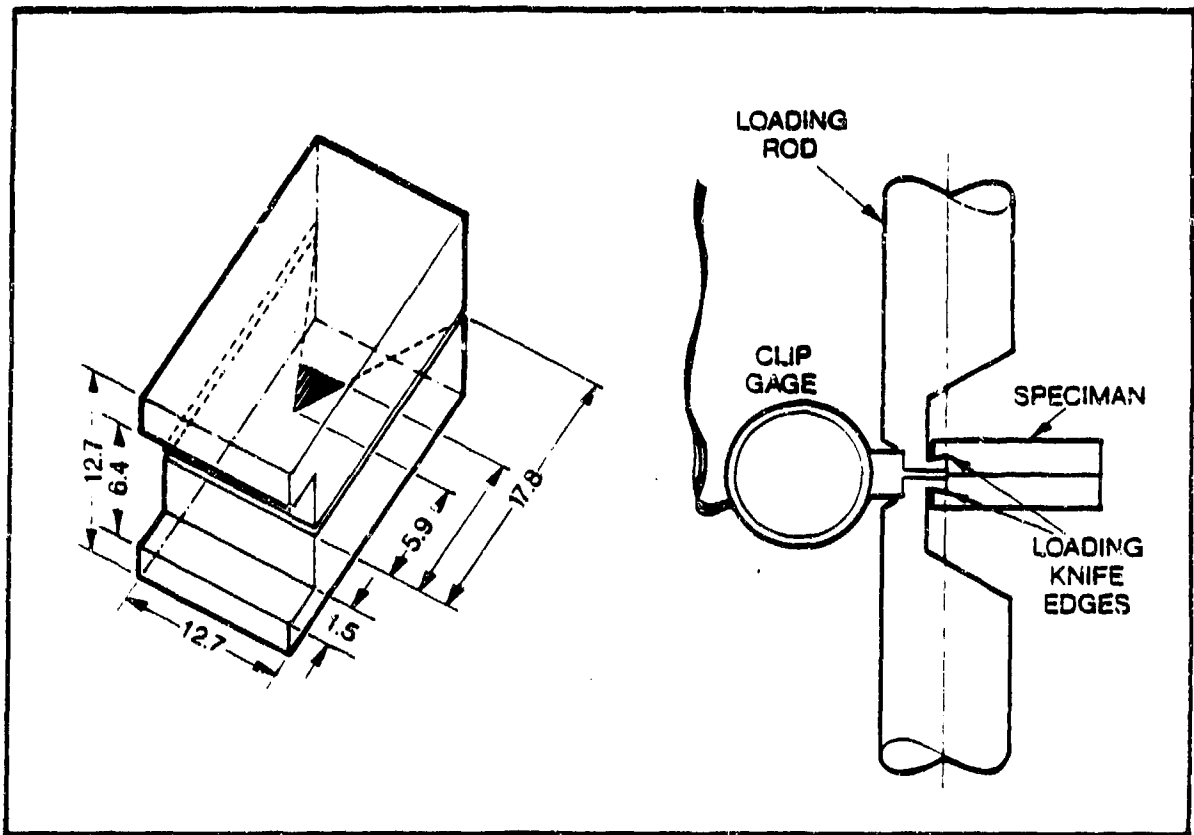
Figure 5.4   Chevron-notch, short-bar specimens for fracture
toughness tests in S-L and S-T orientations.

6. EXPERIMENTAL RESULTS AND DISCUSSION

Tensile and fracture toughness tests were conducted on alloys 8090, 2090, WL049 and 2219 in various tempers at temperatures: 295, 76, 20, and 4 K. The results are reported and briefly discussed in separate sections. Detailed metallurgical and mechanistic analyses may be presented in future technical papers.

6.1 Tensile

6.1.1 Young's Modulus

The Young's modulus (E) data are included in Table 6.1 for each alloy and temper. Since excellent stress-strain curves were obtained for most specimens, the data are considered very representative. Plots of average E values with data scatter bands (for both L and T orientations for T8 tempers) versus lithium content are shown in Figure 6.1. In this figure the alloy used to represent zero weight percent Li was 2219. Included in Figure 6.1 are the dynamic data by Ledbetter[6] (also with 2219 at zero Li content) and the MIL-HNBK-5E[7] recommended value for 2219 at room temperature. Values for T3 tempers are slightly higher for the Al-Li alloys and about equivalent for 2219.

Overall, the addition of lithium produces increases in E of about 5% per wt% Li at room temperature. The dependence on lithium content appears to increase at cryogenic temperatures (~ 3 GPa/wt. % Li at 295 K; ~ 5 GPa/wt. % Li at 76-4 K). However, alloy 8090-T8771 exhibits less temperature dependence than 2090-T81 and WL049-T351. If the data of this alloy (that contains much less Cu) are given more weight in the construction of the lines depicting the dependence of E on Li, the effects of temperature on this dependence would be negligible.

There is little orientation dependence of E in any alloy as depicted by T and L measurements. This lack of orientation dependence holds at low temperatures also. This suggests that the strong texturing effects on E of pure Al, as calculated by Wawra [8] from single-crystal data (E_{111} = 73.8 GPa, E_{100} = 63.2 GPa), are not reproduced by Al-Li stretching procedures.

Young's modulus for the T3 tempers of alloys 2219, WL049, and 8090 fall within the data scatter expected from isothermal measurements and are included in Figure 6.1. From our results it appears that aging does not alter, within experimental uncertainty, the Young's modulus. Other research on this subject for Al-Li alloys suggests an increase in E of about 2% from extended aging.[2]

At low temperatures (4-76 K), the Young's modulus is larger than at room temperatures. The increase of E at low temperatures is approximately 10 percent, of the same order as the increase in E for pure Al.[6]

Table 6.1   Tensile and Toughness Properties: 8090-T3.

Specimen Orientation	Young's Modulus, GPa (msi)	Yield Strength, MPa (ksi)	Tensile Strength, MPa (ksi)	Elongation, %	Reduction of Area, %	Fracture Toughness, MPa√m (ksi√in)	
295 K							
T	86 (12.7)	208 (30)	348 (50)	14	26		
L	82 (11.6)	217 (31)	326 (47)	12	18		
76 K							
T	88 (12.8)	241 (35)	450 (65)	20	37		
L	89 (12.9)	248 (36)	458 (66)	22	27		
						ASTM E 813	
T-L						60	(55)
L-T						97	(88)
20 K							
T	92 (13.3)	268 (39)	592 (86)	25	27		
L	92 (13.3)	272 (39)	609 (88)	28	28		
4 K							
T	89 (13.6)	270 (39)	597 (87)	24	29		
L	88 (12.8)	280 (41)	605 (88)	26	28		
						ASTM E 813	
T-L						50	(46)
L-T						74	(67)

Table 6.1 Tensile and Toughness Properties: 8090-T8151.

Specimen Orient- ation	Young's Modulus, GPa (msi)	Yield Strength, MPa (ksi)	Tensile Strength, MPa (ksi)	Elon- gation, %	Reduction of Area, %	Fracture Toughness, MPa√m (ksi√in)	
295 K							
T	80 (11.6)	405 (59)	507 (73)	6	6		
L	79 (11.4)	402 (58)	474 (69)	4	4		
S	—	—	478 (69)	—	8		
						ASTM E 813	
T-L						44	(40)
L-T						48	(44)
						ASTM E 1304	
T-L						46,48,42	(42,44,38)
L-T						47,47,48	(43,43,44)
S-L						24,21	(22,19)
S-T						29,21,26	(26,19,24)
76 K							
T	88 (12.8)	415 (60)	642 (93)	11	10		
L	88 (12.8)	411 (60)	633 (92)	10	9		
S	—	—	543 (79)	—	5		
						ASTM E 813	
T-L						48,29	(44,26)
L-T						54,58	(49,53)
						ASTM E 1304	
T-L						47,46,46	(43,42,42)
L-T						51,51	(46,46)
S-L						9,9	(8,8)
S-T						13,11	(12,10)
20 K							
T	88 (12.8)	453 (66)	756 (110)	12	10		
L	88 (12.8)	450 (65)	749 (109)	13	10		
4 K							
T	88 (12.8)	463 (67)	780 (113)	14	14		
L	87 (12.7)	452 (66)	769 (111)	15	14		
S	—	—	584 (85)	—	—		
						ASTM E 813	
T-L						42,50	(38,46)
L-T						37,61	(34,56)
						ASTM E 1304	
S-L						13,9	(12,8)
S-T						12,10	(11,9)

Table 6.1   Tensile and Toughness Properties: 8090-T8771.

Specimen Orientation	Young's Modulus, GPa (msi)	Yield Strength, MPa (ksi)	Tensile Strength, MPa (ksi)	Elongation, %	Reduction of Area, %	Fracture Toughness, MPa√m (ksi√in)
			295 K			
T	83 (12)	501 (73)	566 (82)	6	12	
L	79 (11.4)	512 (74)	567 (81)	3	6	
S	—	—	562 (81)	—	—	
						ASTM E 813
T-L						36,31,24 (33,28,22)
L-T						33,39,32 (30,35,29)
						ASTM E 1304
T-L						22,21,27 (20,19,25)
L-T						39,36,43 (35,33,39)
S-L						13 (12)
S-T						19,18 (17,16)
			76 K			
T	86 (12.5)	537 (78)	680 (99)	6	6	
L	88 (12.8)	542 (79)	699 (101)	11	11	
S	—	—	613 (89)	—	—	
						ASTM E 813
T-L						25 (23)
L-T						40,55 (36,50)
						ASTM E 1304
T-L						34,30 (31,27)
L-T						53,51 (48,46)
S-L						9,10 (8,9)
S-T						12,10 (11,9)
			20 K			
T	87 (12.7)	572 (83)	769 (111)	9	9	
L	86 (12.5)	571 (83)	799 (116)	14	13	
			4 K			
T	87 (12.7)	574 (83)	766 (111)	7	7	
L	87 (12.7)	574 (83)	806 (117)	13	15	
S	—	—	651 (94)	—	—	
						ASTM E 813
T-L						—
L-T						53,51 (48,46)
						ASTM E 1304
S-L						18,19 (16,17)
S-T						24,24 (22,22)

Table 6.1   Tensile and Toughness Properties: 2090-T81, 12.7-mm plate.

Specimen Orient-ation	Young's Modulus, GPa (msi)	Yield Strength, MPa (ksi)	Tensile Strength, MPa (ksi)	Elon-gation, %	Reduction of Area, %	Fracture Toughness, MPa√m (ksi√in)
			295 K			
T	78 (11.3)	507 (73)	546 (79)	2	4	
L	77 (11.2)	501 (73)	530 (77)	7	9	
S	—	—	566 (82)	—	3	
45°	75 (10.9)	46ć (68)	519 (75)	5	7	
						ASTM E 813
T-L						34,29 (31,26)
L-T						35,49 (32,45)
						ASTM E 1304
T-L						23,28,28 (21,25,25)
L-T						48,49,47 (44,45,43)
S-L						15,14,10 (14,13,9)
S-T						16,14,9 (15,13,8)
			76 K			
T	89 (12.9)	570 (83)	610 (88)	1	4	
L	87 (12.6)	550 (80)	616 (89)	9	9	
S	—	—	601 (87)	—	—	
45°	81 (11.7)	504 (73)	565 (82)	3	5	
						ASTM E 813
T-L						27,50 (25,46)
L-T						74,64 (67,58)
						ASTM E 1304
T-L						31,35 (28,32)
L-T						53,59 (48,54)
S-L						13,11,7 (12,10,6)
S-T						12,14 (11,13)
			20 K			
T	92 (13.3)	613 (89)	666 (97)	1	2	
L	89 (12.9)	591 (86)	715 (104)	12	10	
			4 K			
T	89 (12.9)	621 (90)	669 (97)	1	4	
L	88 (12.8)	600 (87)	688 (100)	10	17	
S	—	—	690 (100)	—	—	
45°	82 (11.9)	548 (79)	631 (91)	5	6	
						ASTM E 813
T-L						41,51 (37,46)
L-T						58,71 (53,65)
						ASTM E 1304
T-L						36,45 (33,41)
L-T						51,55 (46,50)
S-L						8,9 (7,8)
S-T						13,13 (12,12)

Table 6.1   Tensile and Toughness Properties: 2090-T81, 19.1-mm plate.

Specimen Orient-ation	Young's Modulus, GPa (msi)	Yield Strength, MPa (ksi)	Tensile Strength, MPa (ksi)	Elon-gation, %	Reduction of Area, %	Fracture Toughness, MPa/m (ksi/in)	
			295 K				
T	79 (11.4)	559 (81)	597 (86)	6	13		
L	77 (11.2)	578 (84)	608 (88)	8	17		
S	—	—	608 (88)	—	6		
						ASTM E 813	
T-L						25	(23)
L-T						37	(34)
						ASTM E 1304	
T-L						32,34,29	(29,31,26)
L-T						44,45,43	(40,41,39)
S-L						11,10,12	(10,9,11)
S-T						12,12,13	(11,11,12)
			76 K				
T	87 (12.6)	624 (90)	693 (100)	3	4		
L	86 (12.5)	649 (94)	738 (107)	10	2		
S	—	—	638 (92)	—	3		
						ASTM E 813	
T-L						24	(22)
L-T						33	(30)
						ASTM E 1304	
T-L						34,37	(31,34)
L-T						50,50	(46,46)
S-L						9,10,10	(8,9,9)
S-T						12,9	(11,8)
			20 K				
T	89 (12.9)	663 (96)	764 (111)	4	7		
L	89 (12.9)	665 (96)	836 (121)	15	12		
			4 K				
T	85 (12.3)	670 (97)	760 (110)	3	4		
L	84 (12 2)	672 (97)	861 (125)	12	7		
S	—	—	719 (104)	—	—		
						ASTM E 813	
T-L						38	(35)
L-T						44	(40)
						ASTM E 1304	
S-L						10,9	(9,8)
S-T						10,10	(9,9)

Table 6.1   Tensile and Toughness Properties. WL049-T351.

Specimen Orientation	Young's Modulus, GPa (msi)	Yield Strength, MPa (ksi)	Tensile Strength, MPa (ksi)	Elongation, %	Reduction of Area, %	Fracture Toughness, MPa√m (ksi√in)	
295 K							
T	76 (11.0)	412 (60)	541 (78)	14	22		
L	76 (11.0)	453 (66)	551 (80)	11	14		
S	—	—	519 (75)	—	23		
						ASTM E 813	
T-L						61,47	(56,43)
L-T						53,54	(48,49)
						ASTM E 1304	
T-L						52,60,58	(47,55,53)
L-T						57,57,63	(52,52,57)
S-L						42,44,44	(38,40,40)
S-T						46,43	(42,39)
76 K							
T	85 (12.4)	506 (73)	671 (97)	14	13		
L	83 (12.1)	583 (84)	680 (99)	12	14		
S	—	—	608 (88)	—	3		
						ASTM E 813	
T-L						42,43	(38,39)
L-T						43,37	(39,34)
						ASTM E 1304	
T-L						54,47	(49,43)
S-L						30,32	(27,29)
S-T						41,40	(37,35)
20 K							
T	88 (12.8)	602 (87)	798 (116)	7	13		
L	87 (12.6)	703 (102)	853 (124)	13	11		
4 K							
T	87 (12.6)	621 (90)	793 (115)	10	16		
L	82 (11.9)	699 (101)	853 (124)	13	15		
S	—	—	747 (108)	—	—		
						ASTM E 813	
T-L						26,30	(24,27)
L-T						31,30	(28,27)
						ASTM E 1304	
S-L						26,27	(24,25)
S-T						27,29	(25,26)

Table 6.1   Tensile and Toughness Properties: WL049-T651.

Specimen Orientation	Young's Modulus, GPa (msi)	Yield Strength, MPa (ksi)	Tensile Strength, MPa (ksi)	Elongation, %	Reduction of Area, %	Fracture Toughness, MPa/m (ksi/in)
			295 K			
T	77 (11.1)	543 (79)	620 (90)	10	17	
L	77 (11.1)	567 (82)	633 (92)	9	17	
S	--	—	624 (90)	—	8	
						ASTM E 813
T-L						20 (18)
L-T						25,23 (23,21)
						ASTM E 1304
T-L						30,32,33 (27,29,30)
L-T						30,28,30 (27,26,27)
S-L						22,21,31 (20,19,28)
S-T						25,25,25 (23,23,23)
			76 K			
T	83 (12)	637 (92)	744 (108)	8	11	
L	86 (12.5)	671 (97)	764 (111)	9	12	
S	—	—	691 (100)	—	3	
						ASTM E 813
T-L						21,23 (19,21)
L-T						25,21 (23,19)
						ASTM E 1304
T-L						23,26 (21,24)
L-T						39,43 (36,39)
S-L						14,14 (13,13)
S-T						16,17 (15,16)
			20 K			
T	82 (11.9)	714 (103)	843 (122)	5	9	
L	79 (11.4)	736 (107)	873 (127)	10	11	
			4 K			
T	88 (12.8)	732 (106)	851 (123)	9	9	
L	87 (12.6)	742 (108)	871 (126)	8	12	
S	—	—	703 (102)	—	—	
						ASTM E 813
T-L						20,21 (18,19)
L-T						26,27 (24,25)
						ASTM E 1304
S-L						14,15 (13,14)
S-T						16,16 (15,15)

Table 6.1   Tensile and Toughness Properties: WL049-T851 (Lot 1).

Specimen Orient-ation	Young's Modulus, GPa (msi)	Yield Strength, MPa (ksi)	Tensile Strength, MPa (ksi)	Elon-gation, %	Reduction of Area, %	Fracture Toughness, MPa/m (ksi/in)
			295 K			
T	76 (10.3)	581 (84)	638 (92)	11	22	
L	75 (10.9)	607 (88)	640 (93)	10	20	
S	—	—	627 (91)	—	3	
45°	71 (10.3)	501 (73)	561 (81)	16	37	
						ASTM E 813
T-L						23,23 (21,21)
L-T						22,21 (20,19)
						ASTM E 1304
T-L						28,28,29 (25,25,26)
L-T						31,28,34 (28,25,31)
S-L						20,21 (18,19)
S-T						23,18 (21,16)
			76 K			
T	84 (12.2)	677 (98)	761 (110)	9	12	
L	82 (12.0)	712 (103)	782 (113)	11	14	
S	—	—	745 (108)	—	—	
45°	78 (11.3)	576 (84)	665 (96)	17	28	
						ASTM E 813
T-L						20,22 (18,20)
L-T						20,23 (20,21)
						ASTM E 1304
T-L						29,30 (26,27)
L-T						45,42 (41,38)
S-L						16,23,22 (15,21,20)
S-T						16,20 (15,18)
			20 K			
T	87 (12.6)	715 (104)	853 (124)	9	9	
L	84 (12.2)	774 (112)	882 (128)	11	12	
			4 K			
T	84 (12.2)	744 (108)	859 (124)	8	10	
L	83 (12.0)	785 (114)	893 (129)	11	13	
S	—	—	812 (118)	—	—	
45°	99 (14.3)	618 (90)	757 (110)	12	22	
						ASTM E 813
T-L						26,23 (24,21)
L-T						31,27 (28,25)
						ASTM E 1304
T-L						35,29 (32,26)
L-T						50,50 (46,46)
S-L						22 (20)
S-T						31,31 (28,28)

Table 6.1   Tensile and Toughness Properties: WLD 049-T851 (lot 2)

Specimen Orientation	Young's Modulus, GPa (msi)	Yield Strength, MPa (ksi)	Tensile Strength, MPa (ksi)	Elongation, %	Reduction of Area, %	Fracture Toughness, $MPa\sqrt{m}$ (ksi$\sqrt{in}$)
295 K						
T	75 (10.9)	590 (86)	633 (92)	27	10	
L	75 (10.9)	615 (89)	644 (93)	23	10	
						ASTM E 813
T-L						22 (20)
L-T						25 (23)
76 K						
T	85 (12.4)	680 (99)	760 (110)	15	9	
L	82 (12)	717 (104)	782 (113)	17	9	
						ASTM E 813
T-L						22 (20)
L-T						21 (19)
4 K						
T	83 (12)	775 (112)	853 (124)	14	9	
L	85 (12.3)	780 (113)	884 (128)	12	10	
						ASTM E 813
T-L						21,24 (20)
L-T						23,26 (22)

Table 6.1 Tensile and Toughness Properties: 2219-T37.

Specimen Orientation	Young's Modulus, GPa (msi)	Yield Strength, MPa (ksi)	Tensile Strength, MPa (ksi)	Elongation, %	Reduction of Area, %	Fracture Toughness, MPa√m (ksi√in)
295 K						
T	70 (10.1)	303 (44)	398 (58)	11	25	
L	71 (10.3)	333 (48)	391 (57)	12	28	
S	—	—	427 (62)	—	—	
						__ASTM E 813__
T-L						26,26 (24,24)
L-T						31,26 (28,24)
						__ASTM E 1304__
T-L						35,36,34 (32,33,31)
L-T						39,38,40 (35,35,36)
S-L						26,27,25 (24,25,23)
S-T						27,26,32 (25,24,29)
76 K						
T	77 (11.2)	381 (55)	518 (75)	16	21	
L	77 (11.2)	420 (61)	510 (74)	17	27	
S	—	—	525 (76)	—	—	
						__ASTM E 813__
T-L						32,33 (29,30)
L-T						41,39 (37,35)
						__ASTM E 1304__
T-L						45,45 (41,41)
L-T						57,51 (52,46)
S-L						31,30,29, (28,27,26, 27 25)
S-T						33,35 (30,32)
20 K						
T	79 (11.4)	463 (67)	668 (97)	13	18	
L	82 (11.9)	500 (72)	665 (96)	18	19	
4 K						
T	80 (11.6)	447 (69)	668 (97)	14	16	
L	72 (10.4)	516 (75)	671 (97)	17	23	
S	—	—	664 (96)	—	—	
						__ASTM E 813__
T-L						33,33 (30,30)
L-T						35,42 (32,38)
						__ASTM E 1304__
T-L						51,57 (46,52)
L-T						47,41 (43,37)
S-L						33 (30)

Table 6.1   Tensile and Toughness Properties: 2219-T87.

Specimen Orientation	Young's Modulus, GPa (msi)	Yield Strength, MPa (ksi)	Tensile Strength, MPa (ksi)	Elongation, %	Reduction of Area, %	Fracture Toughness, MPa√m (ksi√in)	
295 K							
T	73 (10.4)	381 (55)	472 (68)	13	28		
L	72 (10.1)	386 (56)	472 (68)	13	32		
45°	70 (10.1)	378 (55)	468 (67)	13	31		
						ASTM E 813	
						29,26	(26,24)
						30,28	(27,25)
76 K							
T	77 (11.3)	456 (66)	582 (84)	13	24		
L	76 (11.0)	463 (67)	583 (84)	14	31		
45°	77 (11.2)	449 (65)	579 (83)	13	28		
						ASTM E 813	
T-L						30,43	(27,39)
L-T						42.37	(38,34)
4 K							
T	76 (10.6)	499 (72)	701 (102)	14	22		
L	76 (10.9)	505 (73)	704 (102)	14	29		
45°	75 (10.9)	491 (71)	703 (102)	15	27		
						ASTM E 813	
T-L						36,37	(33,34)
L-T						46,43	(42,39)
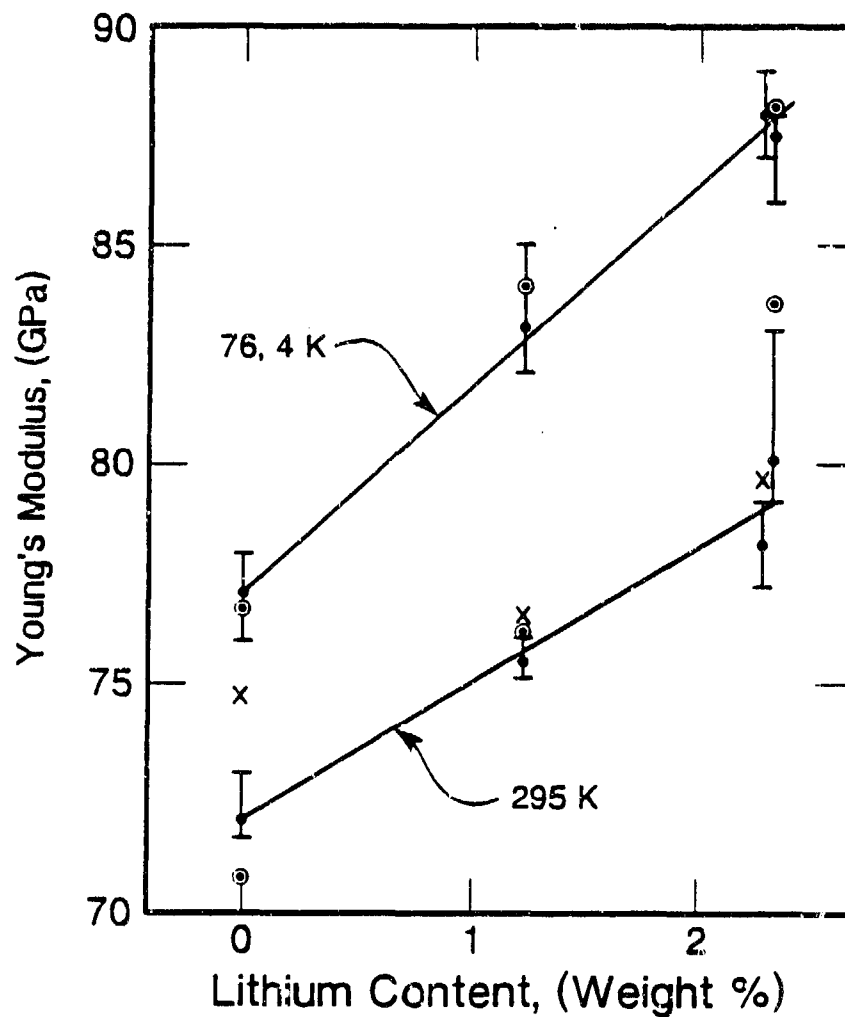
Figure 6.1   Dependence of Young's Modulus on lithium content.
T, L orientations and T8 tempers (•); T, L
orientations and T3 tempers (⊙); Ledbetter, 1990,
dynamic data (x)[6]; MIL-HDBK recommended value for
2219 (□)[2].

41

6.1.2 Strength

The tensile yield strength, ultimate strength, and elongation-to-failure data are included in Table 6.1 for all alloys and tempers. The properties are plotted as a function of temperature in Figures 6.2 to 6.23. Discussion is deferred to Section 6.1.3.

At lower temperatures, the tensile yield strength (σ_y) and ultimate strength (σ_u) increase for all alloys and tempers. The yield strength increases were between 10-20% for the T8 tempers and 25-50% for the T3 tempers, comparing 4-K to 295-K data. Ultimate strength increases were between 20-40% for the T8 tempers and 50-85% for the T3 tempers. Thus, larger (by a factor of 2) increases in strength were found for T3 tempers, compared to T8 tempers.

The distinction between the temperature dependences of σ_y and σ_u in the two tempers is understandable if one assumes the presence of much smaller precipitates in the T3 condition. Smaller precipitates are ineffective at room temperature in restricting dislocation motion. At low temperatures, the reduced thermal energy prevents dislocation flow past the smaller particles; this results in attendant increases in flow strength and in a strong temperature dependence of the flow strength. On the other hand, the longer range stress fields of the larger precipitates present in the alloys of the T8 condition are relatively effective in resisting dislocation motion at room temperature. Thus, at temperatures below 295 K the temperature dependence of the strengths of the T8 alloys is less.

The values of σ_y and σ_u in the transverse (T) specimen orientation are generally less than the values in the longitudinal (L) rolling direction. There are two exceptions to this: alloys 8090-T8151 and 2090-T81, 12.7 mm (0.5 in) plate. Distinctions of σ_u between T and L orientations tended to become greater at low temperatures. This trend is probably associated with delamination. These will be discussed later in the fractography section.

The measurements of the tensile properties in through-thickness orientation (S) were difficult. Early design of the specimens to include a uniform gage length led to failures along the radius of curvature from the reduced section to the grip area. Reductions in the reduced section resulted in the final specimen configuration shown in Figure 4.1(b). With this hour-glass geometry, failures were confined to the reduced section and the ultimate strength could be accurately determined. However, consistent and reliable yield strength and elongation data were not obtained in these tests.

The σ_u data obtained from the through-thickness tensile tests are contained in Table 6.1 and are also plotted in Figure 6.24. At room temperature, the through-thickness σ_u values, labeled $\sigma_u(S)$ are equivalent to, or up to 5% higher, than the $\sigma_u(T)$ or $\sigma_u(L)$ values. At cryogenic temperatures the $\sigma_u(S)$ values do not increase as rapidly as the L or T orientation values; consequently, the ratios of $\sigma_u(S)/[\sigma_u(L) + \sigma_u(T)]^{1/2}$ decrease at 4 K to values between 0.75 to 1.02. At 4 K, the highest ratio of 1.02 represents alloy 2090-T81 (12.7-mm plate); all other alloys have ratios less than 0.94.
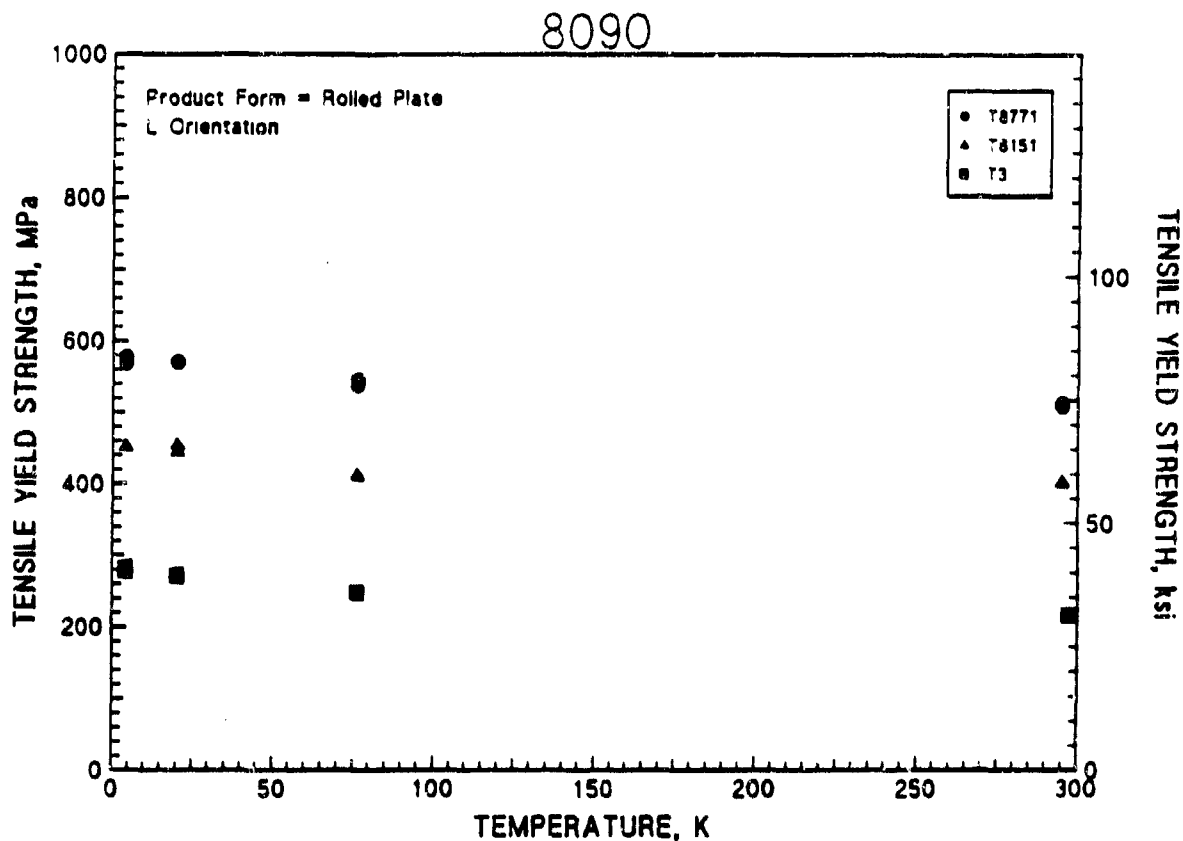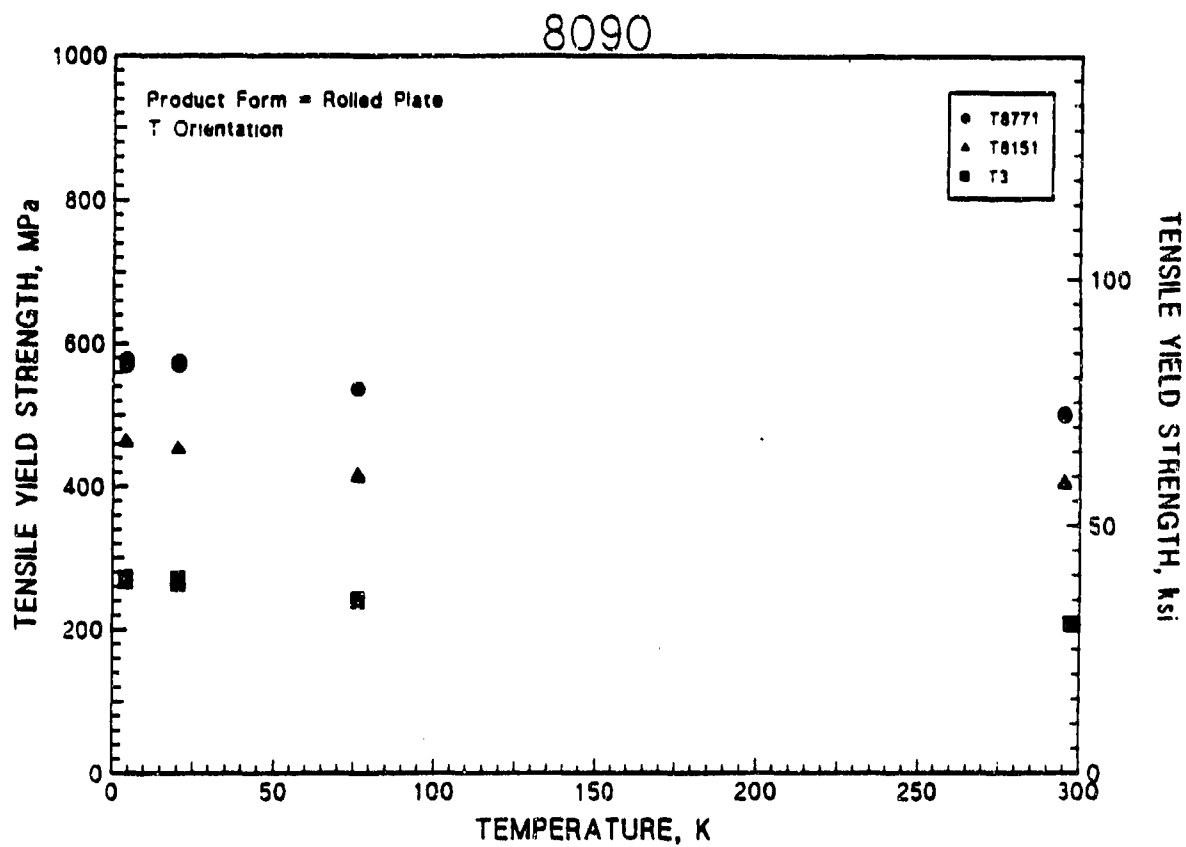
Figure 6.2   Tensile yield strength versus temperature for 8090,
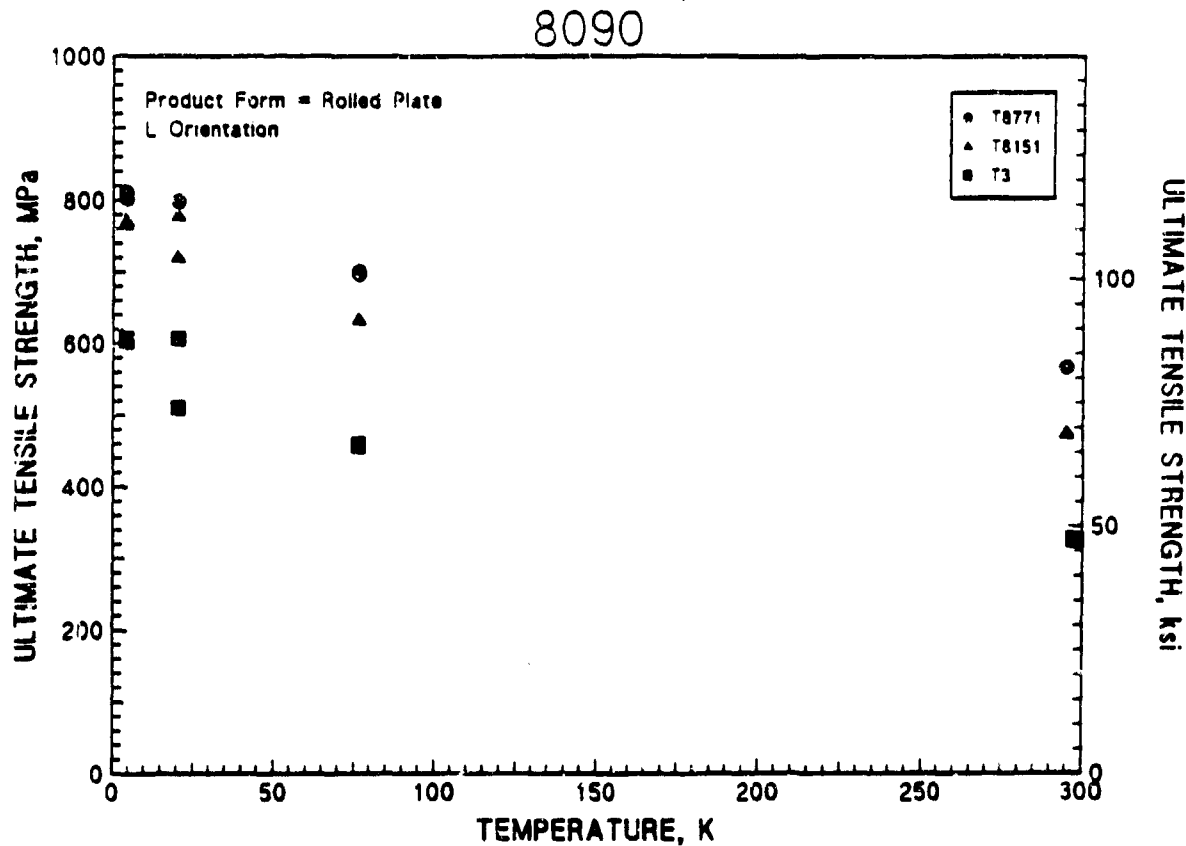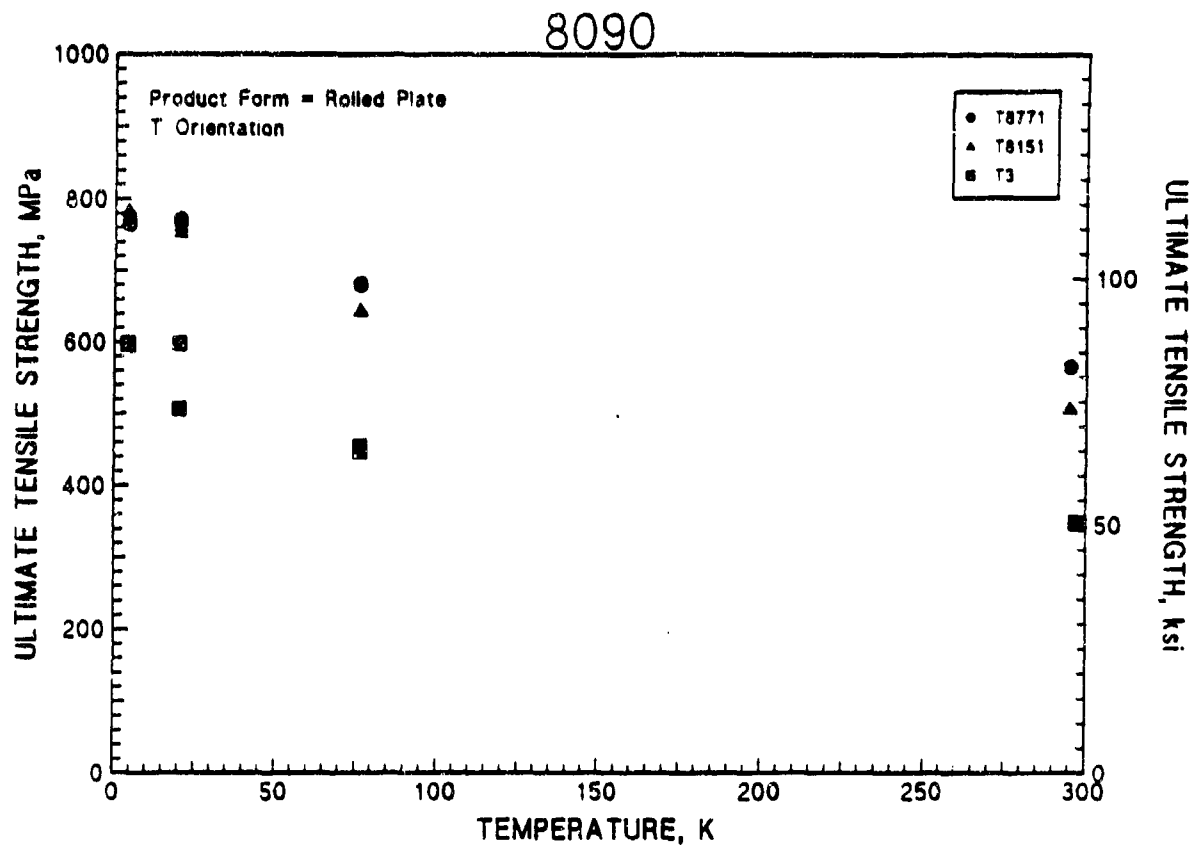T (upper graph) and L (lower graph) orientations.

43

Figure 6.3   Ultimate tensile strength versus temperature for 8090,
             T (upper graph) and L (lower graph) orientations.
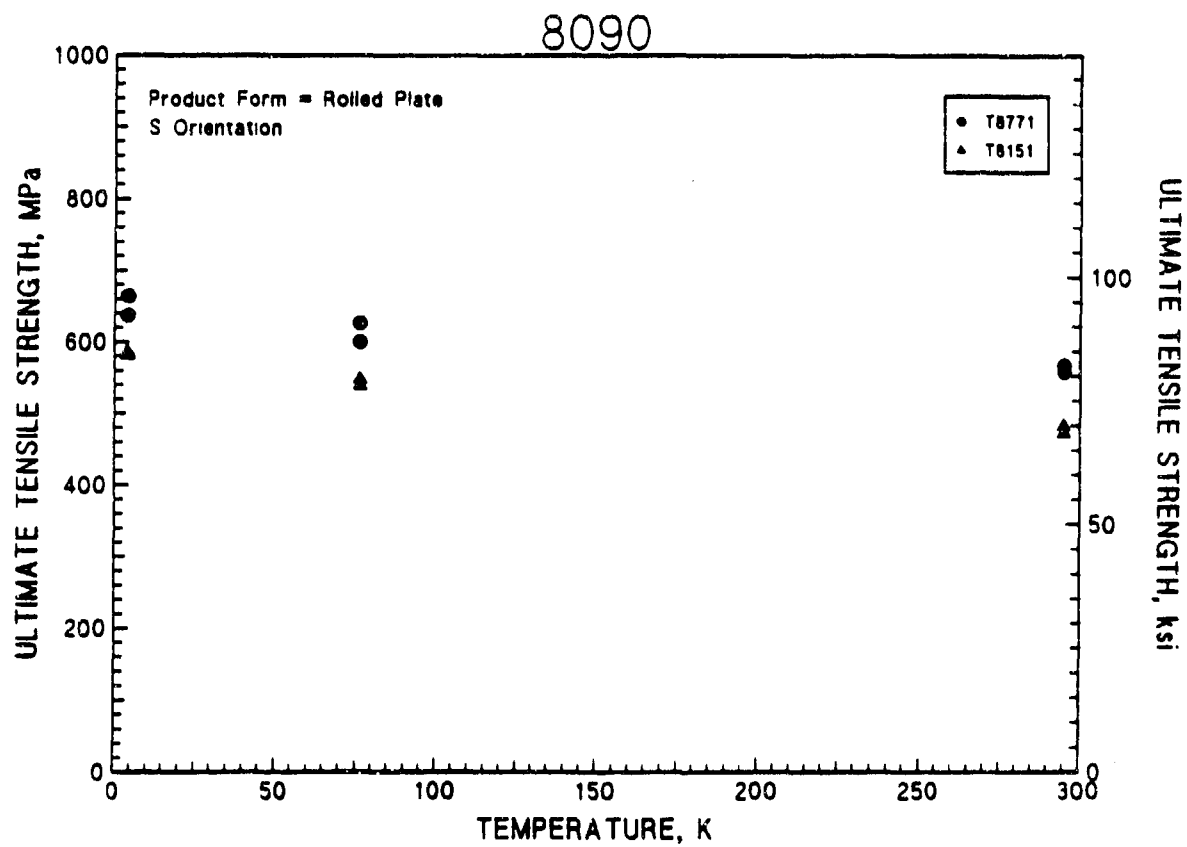
Figure 6.4   Ultimate tensile strength versus temperature for
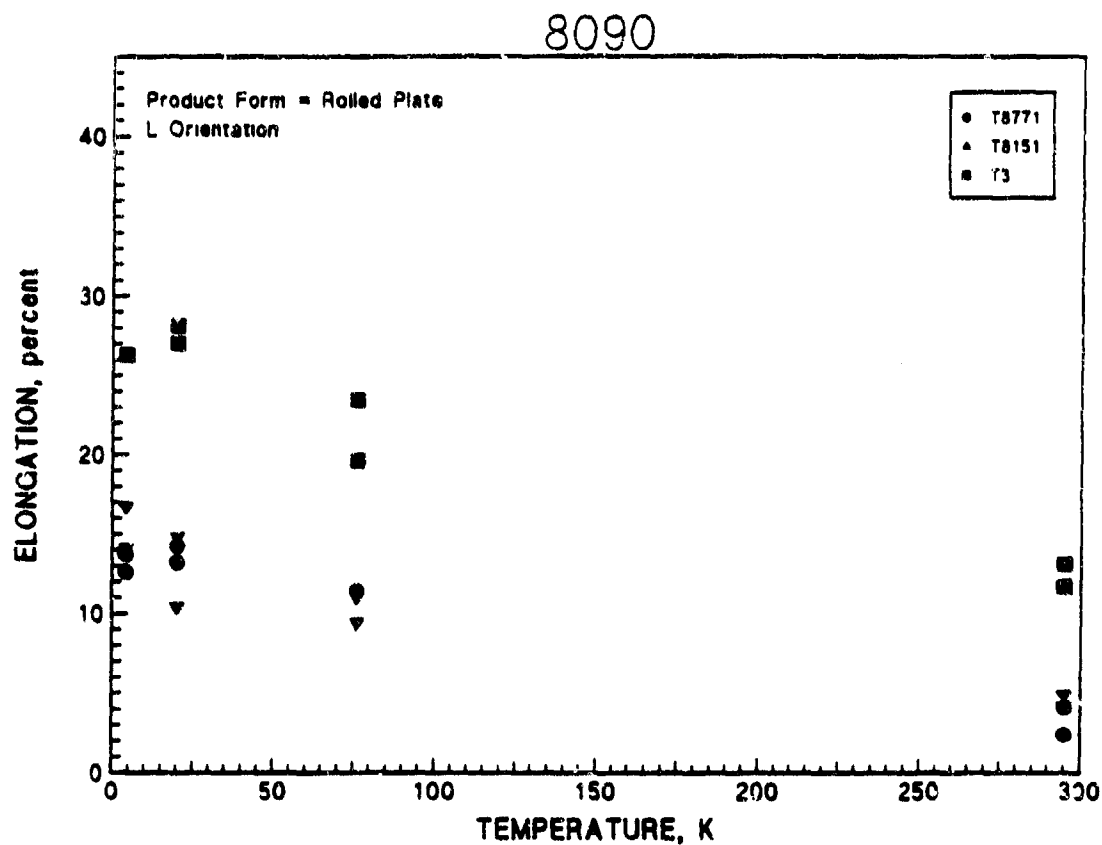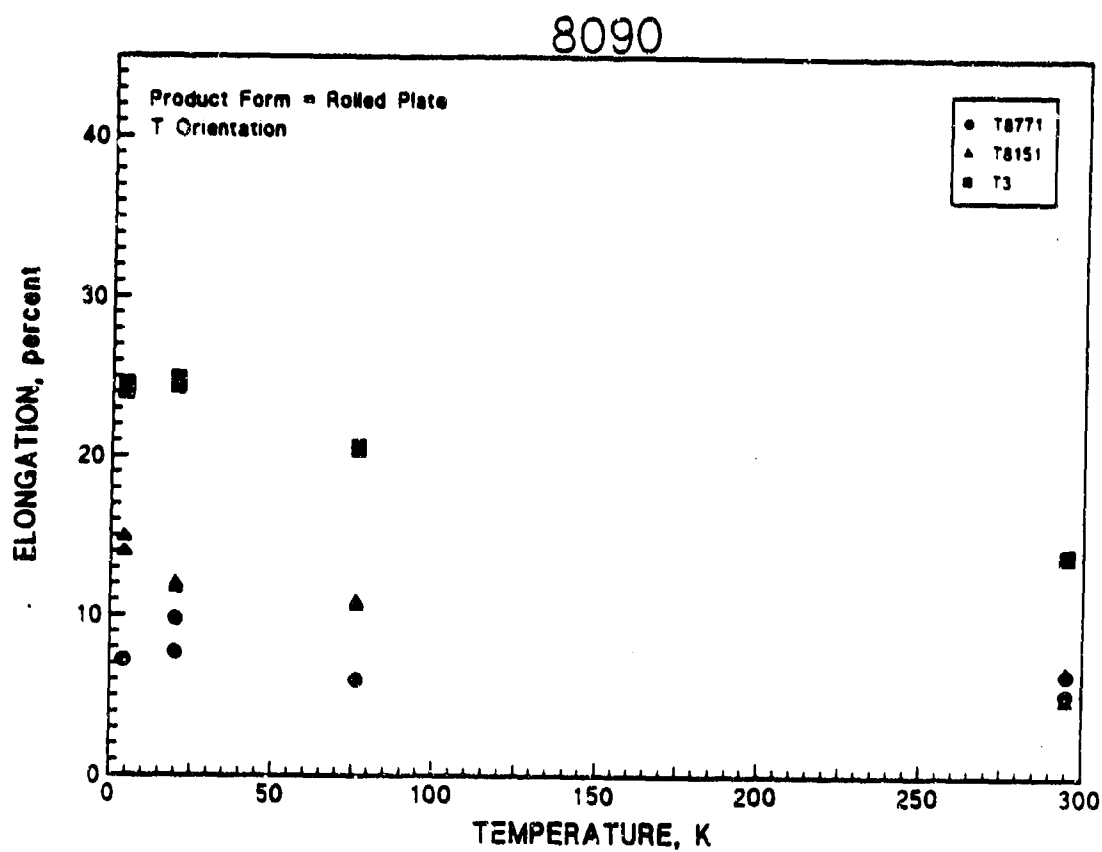8090, S orientation.

45

Figure 6.5   Tensile elongation versus temperature for 8090,
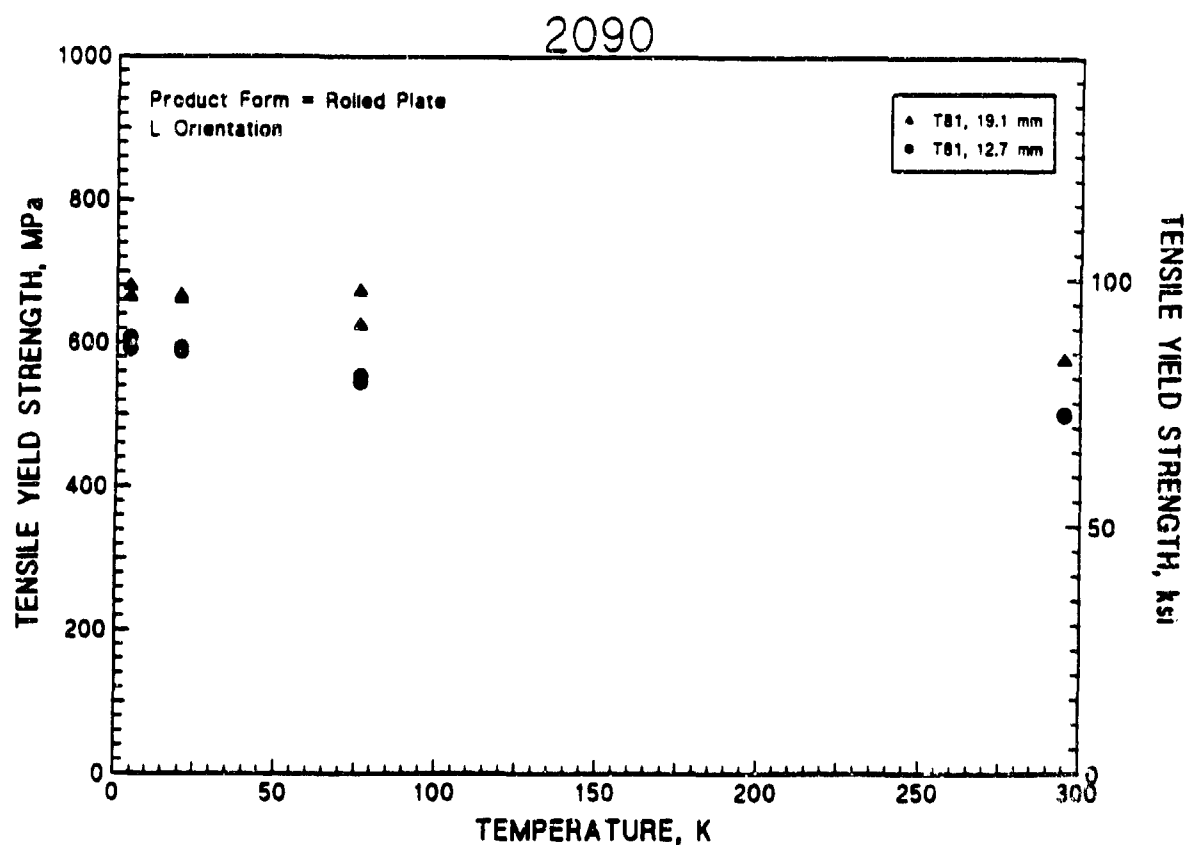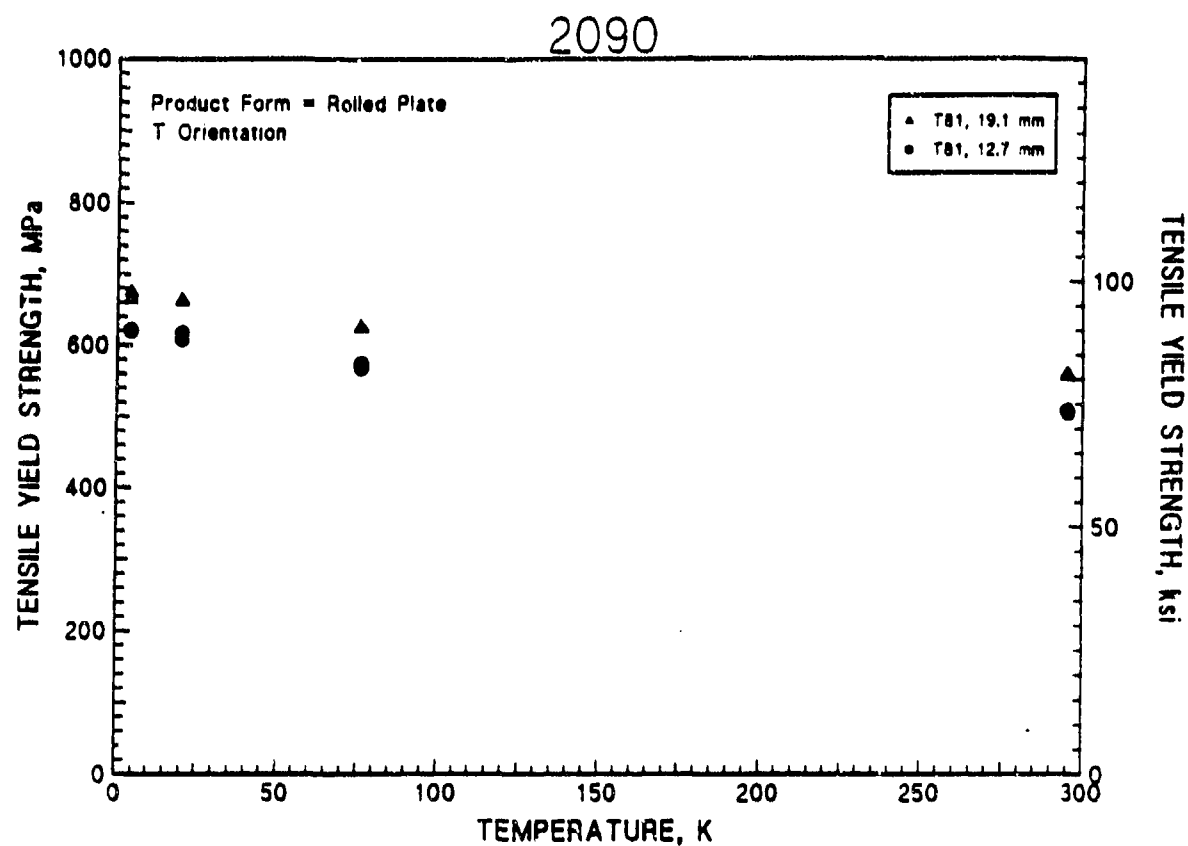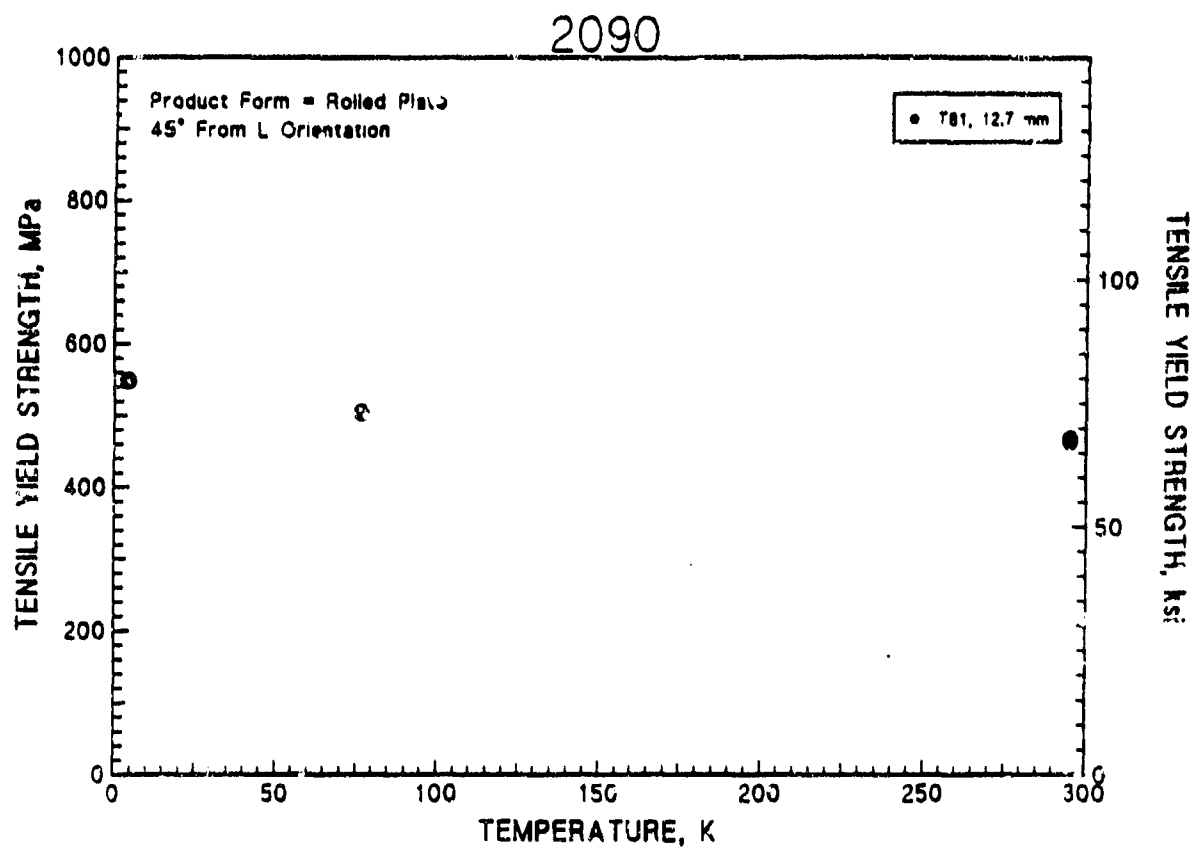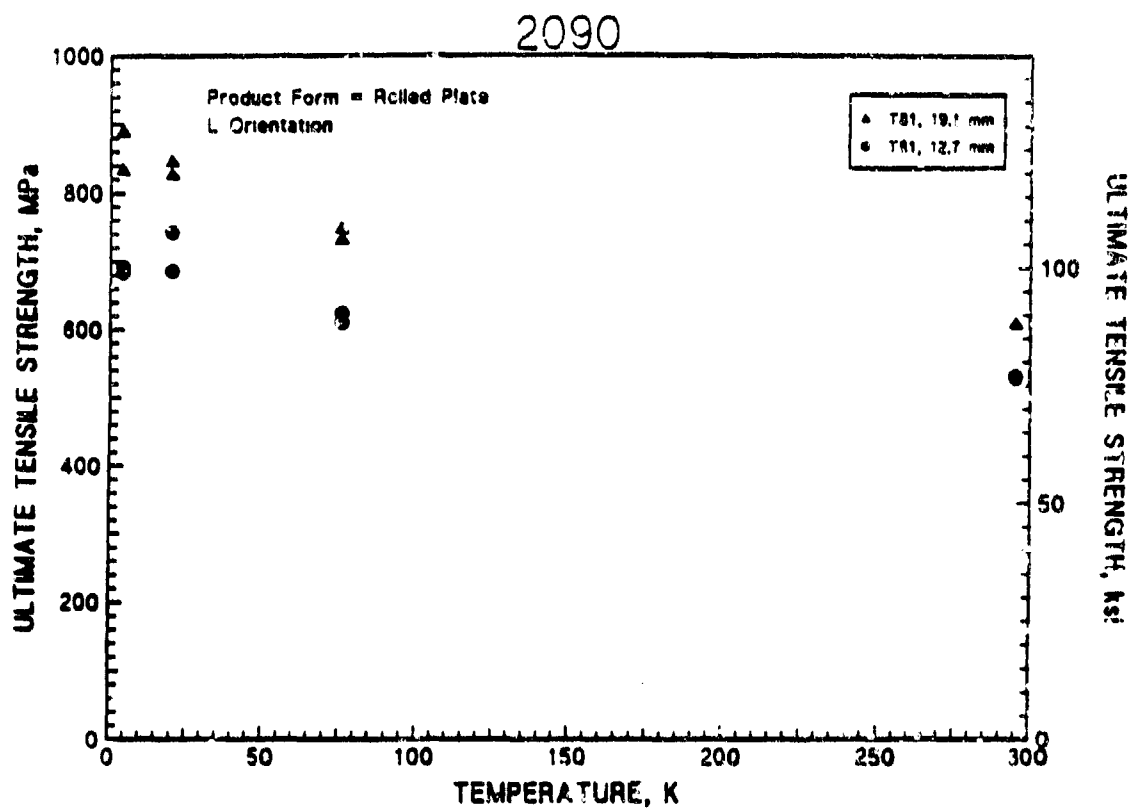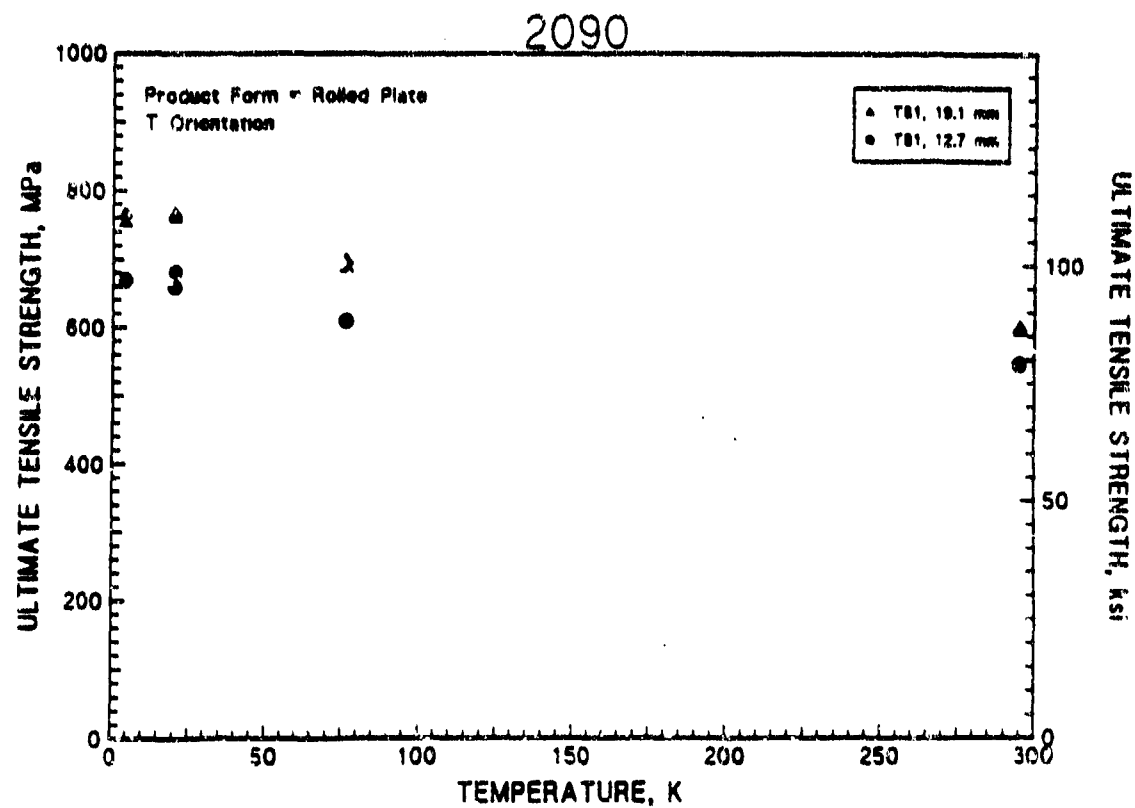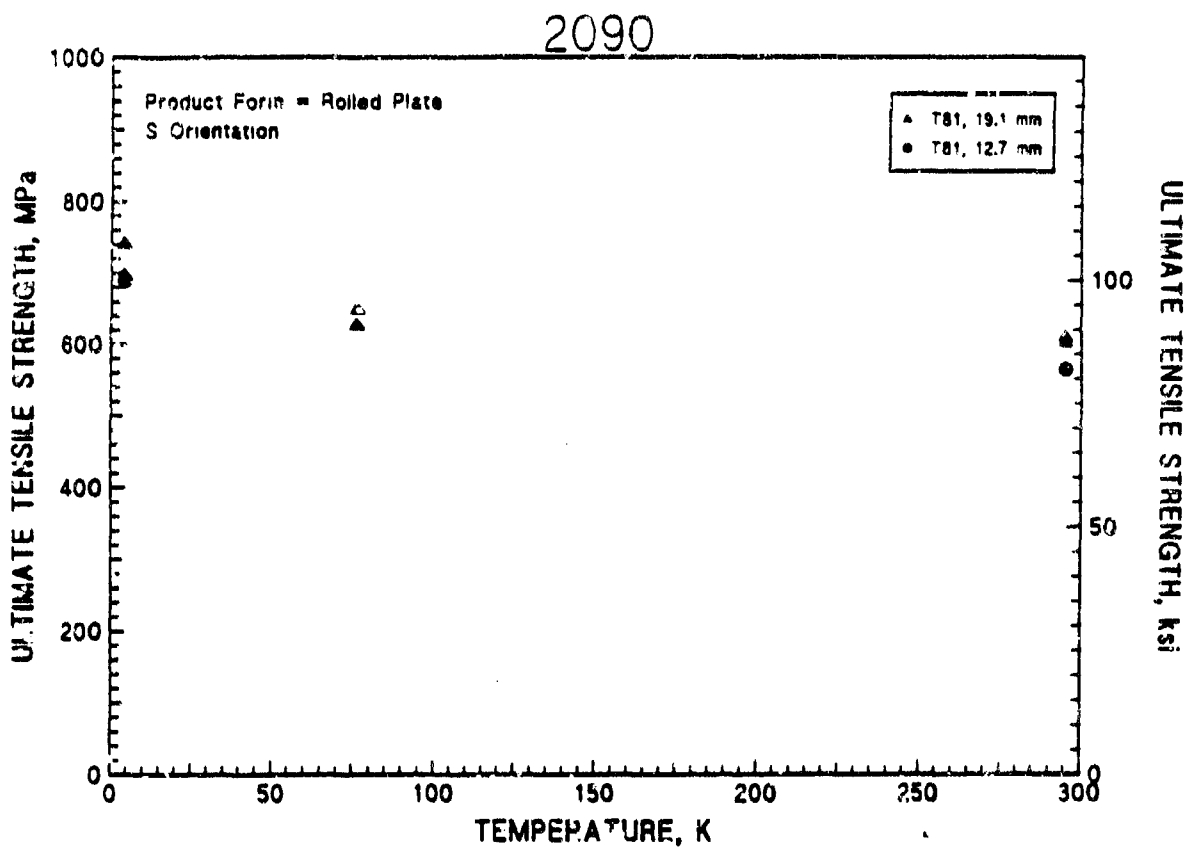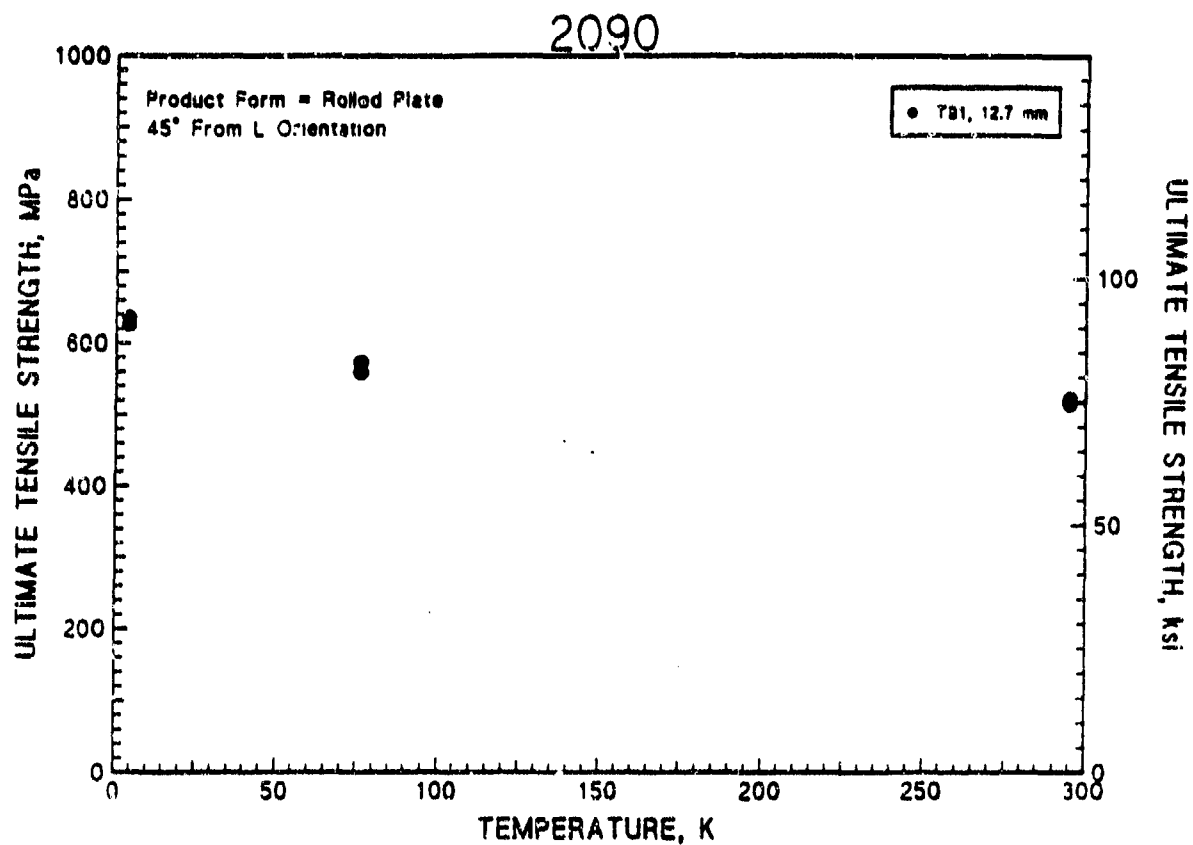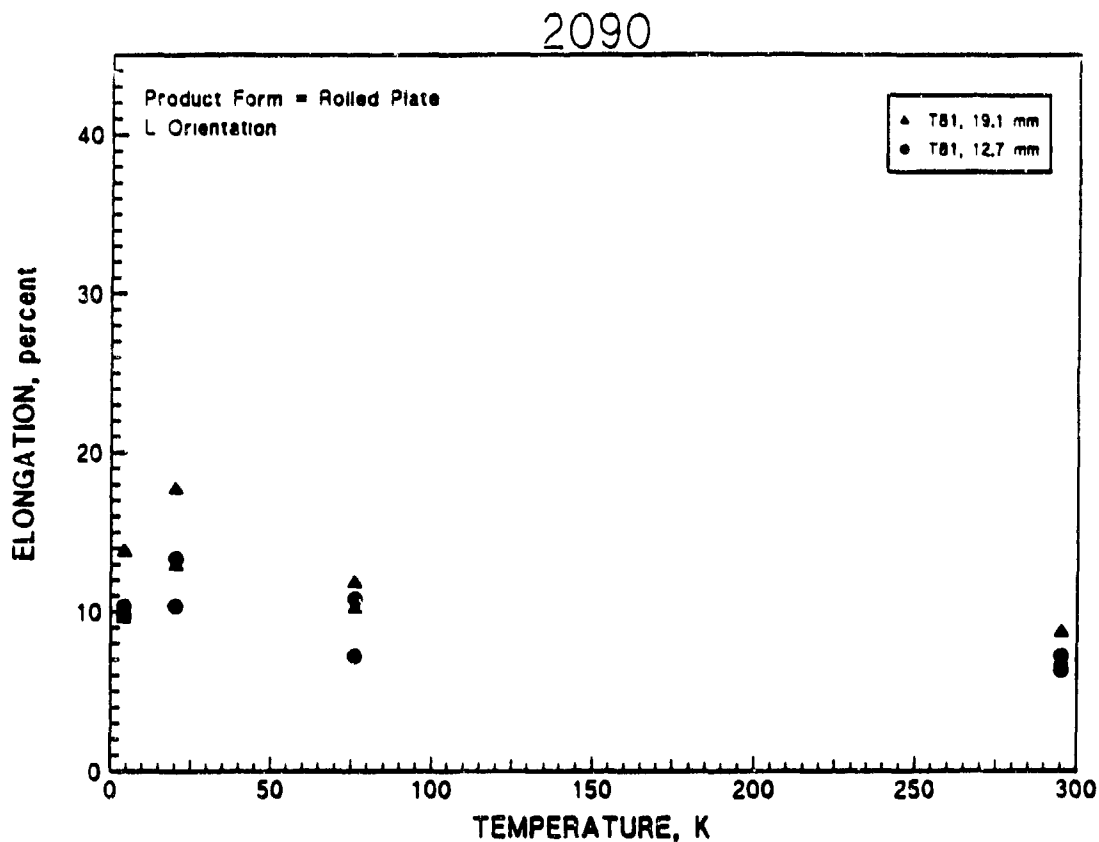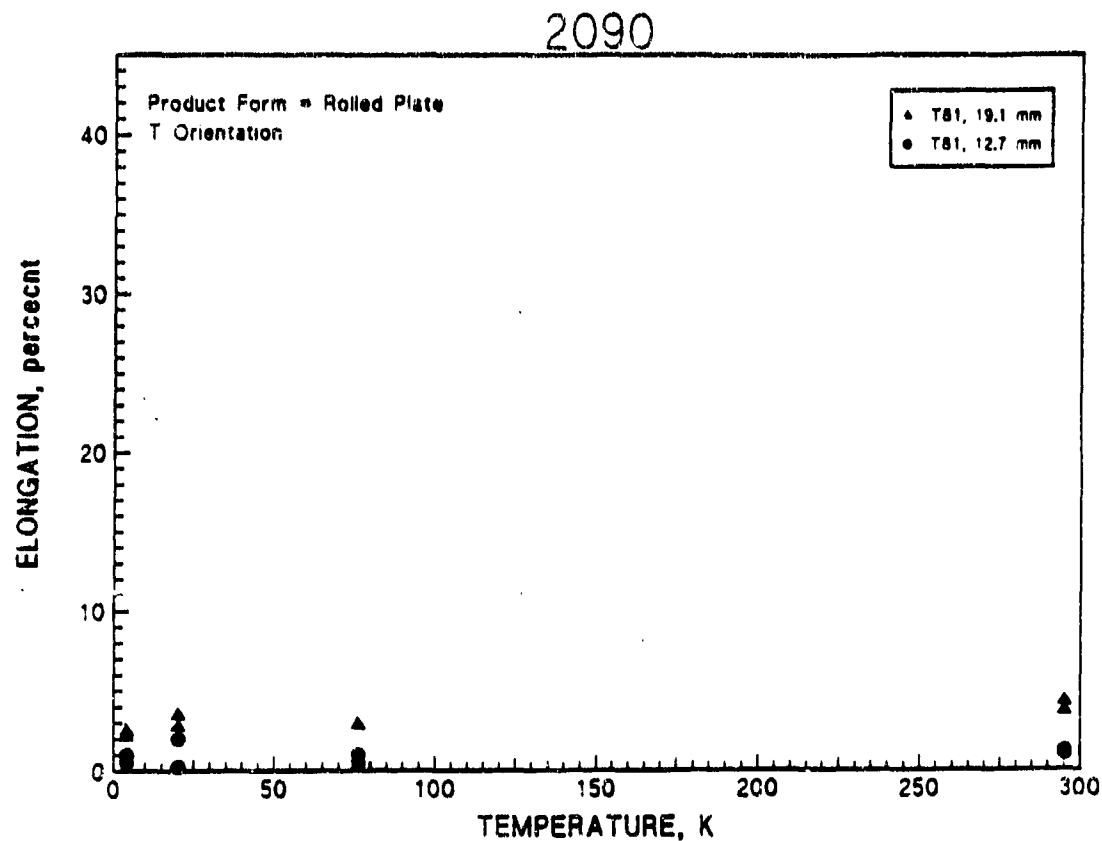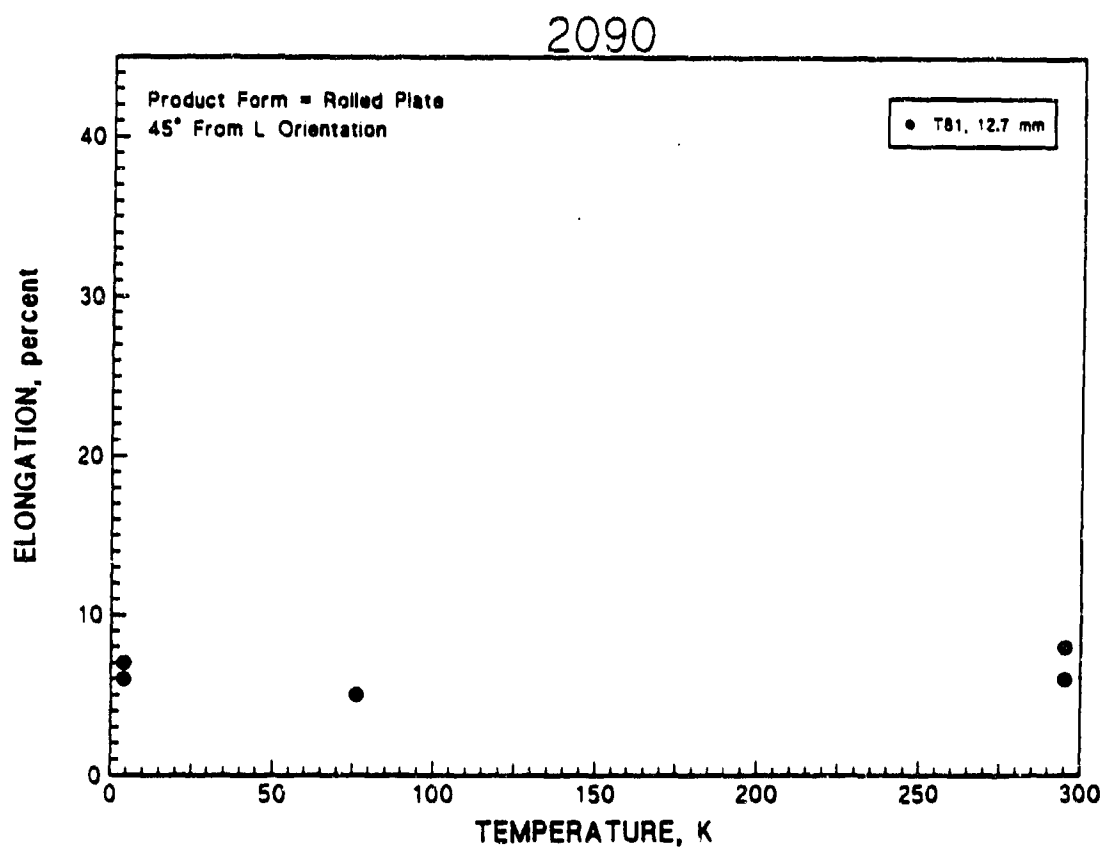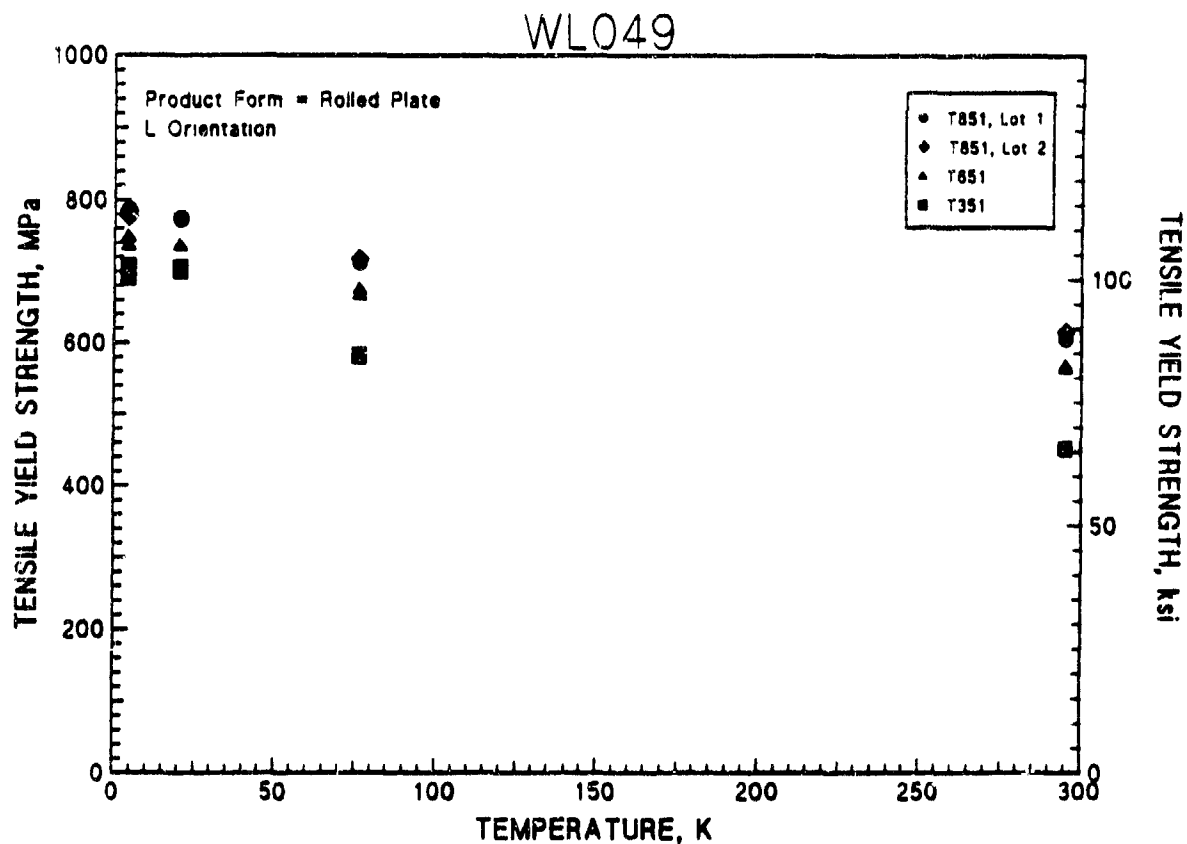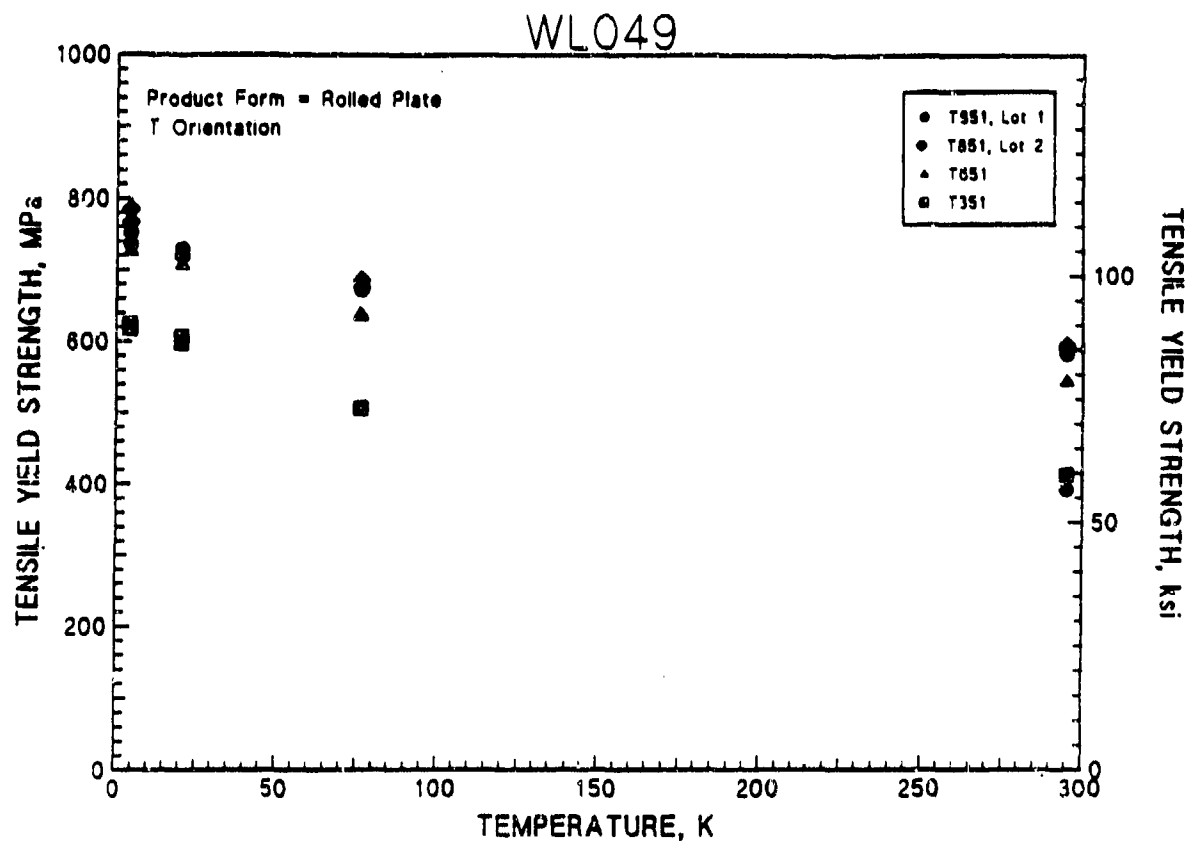   T (upper graph) and L (lower graph) orientations.

Figure 6.6   Tensile yield strength versus temperature for 2090,
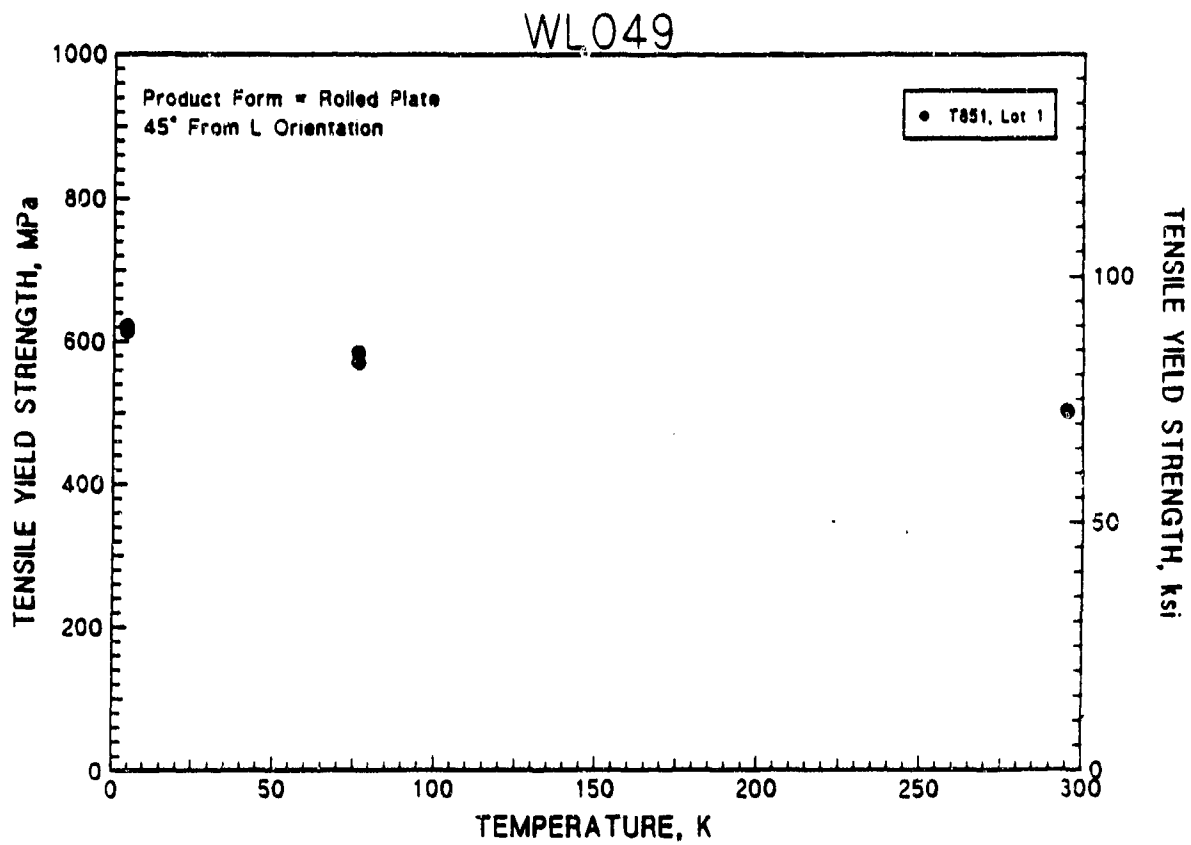T (upper graph) and L (lower graph) orientations.

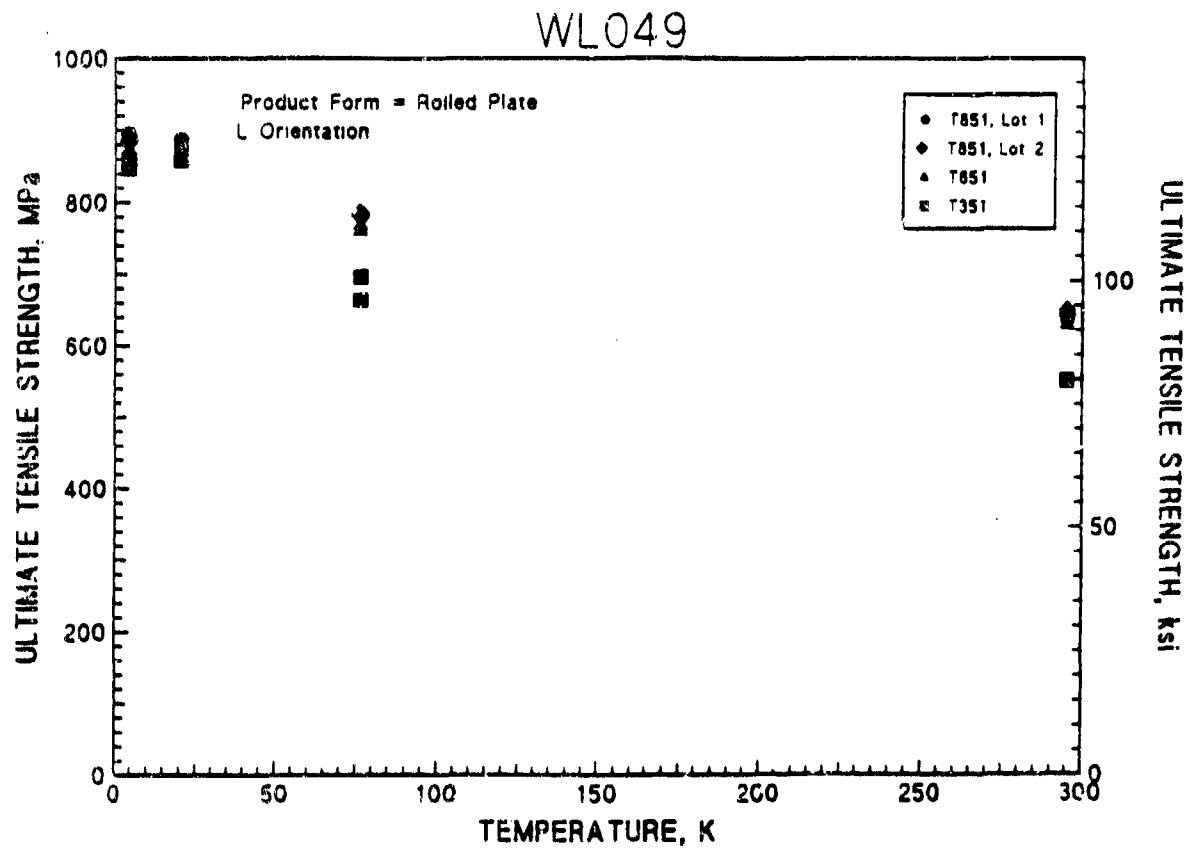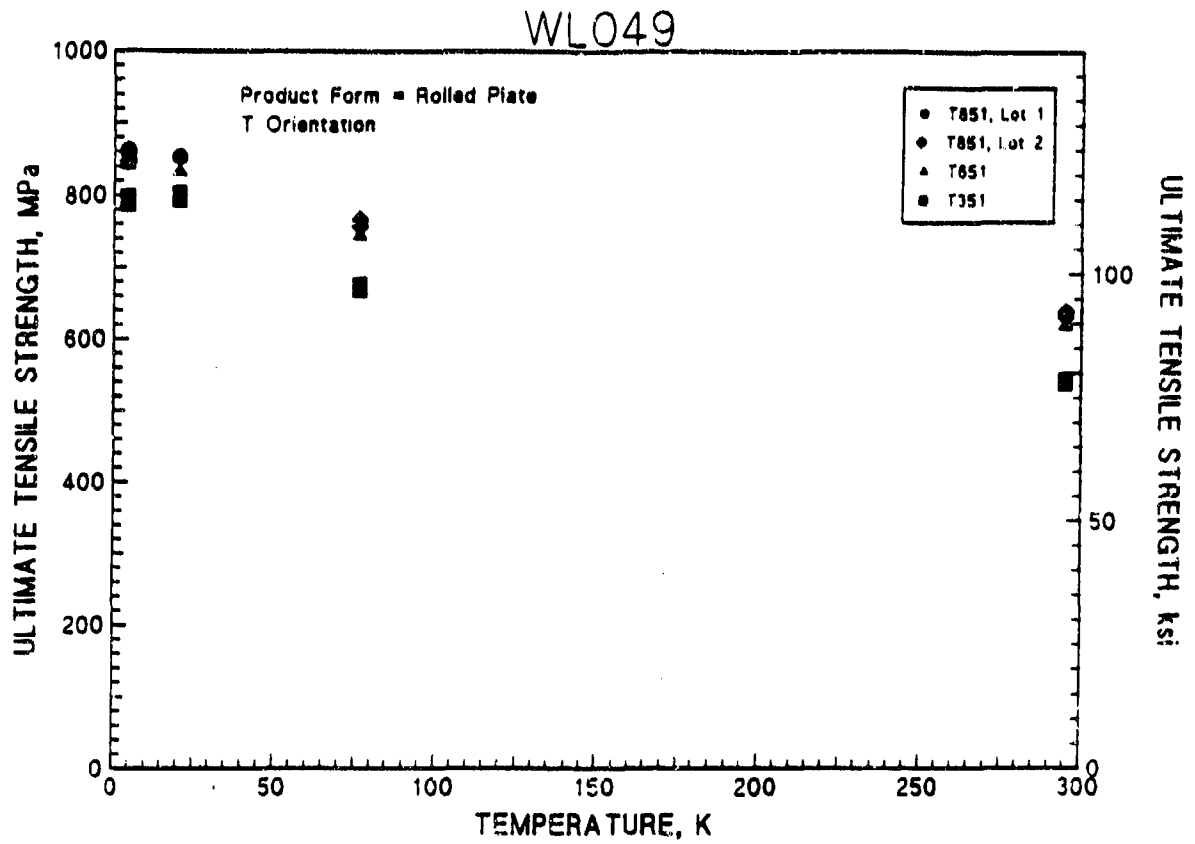Figure 6.7   Tensile yield strength versus temperature for 8090, 45° orientation.

Figure 6.8   Ultimate tensile strength versus temperature for 2090,
T (upper graph) and L (lower graph) orientations.

Figure 6.9   Ultimate tensile strength versus temperature for 2090,
45° (upper graph) and S (lower graph) orientations.

Figure 6.10   Tensile elongation versus temperature for 2090,
              T (upper graph) and L (lower graph) orientations.

51

Figure 6.11   Tensile elongation versus temperature for 2090,
             45° orientation.

Figure 6.12   Tensile yield strength versus temperature for WL049,
T (upper graph) and L (lower graph) orientations.

WL049

Figure 6.13   Tensile yield strength versus temperature for WL049,
45° orientation.

Figure 6.14 Ultimate tensile strength versus temperature for WL049,
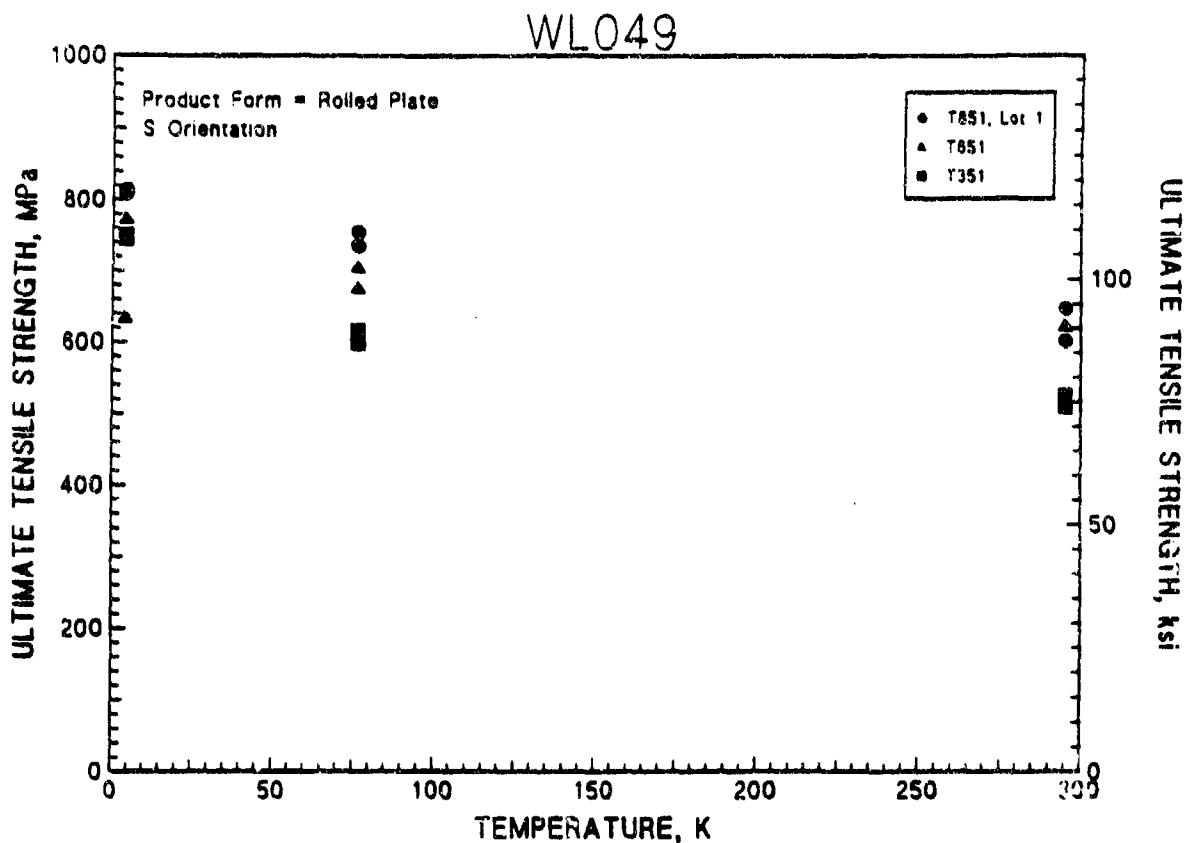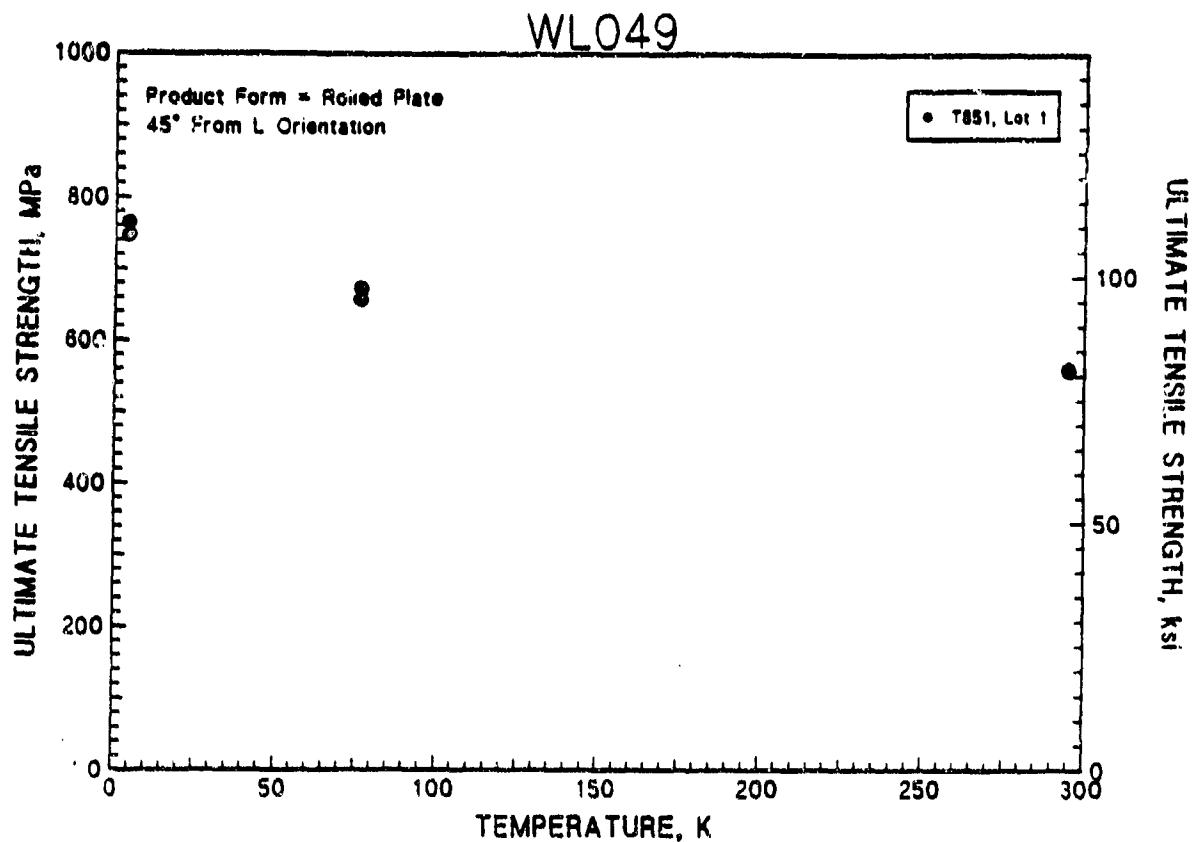T (upper graph) and L (lower graph) orientations.

Figure 6.15 Ultimate tensile strength versus temperature for WL049,
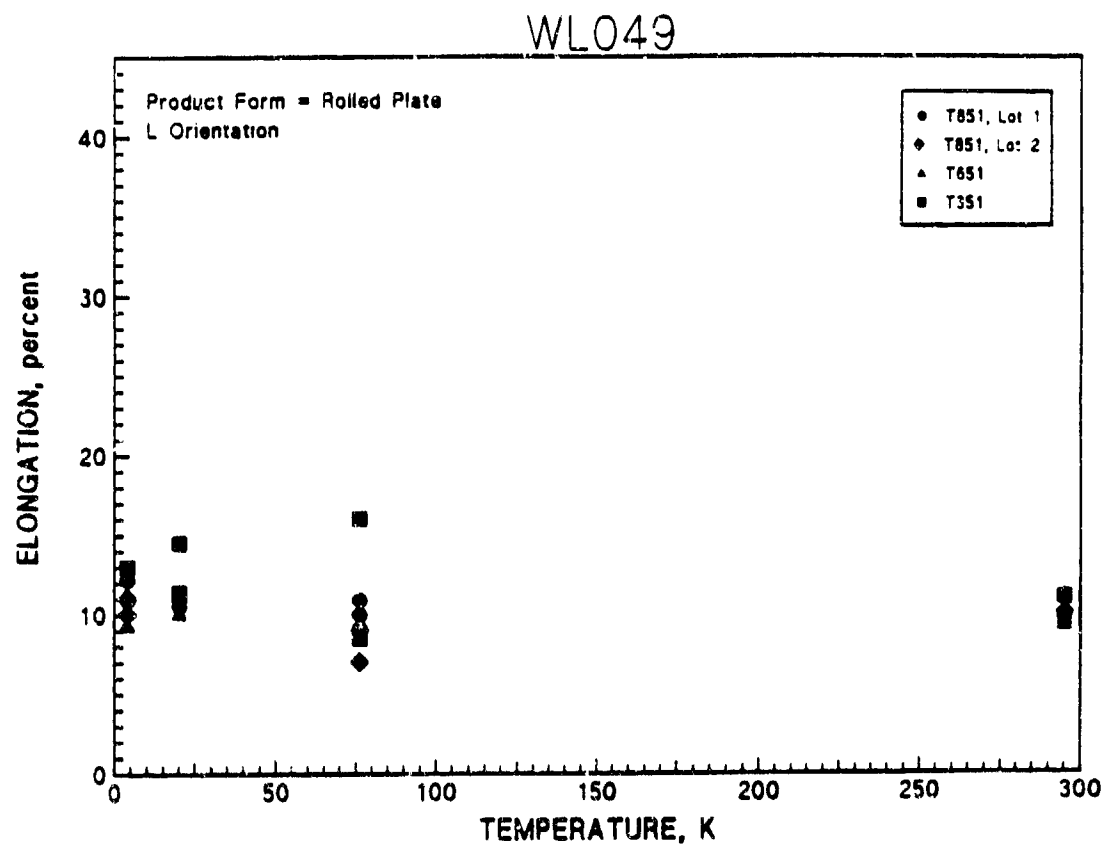45° (upper graph) and S (lower graph) orientations.
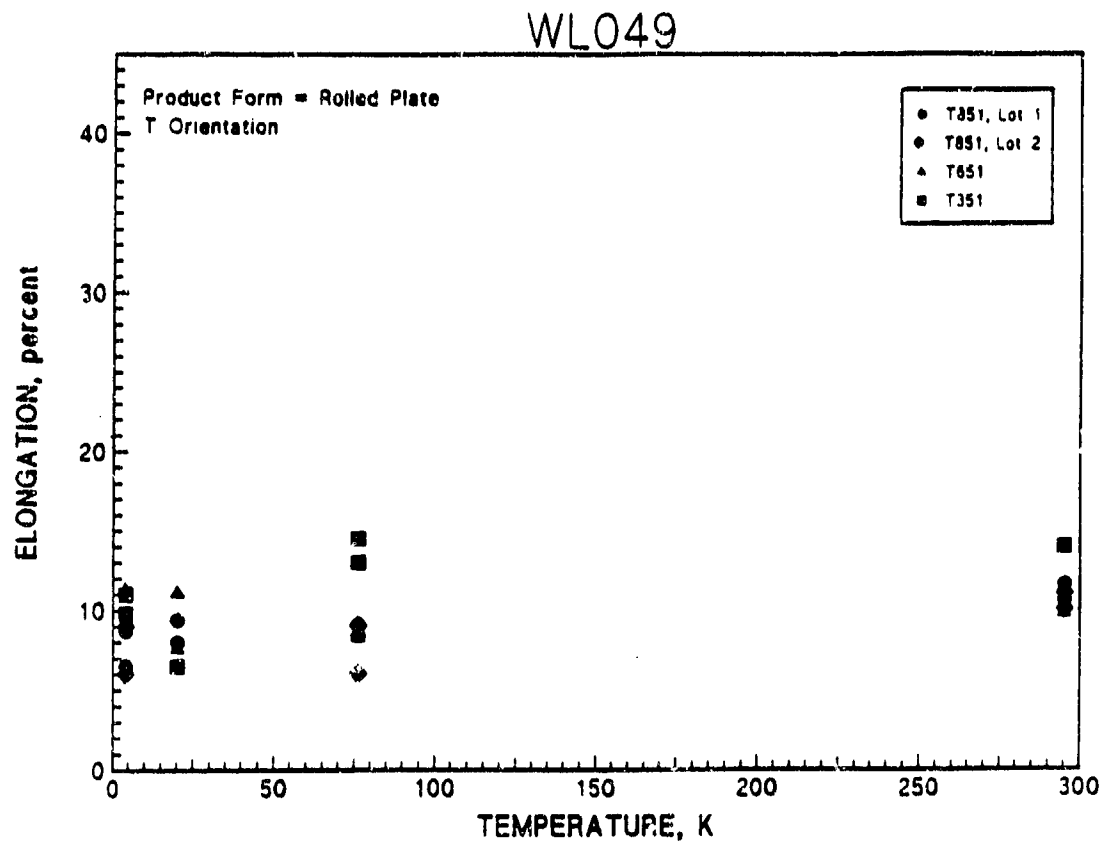
WL049

WL049

Figure 6.16   Tensile elongation versus temperature for WL049,
              T (upper graph) and L (lower graph) orientations.
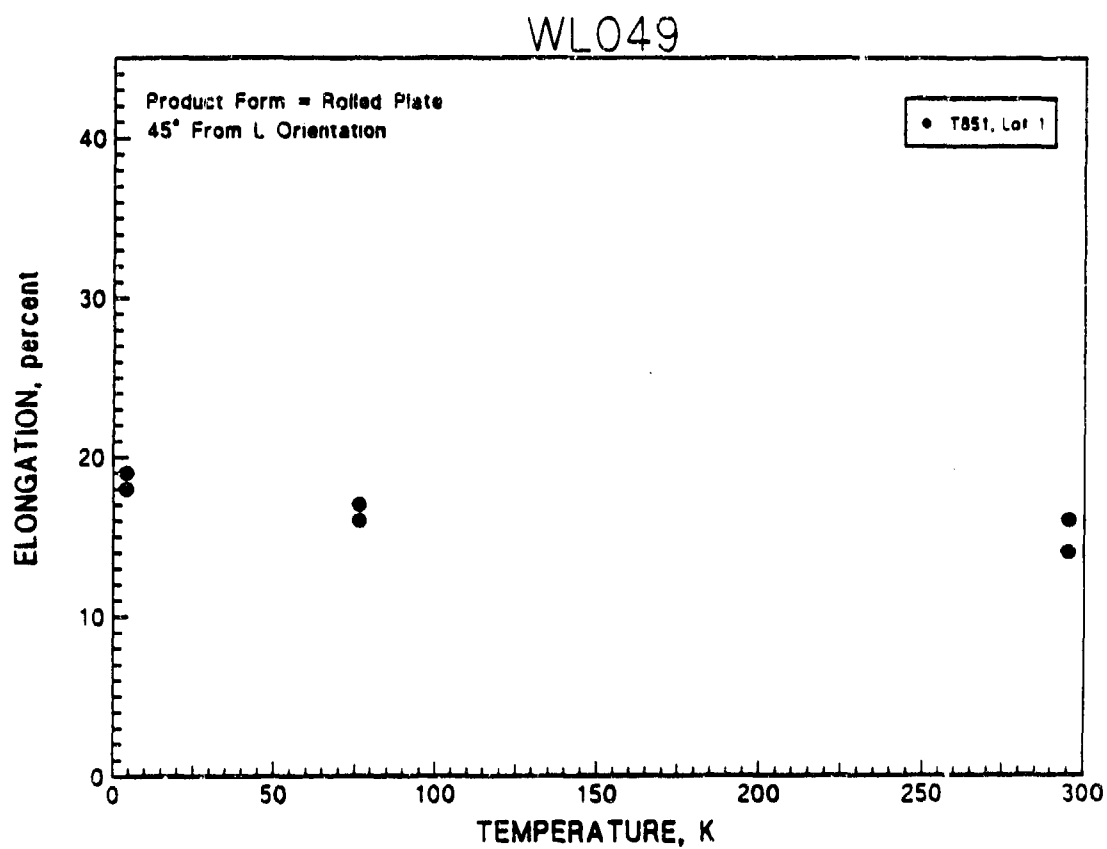
57

WL049

Figure 6.17   Tensile elongation versus temperature for WL049,
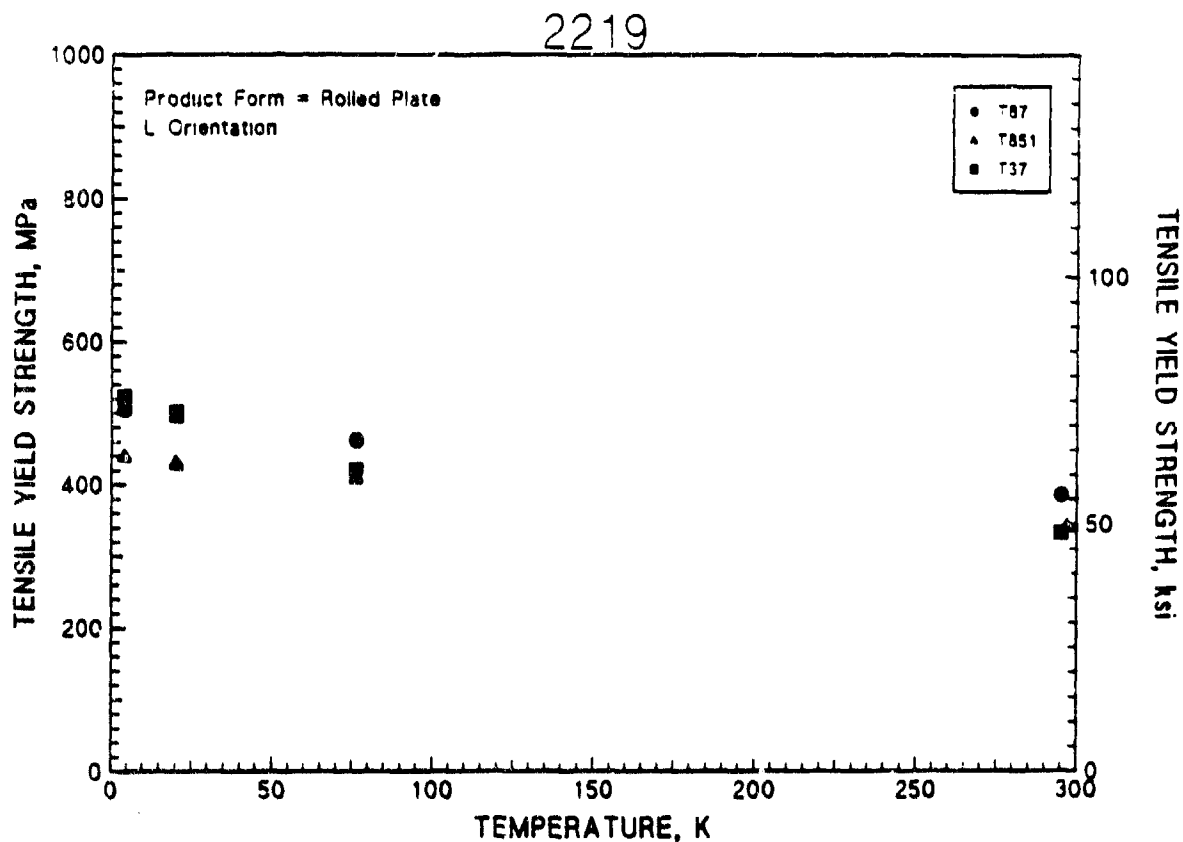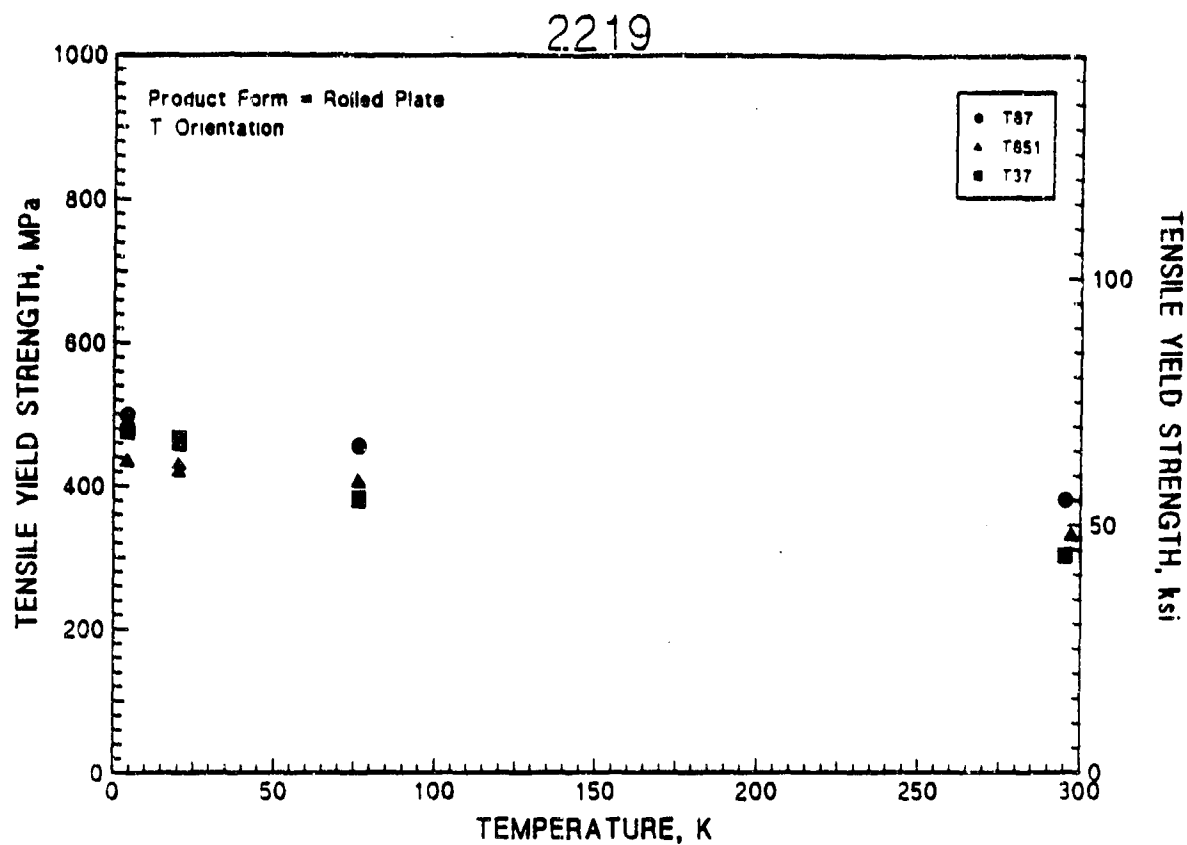45° orientation.

58

Figure 6.18   Tensile yield strength versus temperature for 2219,
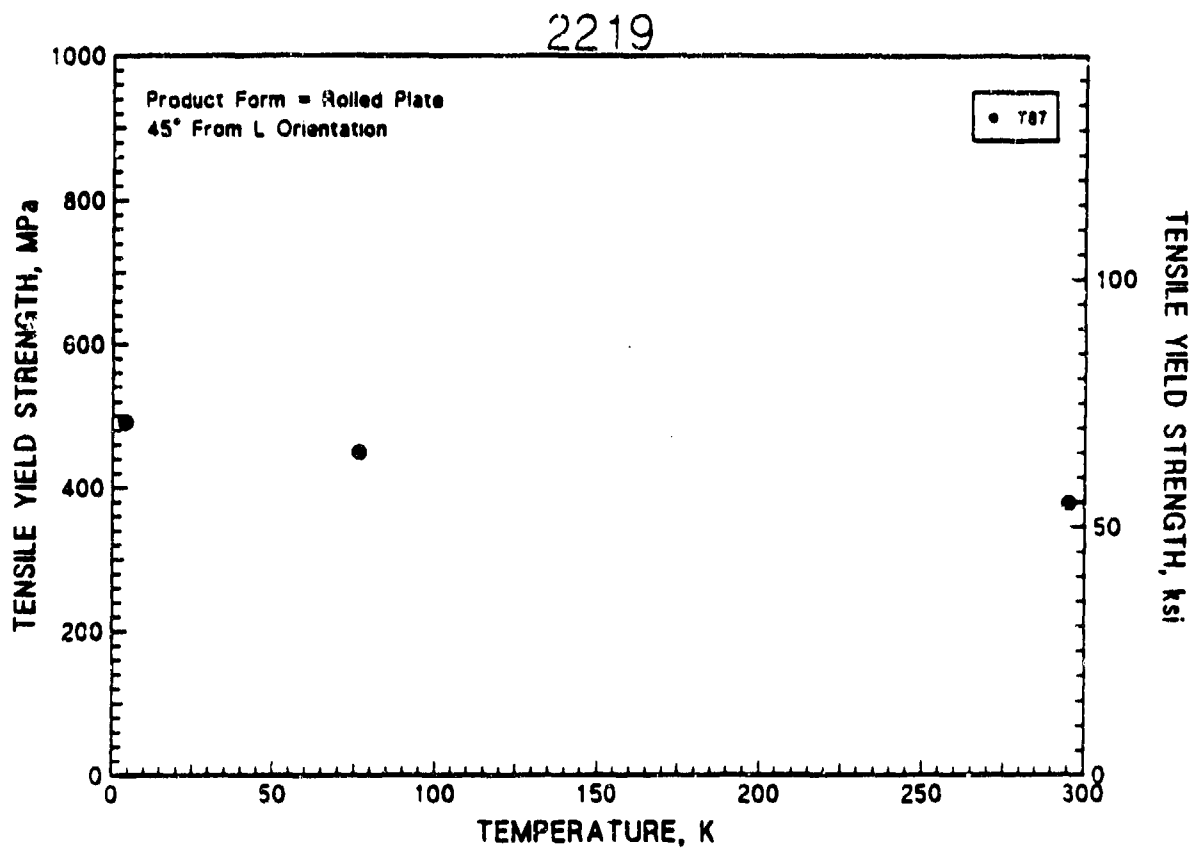T (upper graph) and L (lower graph) orientations.

Figure 6.19   Tensile yield strength versus temperature for 2219,
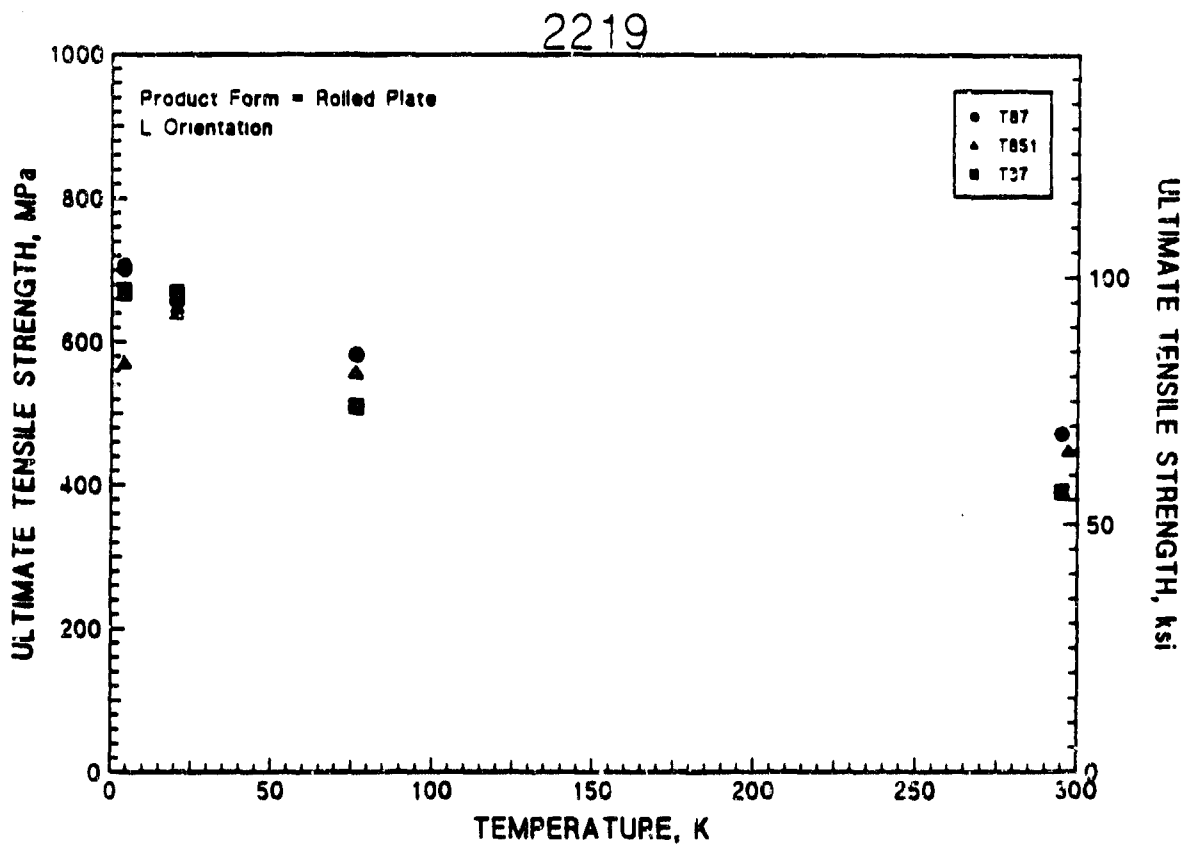   45° orientation.

Figure 6.20   Ultimate tensile strength versus temperature for 2219.
T (upper graph) and L (lower graph) orientations.

Figure 6.21   Ultimate tensile strength versus temperature for 2219,
              45° (upper graph) and S (lower graph) orientations.

Figure 6.22   Tensile elongation versus temperature for 2219,
T (upper graph) and L (lower graph) orientations.

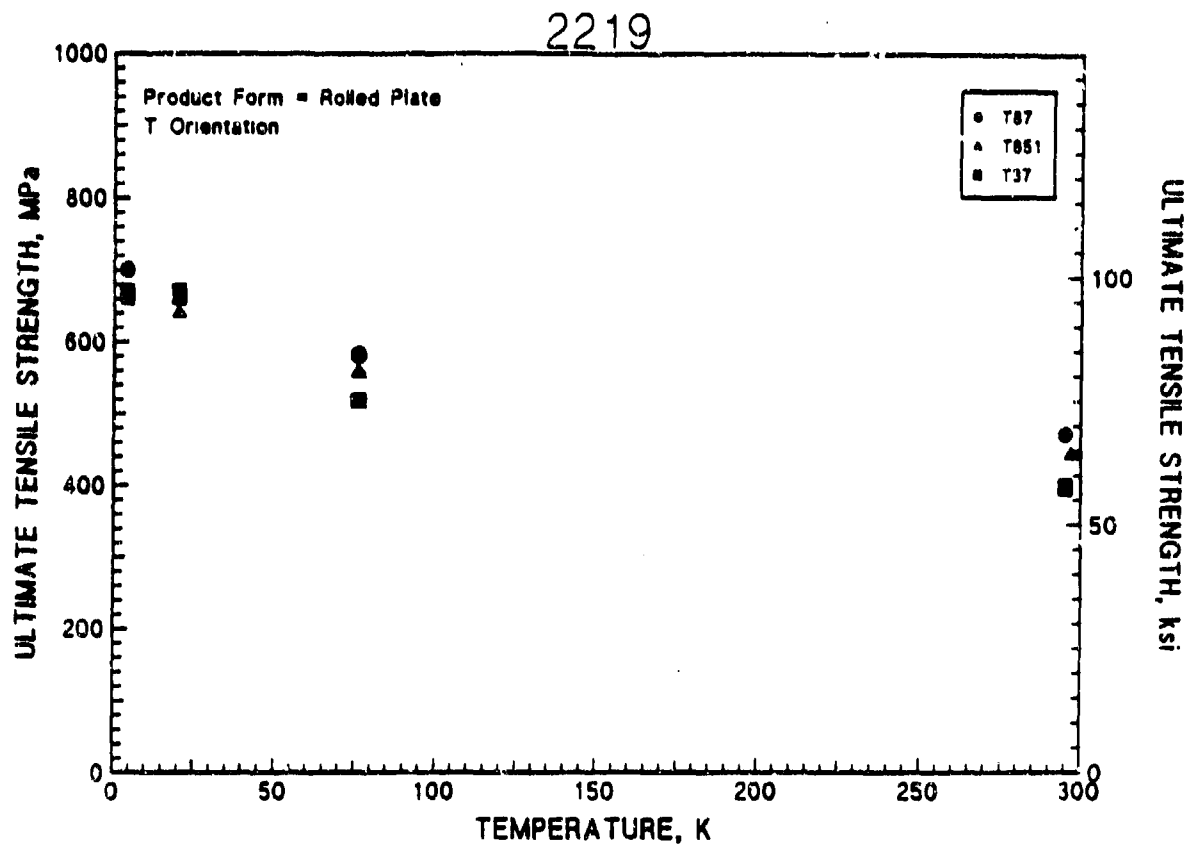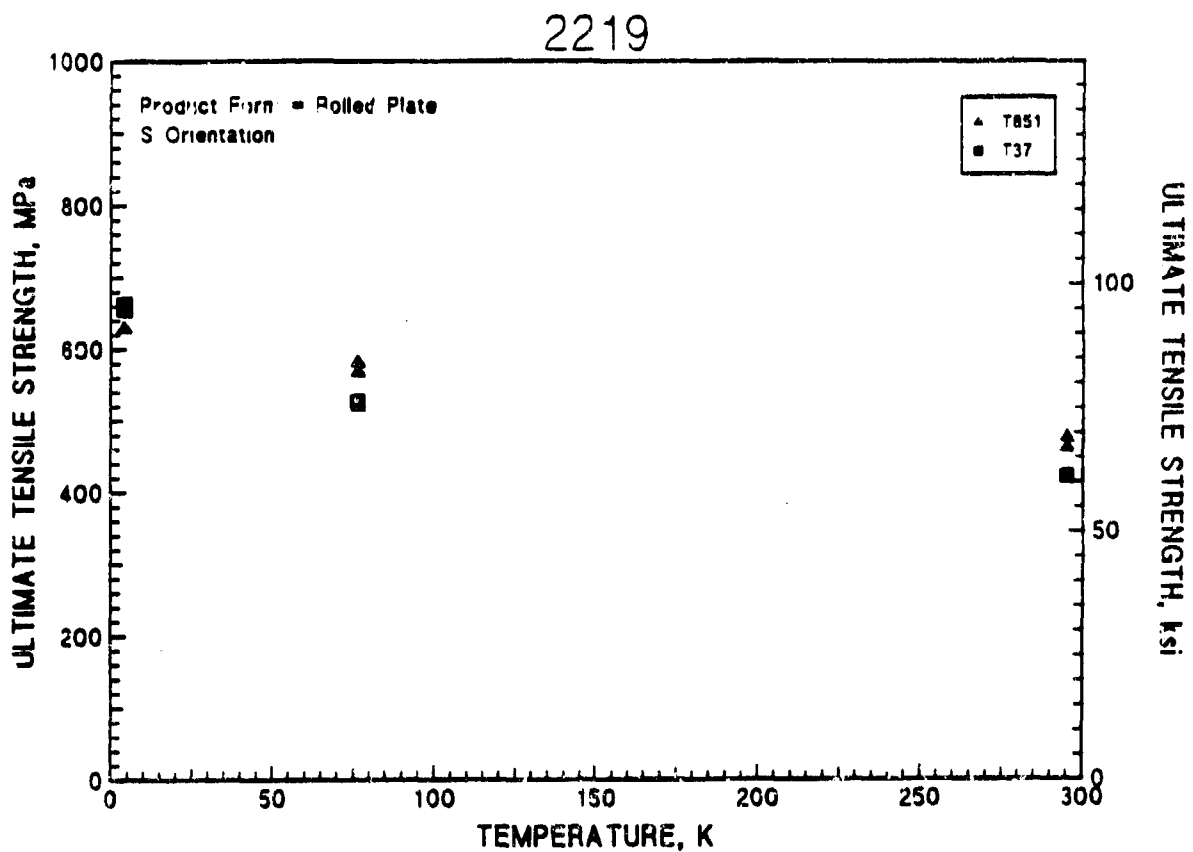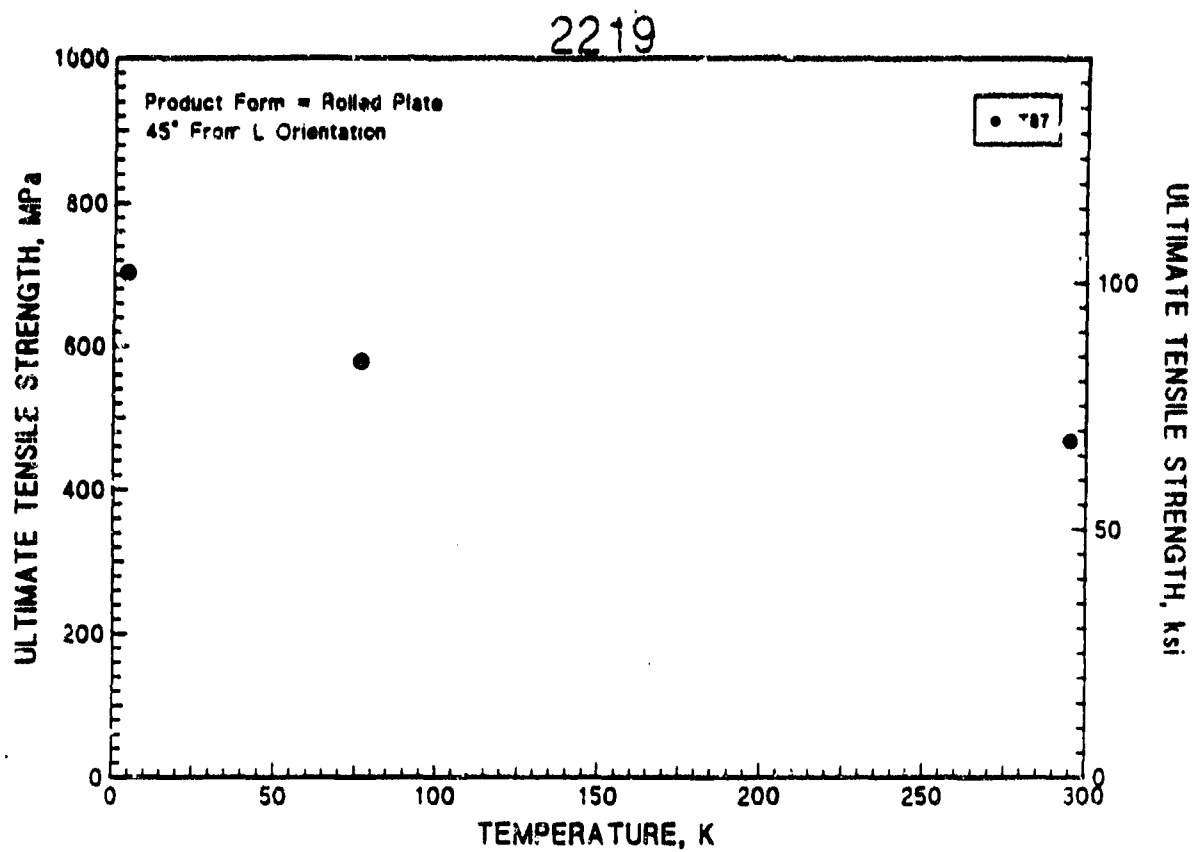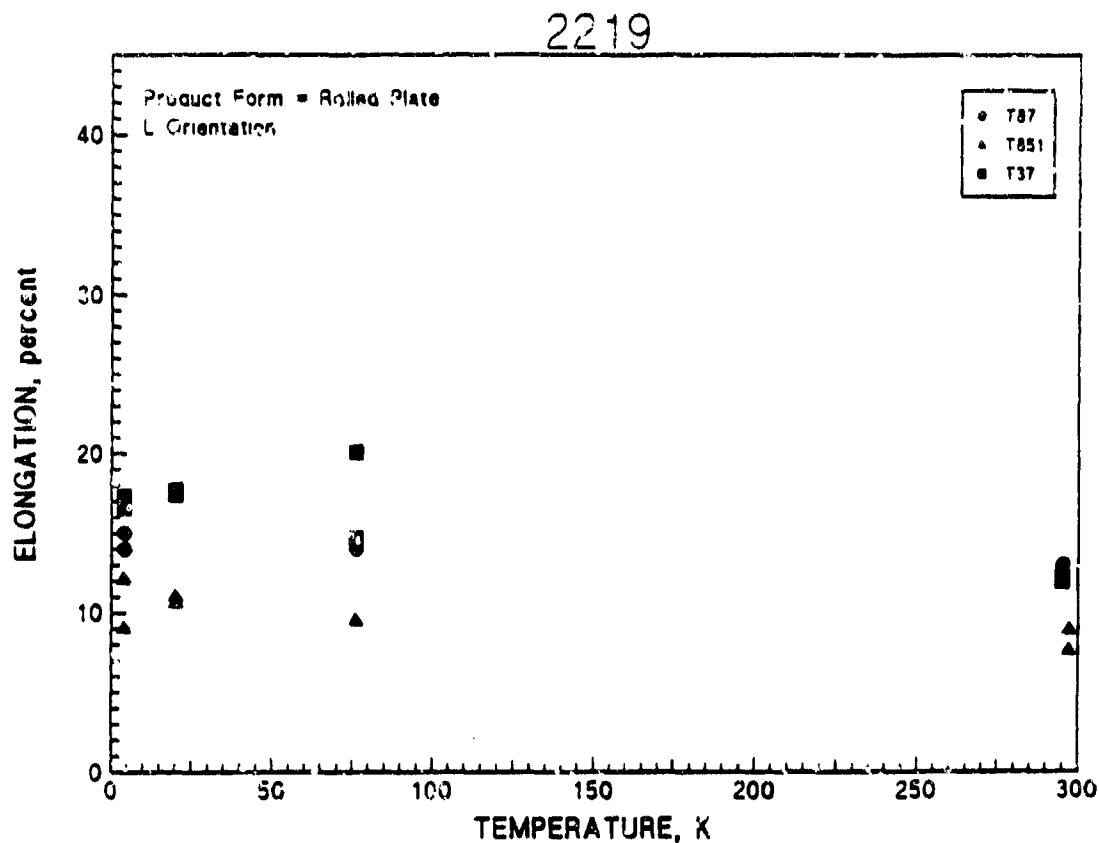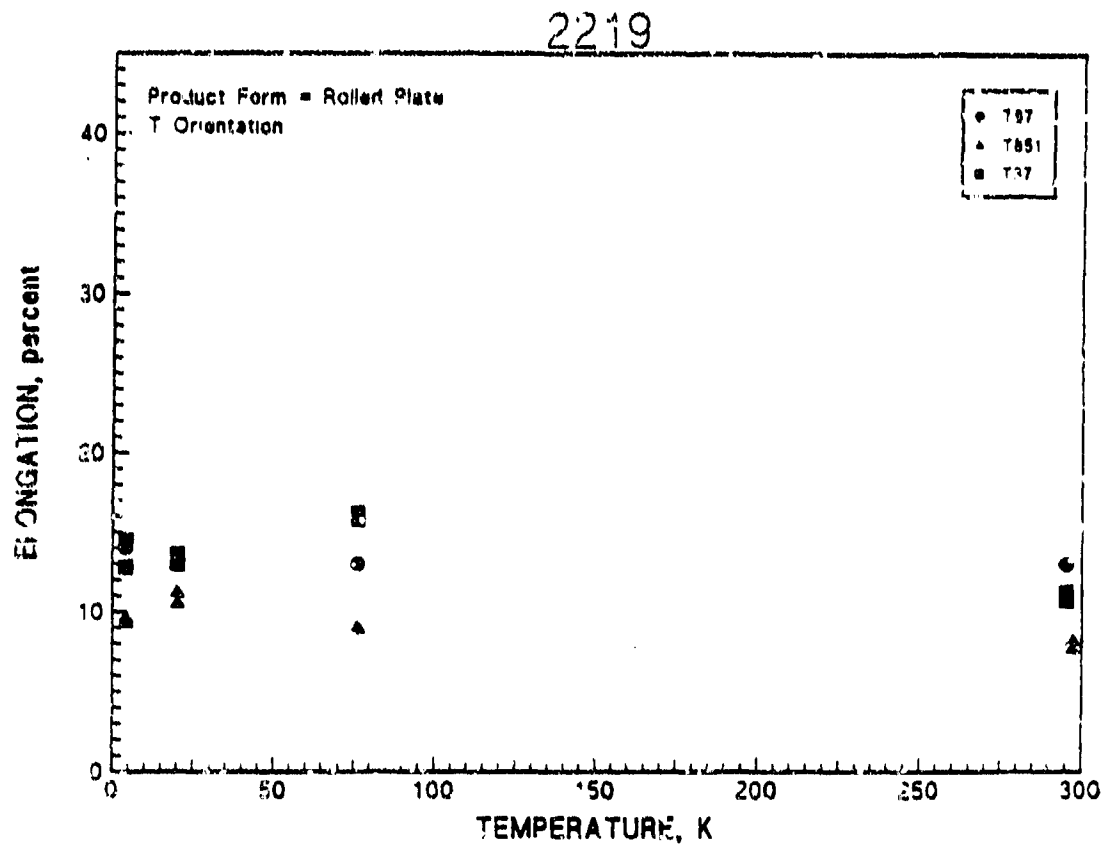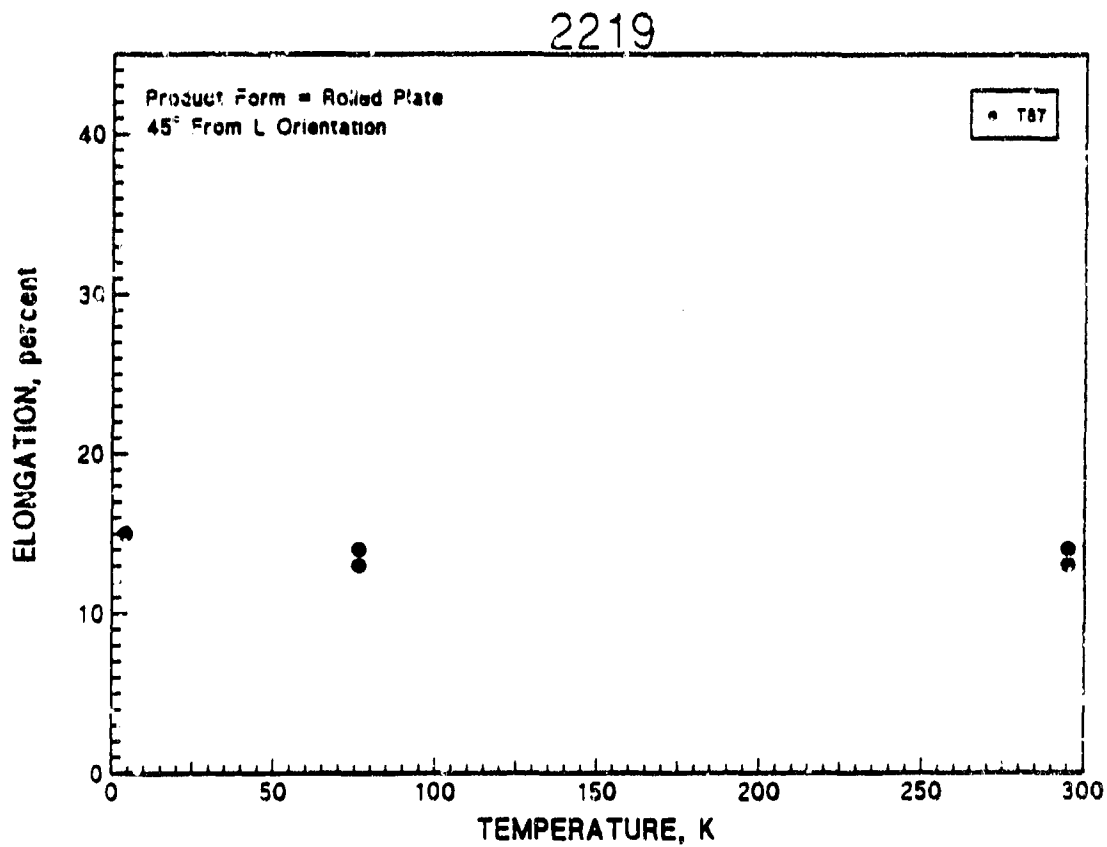Figure 6.23   Tensile elongation versus temperature for 2219,
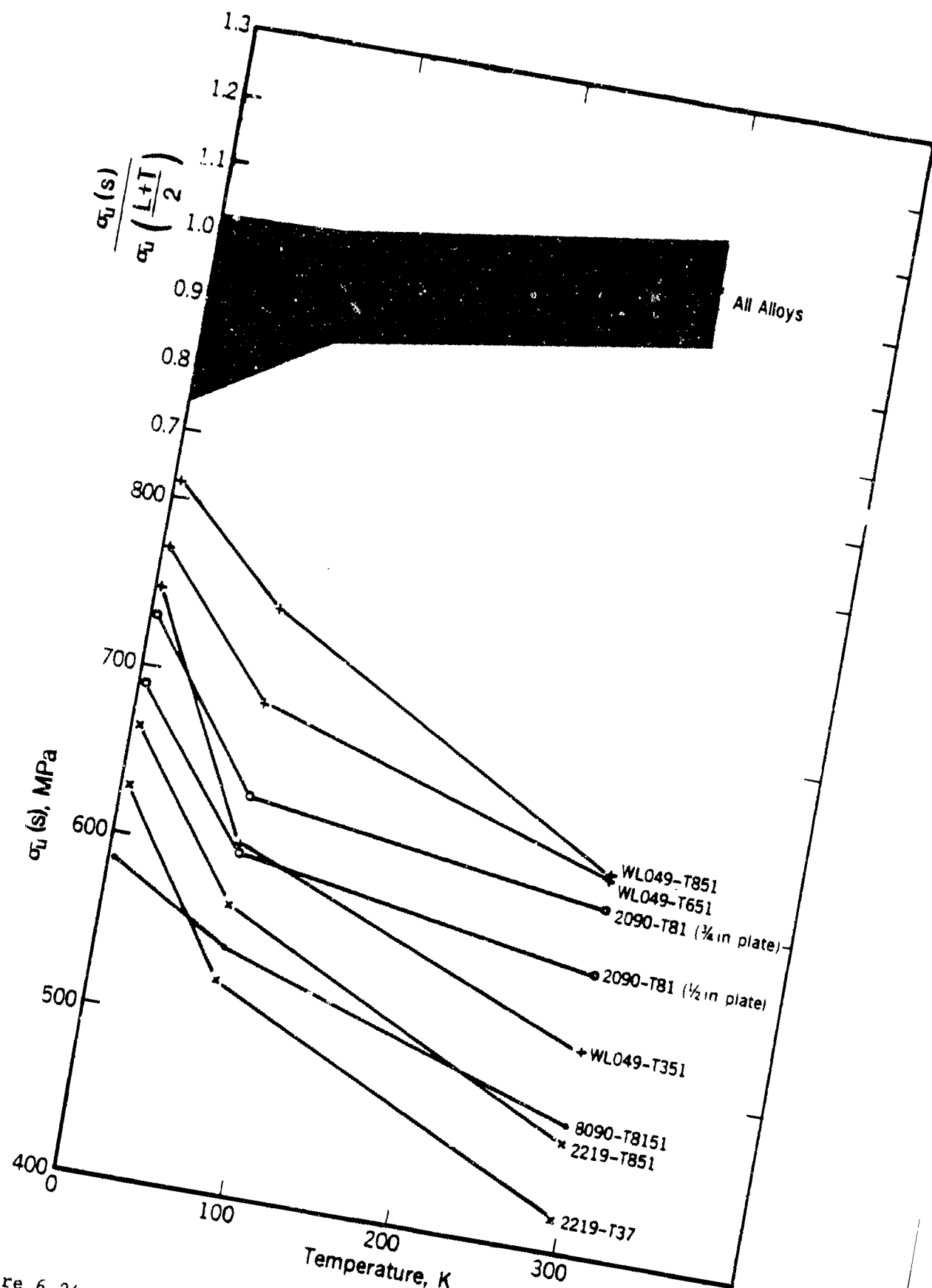45° orientation.

Figure 6.24 Summary of through-thickness ultimate tensile strengths $\sigma_u(S)$ as a function of temperature.

65

In the S orientation, alloy WL049-T851 retains a higher strength than 2090-T81; however, the margin between the two alloys is reduced at least in the present tests on 12.7 mm plate. The ratio $\sigma_u(S)/[\sigma_u(L) + \sigma_u(T)]1/2$ at 4 K is 0.93 for WL049-T851 (lot 1), and 1.02 for 2090-T81.

Tensile tests were also conducted on selected alloys and T8 tempers using specimens machined from the plate at an angle 45° from the L (and T) orientation. In this orientation, strength properties for the Al-Li alloys were found to be less, compared to the L and T orientations. The data are included in Table 6.1 and plotted in Figure 6.25.

There is little dependence on orientation for alloy 2219-T87. The σ_y data for 45° orientation are slightly less (-2%) than the average of the T and L orientations. Yield strengths in the 45° orientation for alloy 2090-T81 are about 10% less than the average of σ_y for the T and L orientations, and about 17% less for alloy WL049-T851. Ultimate strength decreases for these alloys in the 45° orientation are less than the yield strength decreases. At low temperatures, the decreases between the σ_y and σ_u in the 45° orientation compared to the L and T orientations are larger. This temperature dependence suggests that the orientation effects are related to the influence of the preferred orientation of the grain structure on dislocation-precipitate interactions.

Figure 6.25 shows that despite the increased dependence of WL049-T851 on orientation, the absolute values of σ_y remain higher than σ_y of 2090-T81 in the 45° orientation.

General conclusions are summarized below:

- The tensile strengths (σ_y, σ_u) increase with decreasing temperature and are higher for T8 tempers compared to T3 or T6 tempers.

- The tensile strengths (σ_y, σ_u) are highest for WL049-T851, followed by 2090-T81, then 8090-T8151. All Al-Li alloys have higher tensile strengths than alloy 2219 in corresponding tempers.

- The tensile properties of WL049 exhibit greater sensitivity to orientation than 2090 and 8090; there are larger disparities between the values measured in the L and T orientations (L has larger values), and greater decreases in the values measured in the 45° orientation and in the S orientation.

6.1.3 Ductility

The tensile elongation and reduction of area data for all alloys, temperatures, and tempers are reported in Table 6.1 and Figures 6.5, 6.10, 6.11, 6.16, 6.17, 6.22, and 6.23.

Contrary to the conclusions of earlier studies, it is difficult to generalize about the temperature dependence of the tensile ductility of Al-Li alloys. Usually the elongation to failure in the L orientation increases at lower temperatures (the exception is the second lot of WL049-T851).
In the T orientation, the elongation to failure also increases with decreasing temperature for all tempers of alloys 8090 and 2219, however, the
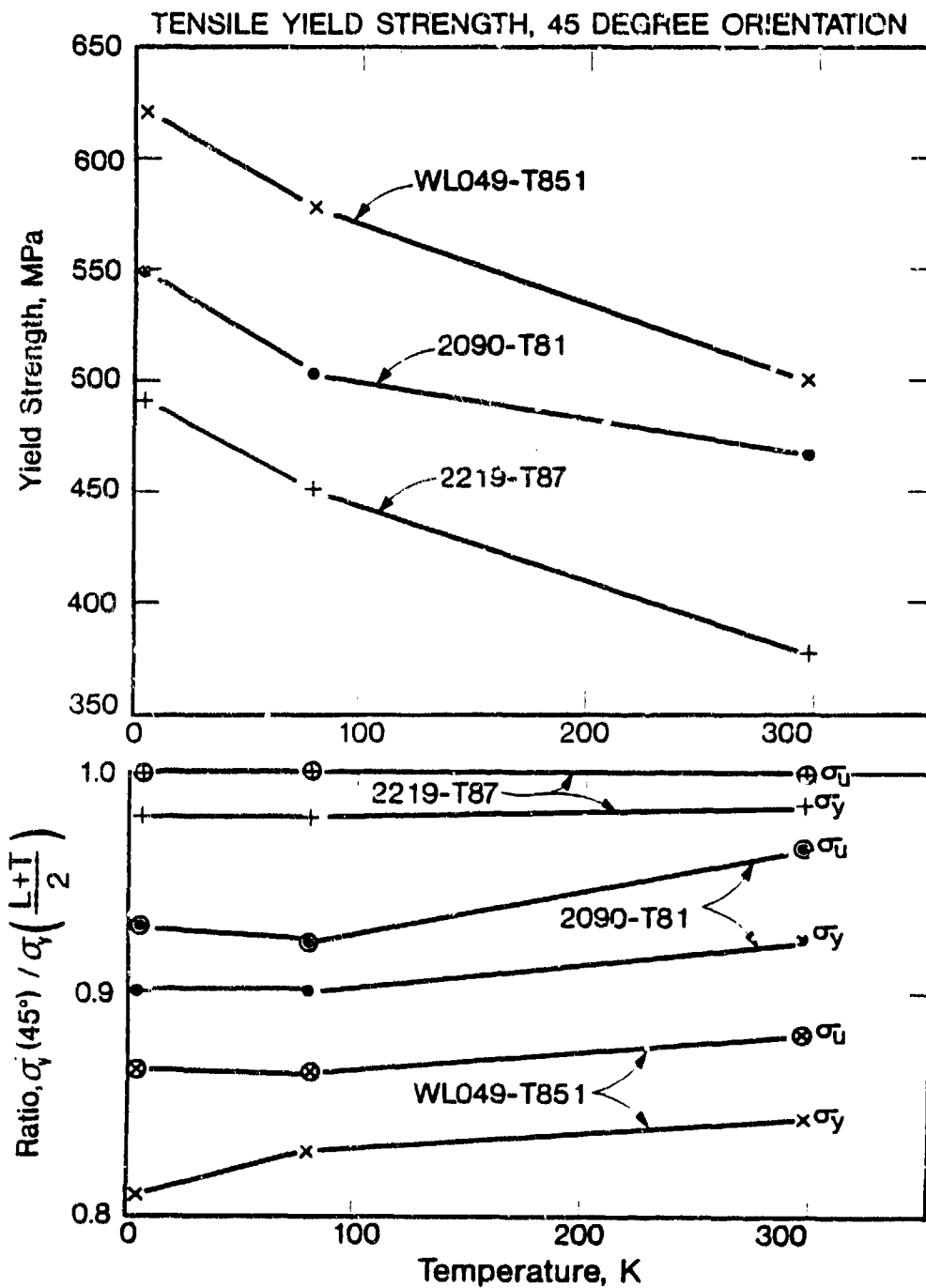
Figure 6.25 Summary of tensile yield strength in the 45° orientation as a function of temperature for T8 tempers of Al-Li alloys.

elongation of alloys 2090 and WL049 (in all tempers) decreases with decreasing temperature in this orientation.

Tensile elongation is very low at all temperatures for 2090-T81 (1-2%) in the T orientation from 12.7 mm thick plate for the same orientation from the 19.1 mm thick plate; the elongation ranges from 2.5 to 5%. The elongation is much higher (6-15%) for WL049-T851 at all temperatures. Alloy 8090, in all tempers, showed the largest increases of elongation at lower temperatures. For example, the elongation of the T8771 temper in the L orientation increased from only 3% at 295 K to 13% at 4 K.

There has been much conjecture on the reasons for increased ductility of face-centered cubic metals and alloys at low temperatures. Recently, Glazer et al.[9] suggested that, for Al-Li alloys, specimen necking occurs when the true stress in the specimens reaches the strain-hardening rate. They plot strain-hardening rate and true stress for 2090-T81, L orientation, versus true strain to illustrate the coincidence of the two values at tensile failure.

There is a simple explanation for the extension to larger strains of the convergence of true stress and strain-hardening rates as the temperature is lowered. The primary failure mechanism in face-centered cubic metals at room and low temperatures is microvoid coalescence. At low temperatures, vacancy diffusion rates per unit deformation are much lower unless they are stress-assisted (stresses are higher at lower temperatures). The temperature dependence of the diffusion coefficient is proportional to $e^{-Q/RT}$ where Q is regarded as an activation energy for the diffusion event (see, e.g., Shewmon[10]). The reduced diffusion rates lead to retardation of vacancy migration, necessary for the formation of voids and for subsequent void growth. Thus, coalescence of voids to form microcracks is delayed at lower temperatures, leading to delayed fracture (increased toughness).

The distinctions between the elongation behavior of alloys 2090-T81 and WL049-T851 in the 45° orientation are interesting. In 2090-T81, elongations (3.5%) at 45° are intermediate between the high values (7-12%) of the L orientation and the low values (1-2%) of the T orientation. In WL049-T851, elongation values at 45° are considerably larger (12-17%) than in the T or L orientations (9-11%). (The strengths of both alloys are lower in the 45° orientation compared to T and L orientations). The other distinction between the two alloys, with respect to tensile ductility is that WL049 has equivalent elongations in the L and T orientations while 2090-T81 has severe degradation of the elongation in the T orientation compared to the L orientation.

6.1.4 Stress-Strain Curves

Engineering stress-strain curves are presented in Figures 6.26-6.35 and true stress-strain curves are shown in Figures 6.36-6.41. Only curves at 4, 76 and 295 K are included. Discontinuous yielding (serrations) at 4 K is prevalent. At 20 K, there is very limited serrated yielding and the stress-strain curves fall within the range of the serrations of the 4 K curves. Therefore, because of the overlap of the 4 and 20 K curves, the 20 K curves were omitted for clarity.
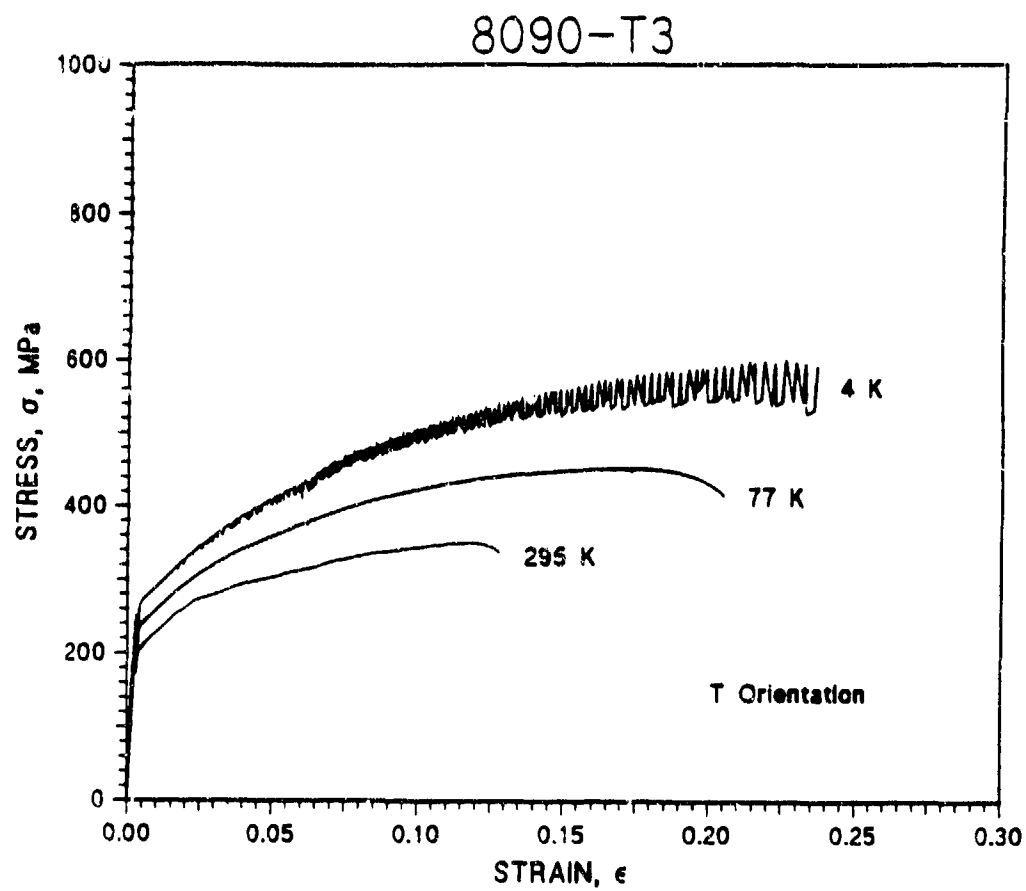
Figure 6.26 Engineering stress-strain curves for 8090-T3, T orientation.

Figure 6.27 Engineering stress–strain curves for 8090–T8151,
L orientation.

Figure 6.28   Engineering stress-strain curves for 8090–T8771,
L orientation.

Figure 6.29   Engineering stress-strain curves for 2090-T81,
             L orientation, 12.7 mm plate.

Figure 6.30   Engineering stress–strain curves for WL049–T351,
              T orientation.

Figure 6.31   Engineering stress-strain curves for WL049-T651,
               L orientation.
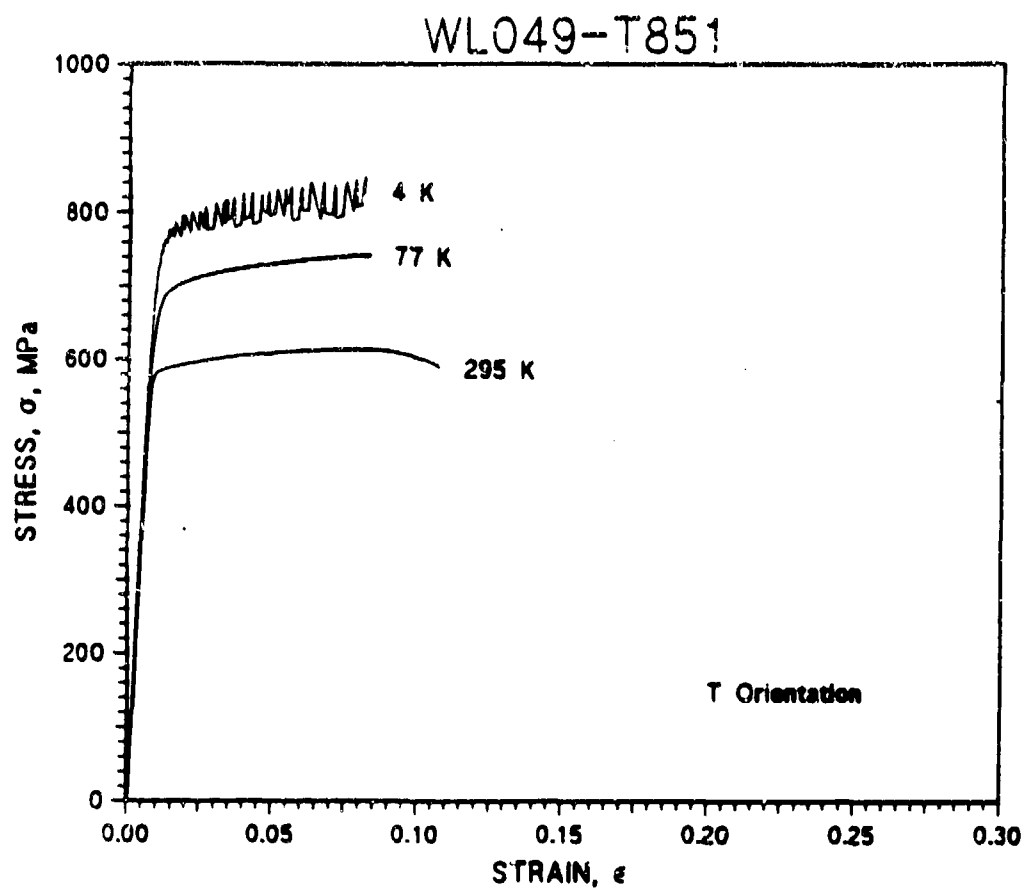
Figure 6.32   Engineering stress-strain curves for WL049-T851,
                T orientation.
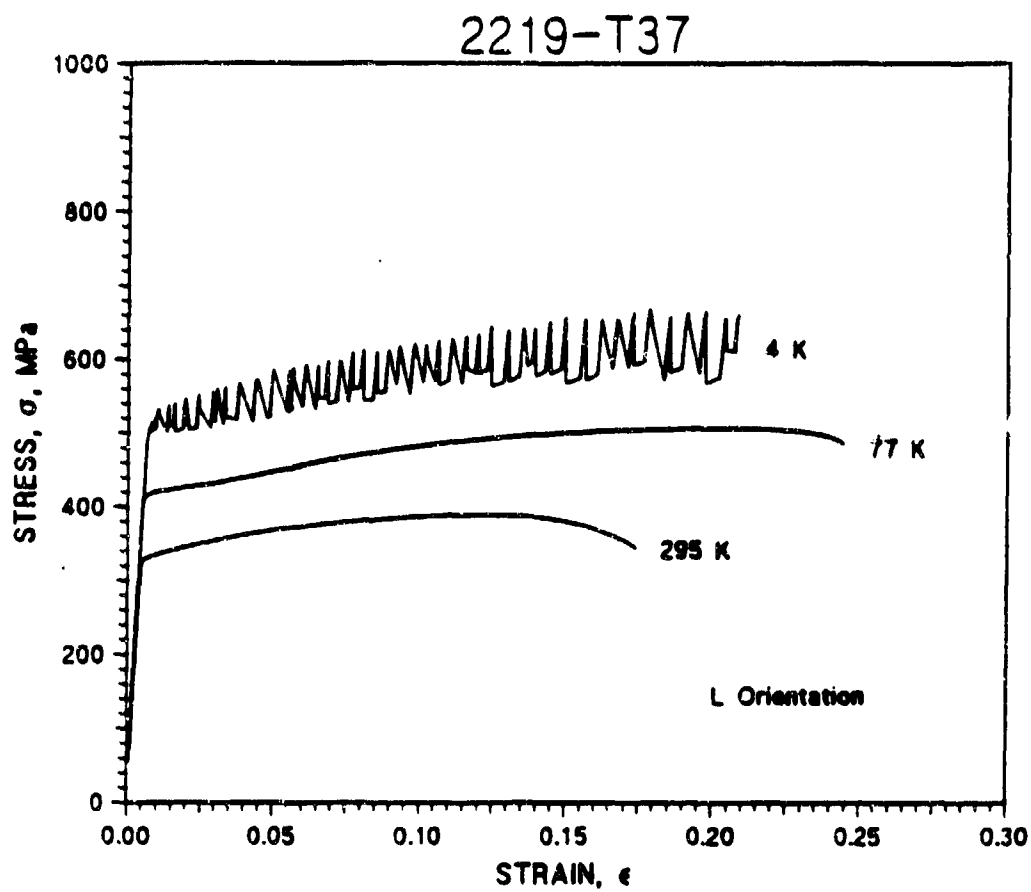
2219-T37

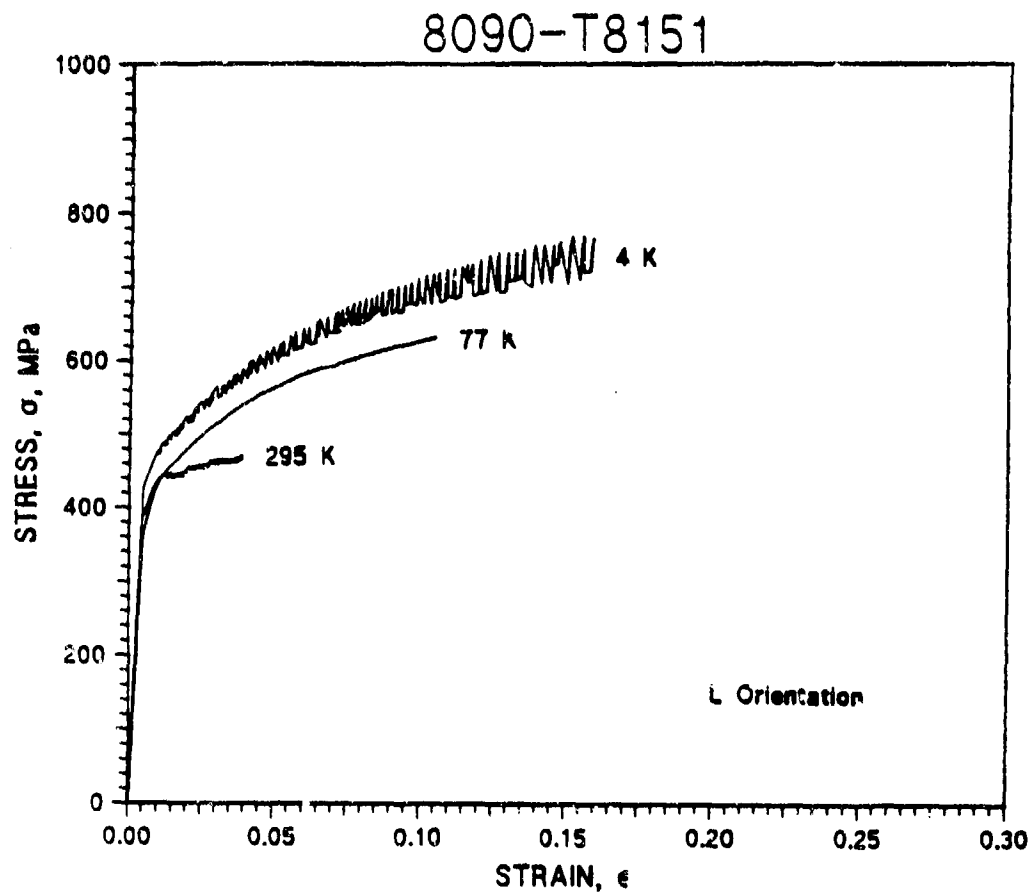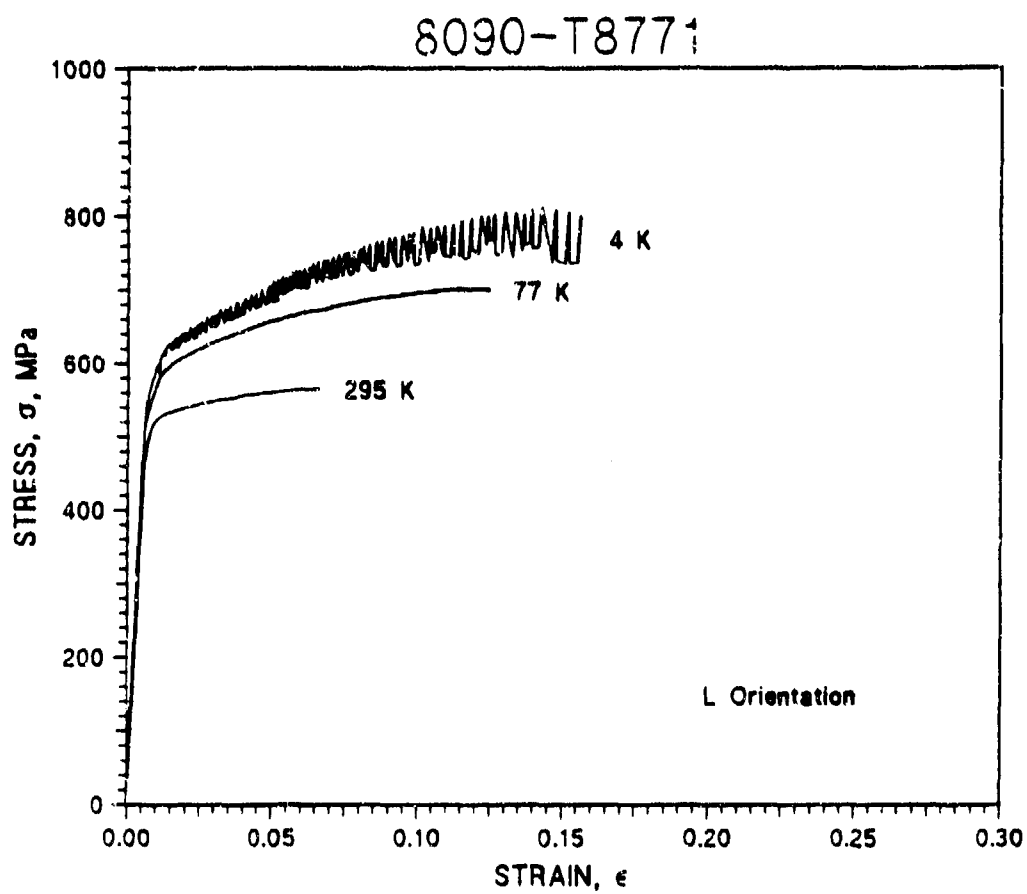Figure 6.33 Engineering stress-strain curves for 2219-T37,
T orientation.

76
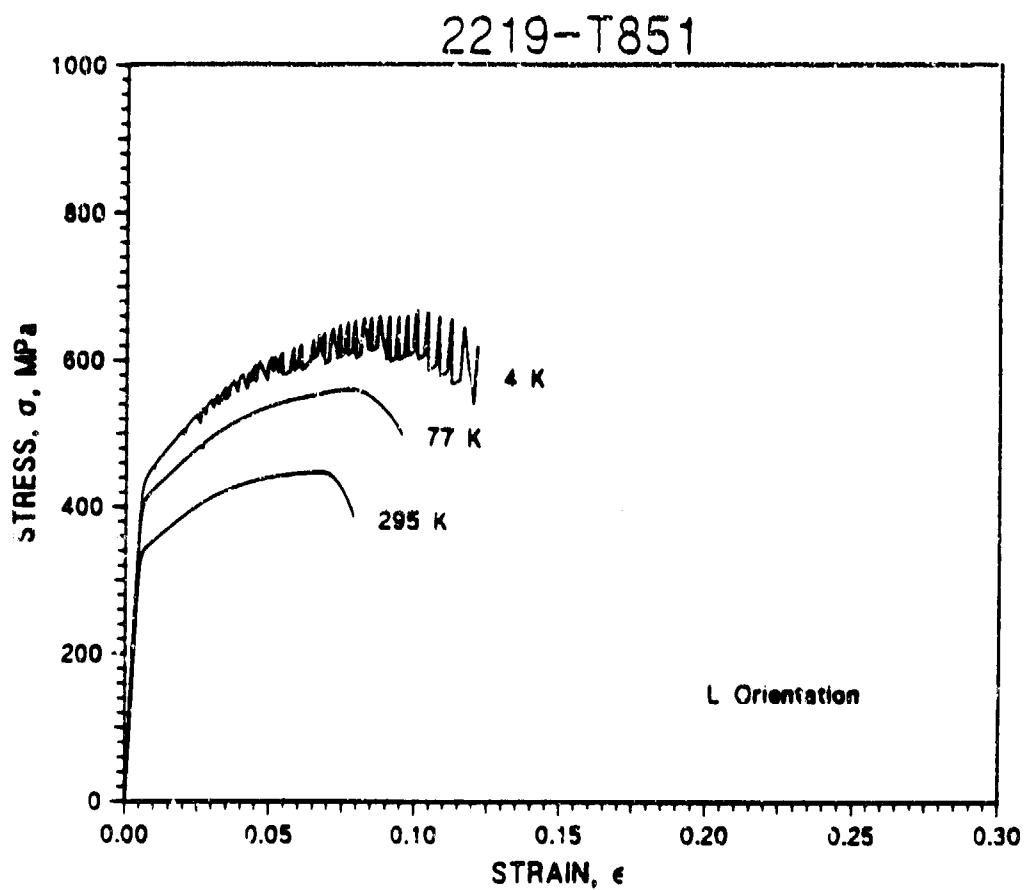
Figure 6.34   Engineering stress-strain curves for 2219-T851,
L orientation.
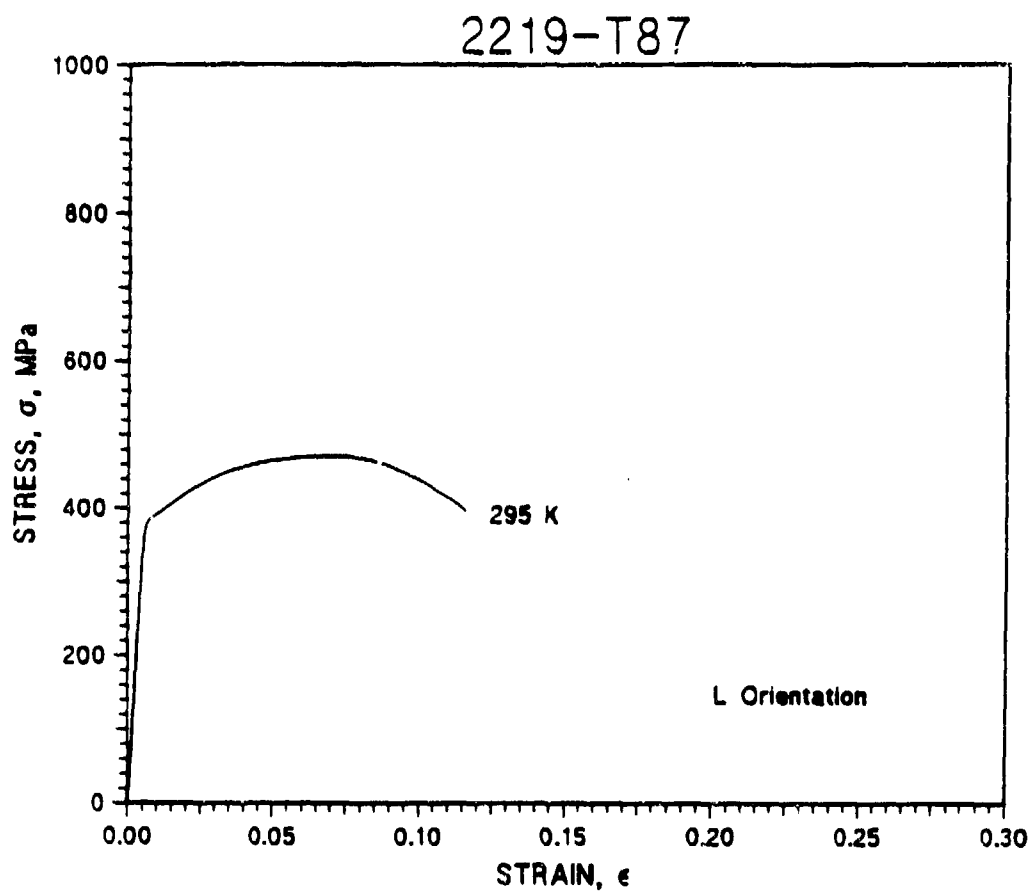
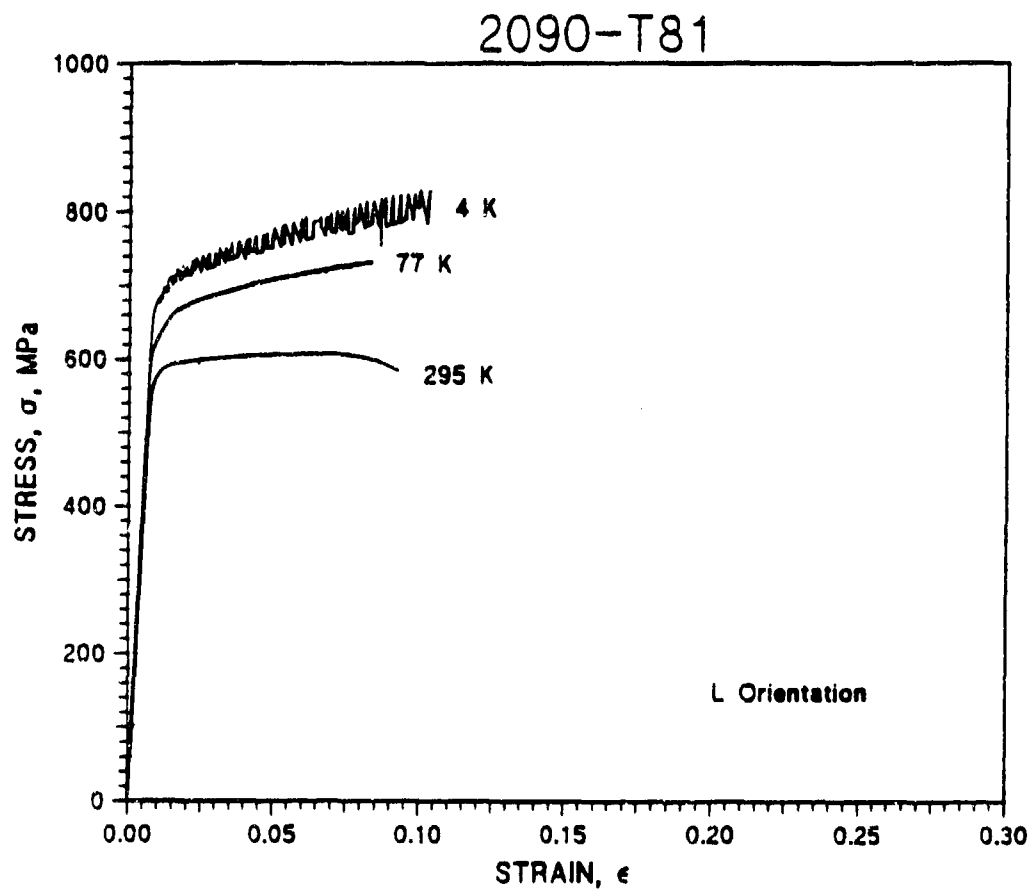Figure 6.35 Engineering stress-strain curves for 2219-T87, L orientation.
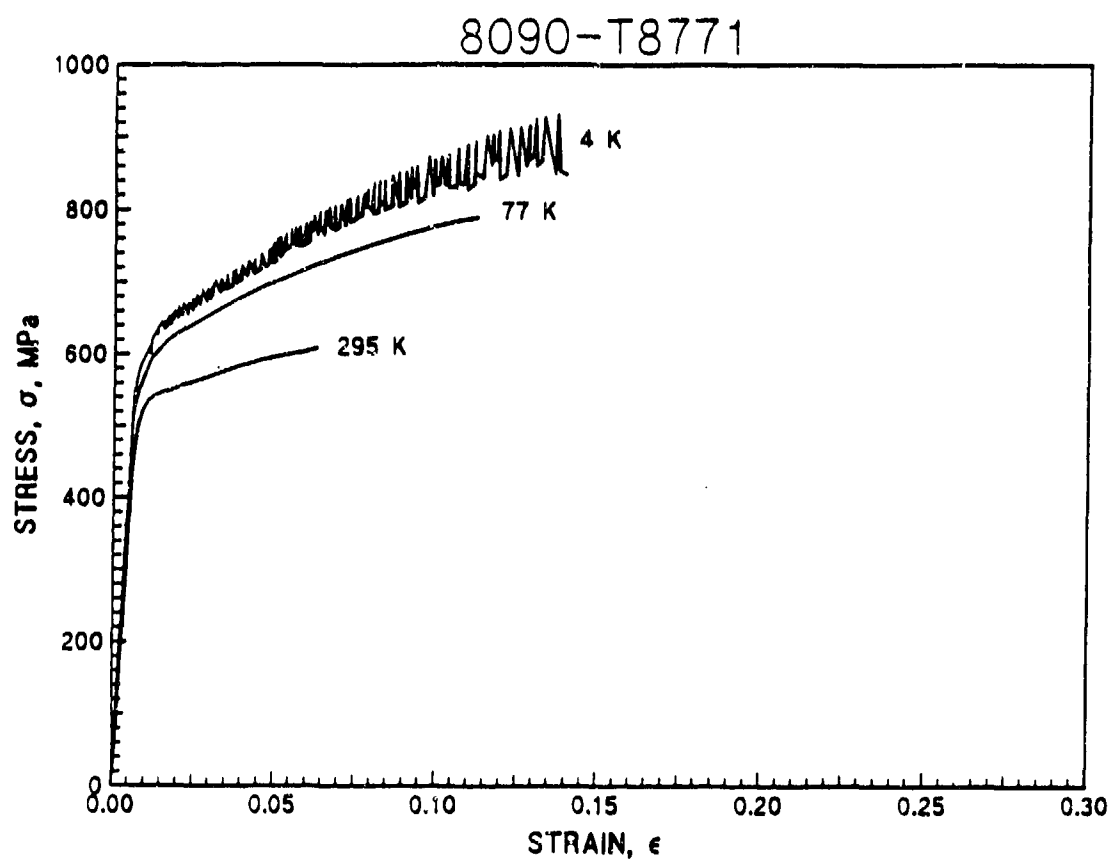
Figure 6.36 True stress-strain curves for 8090-T8771,
          L orientation.
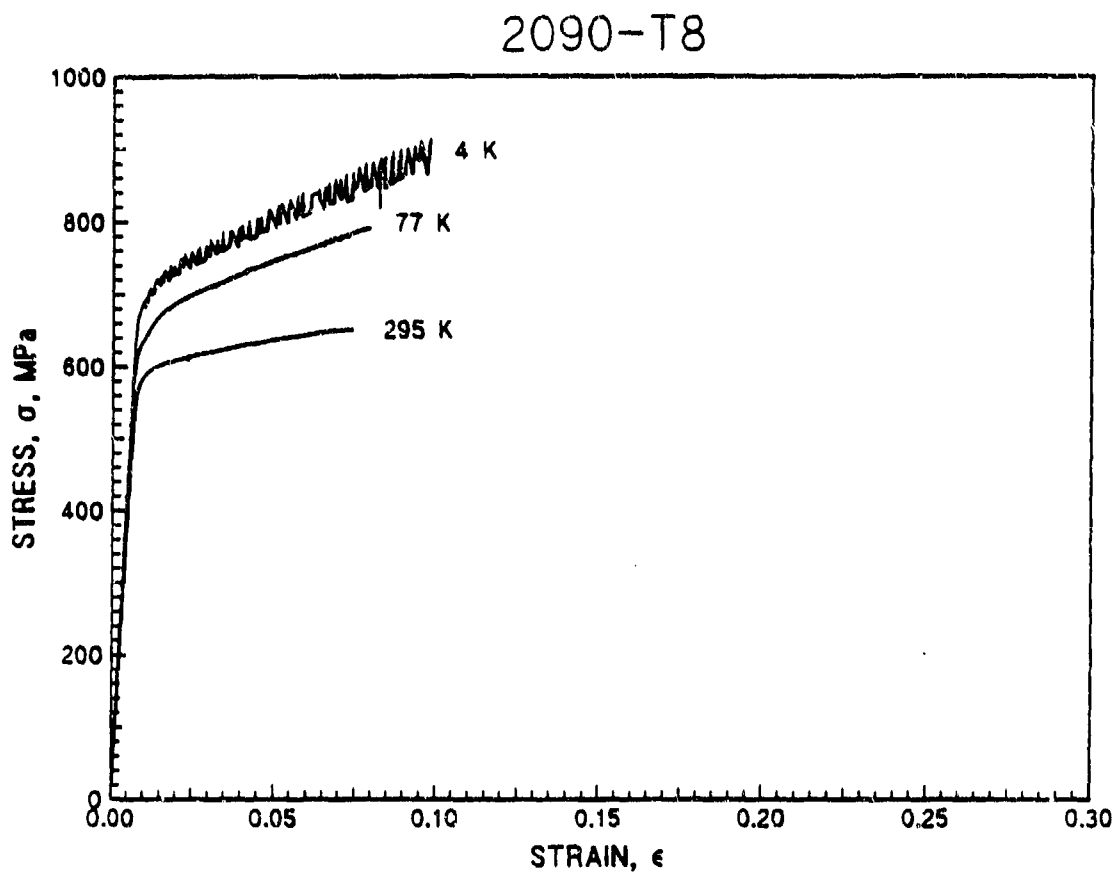
2090-T8

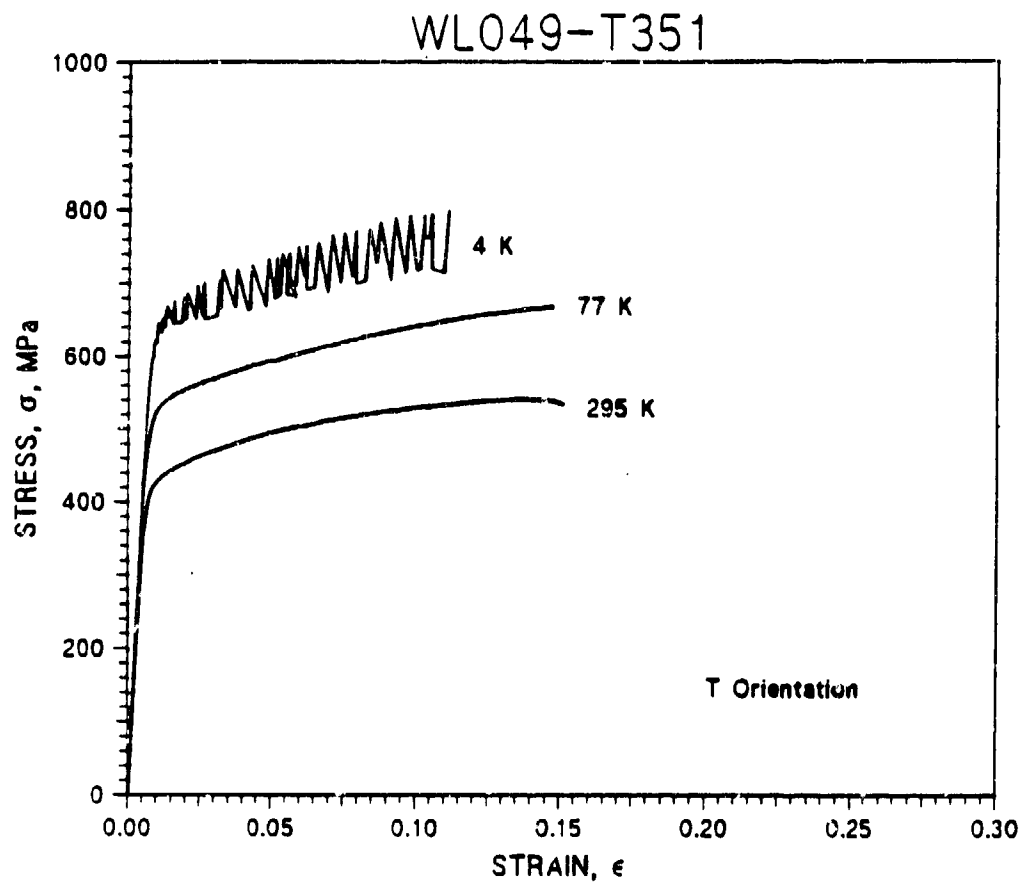Figure 6.37   True stress-strain curves for 2090-T81,
L orientation, 12.7 mm plate.

WL049-T351

Figure 6.38   True stress-strain curves for WL049-T351,
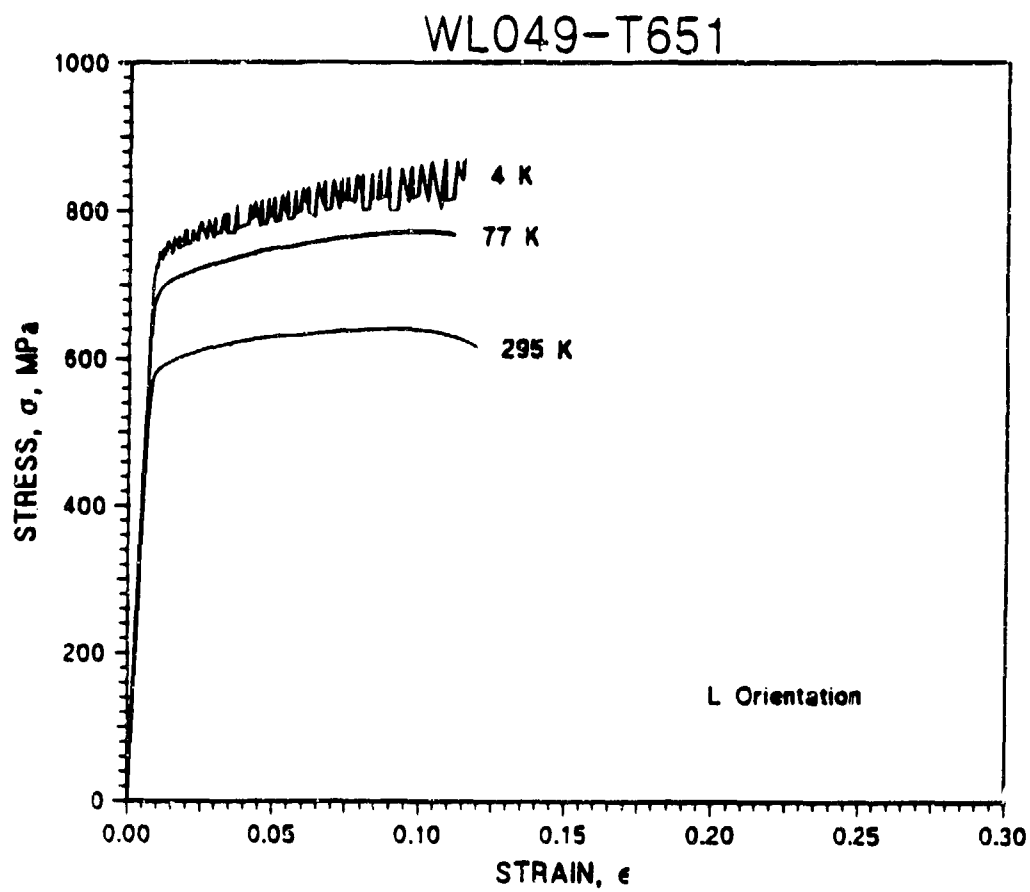   L orientation.

WLO49-T851

Figure 6.39 True stress-strain curves for WLO49-T851,
T orientation, lot 1. Curves not completed
to failure.

Figure 6.40   True stress-strain curves for 2219-T37,
             L orientation.

2219-T851

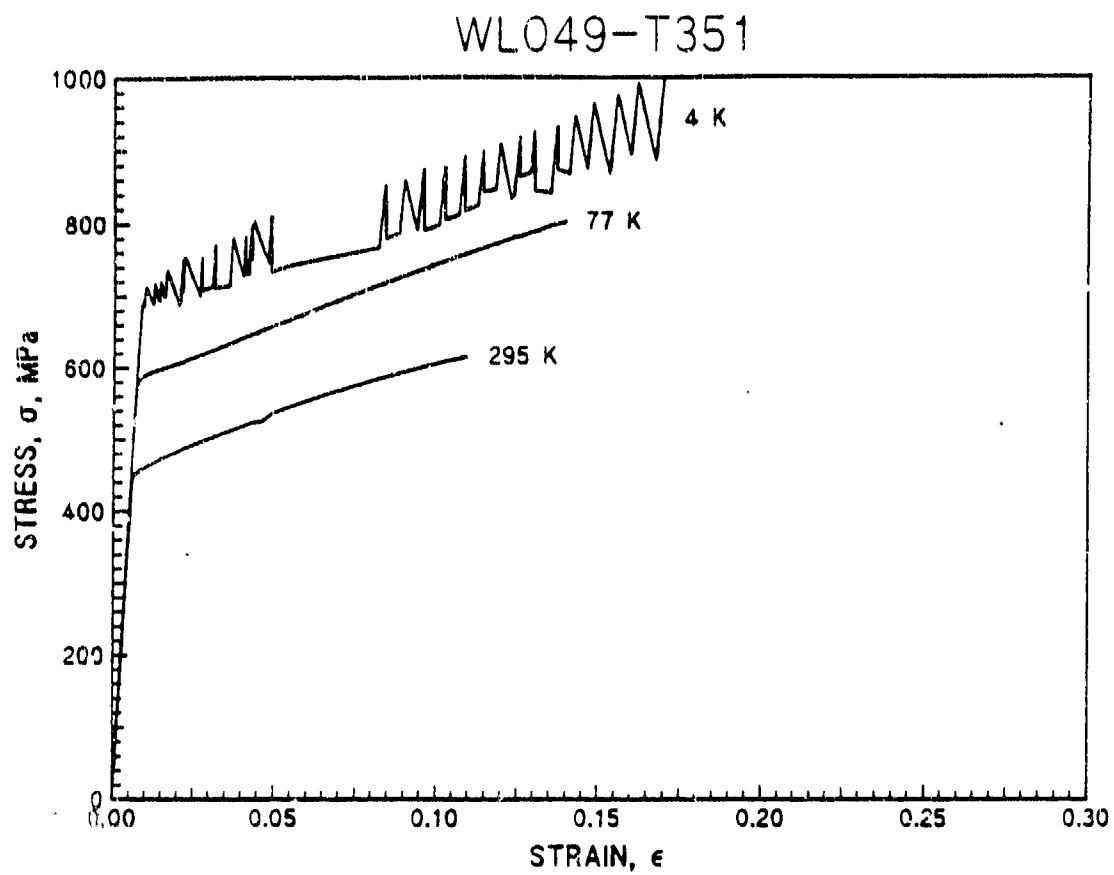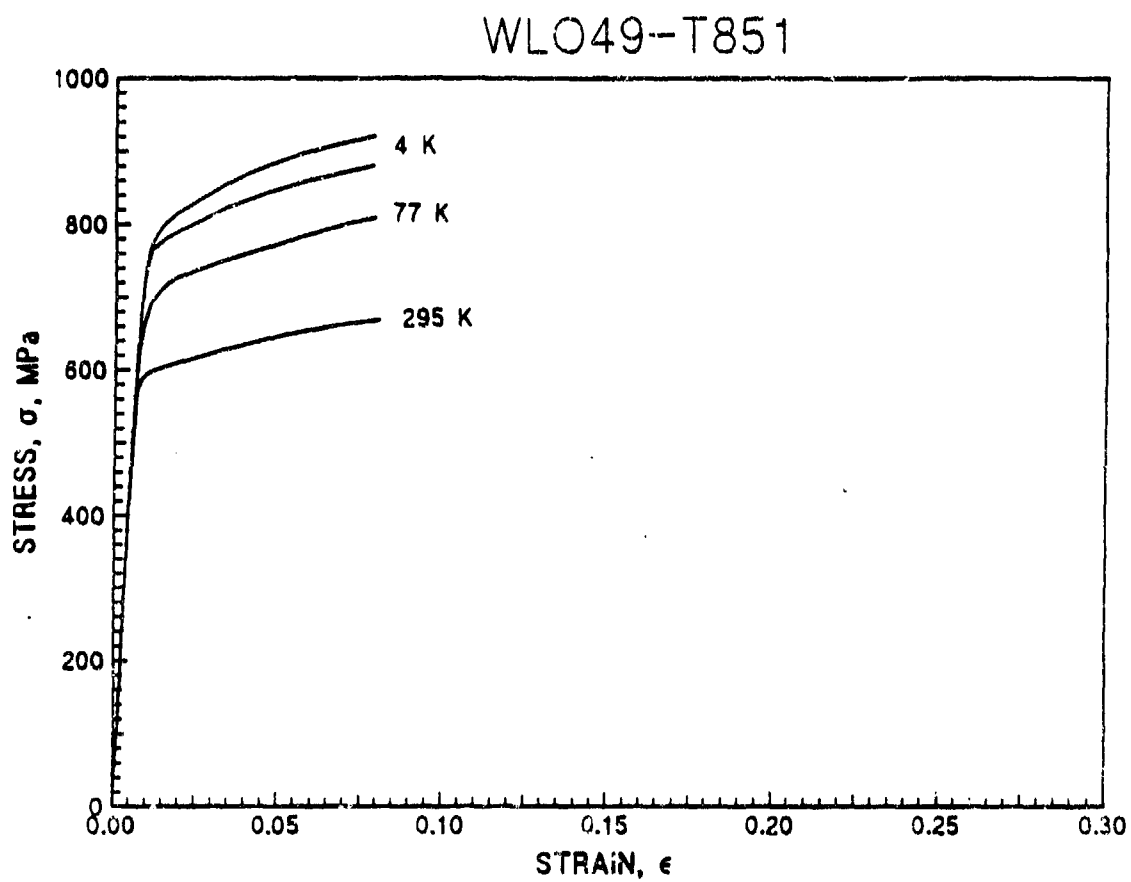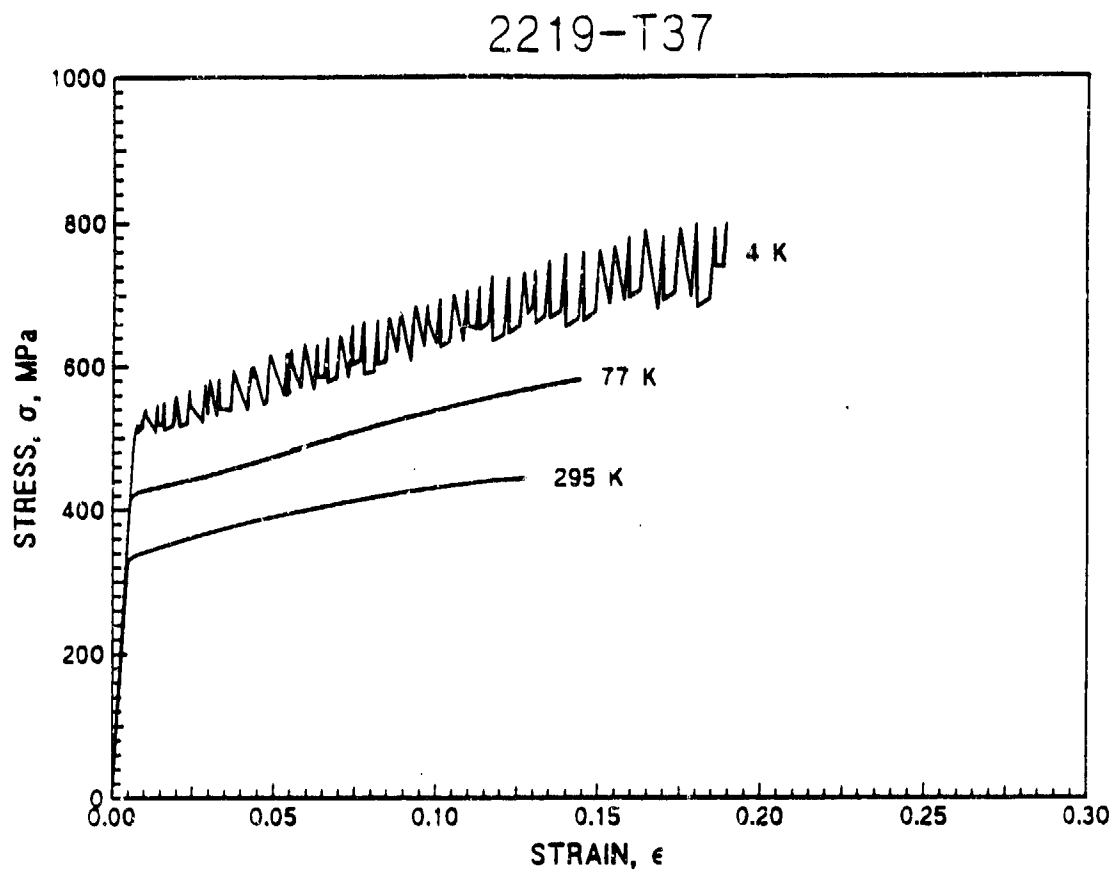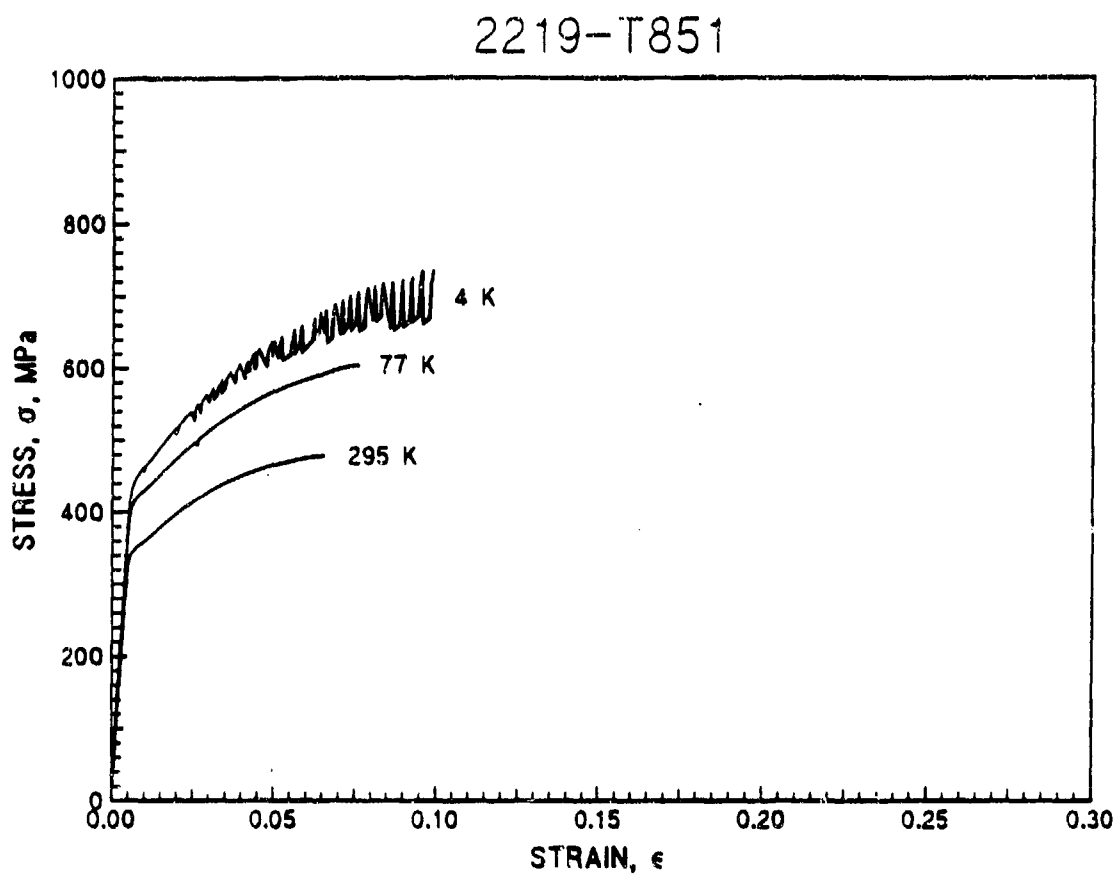Figure 6.41   True stress-strain curves for 2219-T851,
                L orientation.

Discontinuous yielding was observed in all tests conducted at 4 K. This phenomena is associated with the inability to transfer the heat out of the deforming specimens faster than it is generated.[11,12] Therefore, the nature of discontinuous yielding depends on strain rate, specimen configuration, test environment (liquid or gas), and alloy. To initiate discontinuous yielding, the rate of work input must exceed the rate of heat transferred out of the specimen to the coolant and specimen grips and the amount of heat absorbed by the specimen. The nearly adiabatic conditions at 4 K lead to localized heating within the specimen from heat generated by moving dislocations. This localized heating leads to an imbalance between thermal and mechanical energy and to unstable plastic deformation in regions of higher local temperatures.[11]

From true stress-true strain diagrams for alloy 2090-T81, we calculate approximate strain-hardening rates ($\Delta\sigma/\Delta\epsilon$) of 2100 MPa at 4 K, 1500 MPa at 76 K, and 700 MPa at 295 K for a true strain of 0.05. These values are larger (about 50%) than those reported by Glazer, et al.[9] from data on an earlier vintage 2090-T81 at equivalent test temperatures and orientation (L). Our strain rate ($9 \times 10^{-5} \text{s}^{-1}$) was about an order of magnitude lower than that used by Glazer, et al. However, except at 4 K, this effect on strain-hardening rates is expected to be insignificant.

The strain-hardening rates for all alloys increase at lower temperature, but there is a stronger dependence on temperature of the strain-hardening rate of Al-Li alloys than of 2219. Glazer, et al.[9] report a decrease of planar slip at low temperatures for alloy 2090-T81. Since planar slip is more frequent in Al-Li alloys than in alloy 2219, strain-hardening may be associated with the frequency of planar slip: a decrease in the frequency of planar slip results in an increase of the strain-hardening rate. Other unique deformation mechanisms at low temperatures in Al-Li alloys have not been identified.

Analyses of the true stress-strain curves show that the strain-hardening rates at 4 K of 8090-T8771 are higher (~2800 MPa) and of WL049-T851 (1500 MPa) and WL049-T351 (1300 MPa) lower than the rate for alloy 2090-T81. Planar slip frequency has been associated with increased Li content. Since alloys 8090 and 2090 have higher Li contents than WL049, the association of planar slip with strain-hardening rates from these data at 4 K would portray an opposite trend to that discussed above on the basis of their temperature dependence. Therefore, it is likely that strain-hardening rates in Al-Li alloys must be related to dislocation-precipitate interactions, not planar deformation. The increased temperature dependence of the Al-Li alloys, compared to alloy 2219, provides evidence for this.

Planar slip has been associated with dislocation-precipitate interactions. The lack of correlation between planar-slip frequency and strain-hardening rates suggests that there is not a simple correlation between planar-slip frequency and precipitates. Clearly, for better fundamental understanding, these metallurgical variables should be sorted out.

6.2 Fracture Toughness

Two types of specimens and test techniques were used to evaluate the fracture toughness of Al-Li alloys at cryogenic temperatures. For T-L and L-T orientations C(T) specimens were machined from plates. For the S-L and S-T orientations, chevron-notched, short-bar specimens were machined in the through-thickness direction. The results of these measurements are discussed separately.

6.2.1 Compact-Tension Tests

Fracture toughness, measured using C(T) specimens, is plotted versus temperature in Figures 6.42-6.45 and listed in Table 6.1 for alloys 8090, 2090, WL049, and 2219 in various tempers.

Fracture toughness increases in all alloys and tempers at lower temperatures except for WL049-T351. This alloy is quite tough (-55 MPa$\cdot\sqrt{m}$) at room temperature and the fracture toughness decreases to about 30 MPa$\cdot\sqrt{m}$ at 4 K. Other alloys and tempers typically increase in toughness from 20-40 MPa$\cdot\sqrt{m}$ at room temperature to 30-50 MPa$\cdot\sqrt{m}$ at 4 K.

The toughness of alloy 2090 is strongly influenced by delamination effects from the flat, pancake-like grain structure. This is discussed more completely in the Fractography Section (6.3). The large scatter of toughness values of 2090-T81 (e.g., 26-74 MPa$\cdot\sqrt{m}$ at 76 K) of different crack orientations is likely to be caused by the influence of delaminations.

As measured by the J-integral test, alloys 8090 and 2090 in the T8 temper have higher toughness than alloys WL049 and 2219. Average values at 4 K for 8090 and 2090 range from 40 to 70 MPa$\cdot\sqrt{m}$; average values for WL049 and 2219 range from 25 to 45 MPa$\cdot\sqrt{m}$. The divergences in values at low temperatures of these two sets of alloys may be at least partially attributed to the effects of delaminations. However, another consideration is the cleanliness of the alloys. As described in Table 3.4, alloys 8090 and 2090 have considerably fewer secondary constituent particles ($3500/mm^2$ for 8090-T8771; $1700/mm^2$ for 2090-T81) than alloys WL049 and 2219 ($5300/mm^2$ for WL049-T851, lot 1; $6100/mm^2$ for 2219-T87). At low temperatures, shear-like failures are initiated by a microvoid coalescence type of ductile fracture. Larger particle density or size distribution would produce enhanced nucleation sites and, thus, result in lower toughness.

Therefore, there are two major distinctions between the tougher alloys, 8090 and 2090, and the alloys WL049 and 2219 at low temperatures: (1) the tendency to delaminate and (2) the constituent particle density. Both of these factors contribute to increased toughness of alloys 8090 and 2090 at low temperatures.

8090

Figure 6.42   Fracture toughness (J-integral, C(T) specimens)
versus temperature of various tempers and
orientations of Al-Li, alloy 8090.

2090

Figure 6.43 Fracture toughness (J-integral, C(T) specimens)
versus temperature of alloy 2090-T81 in two
thicknesses and orientations.
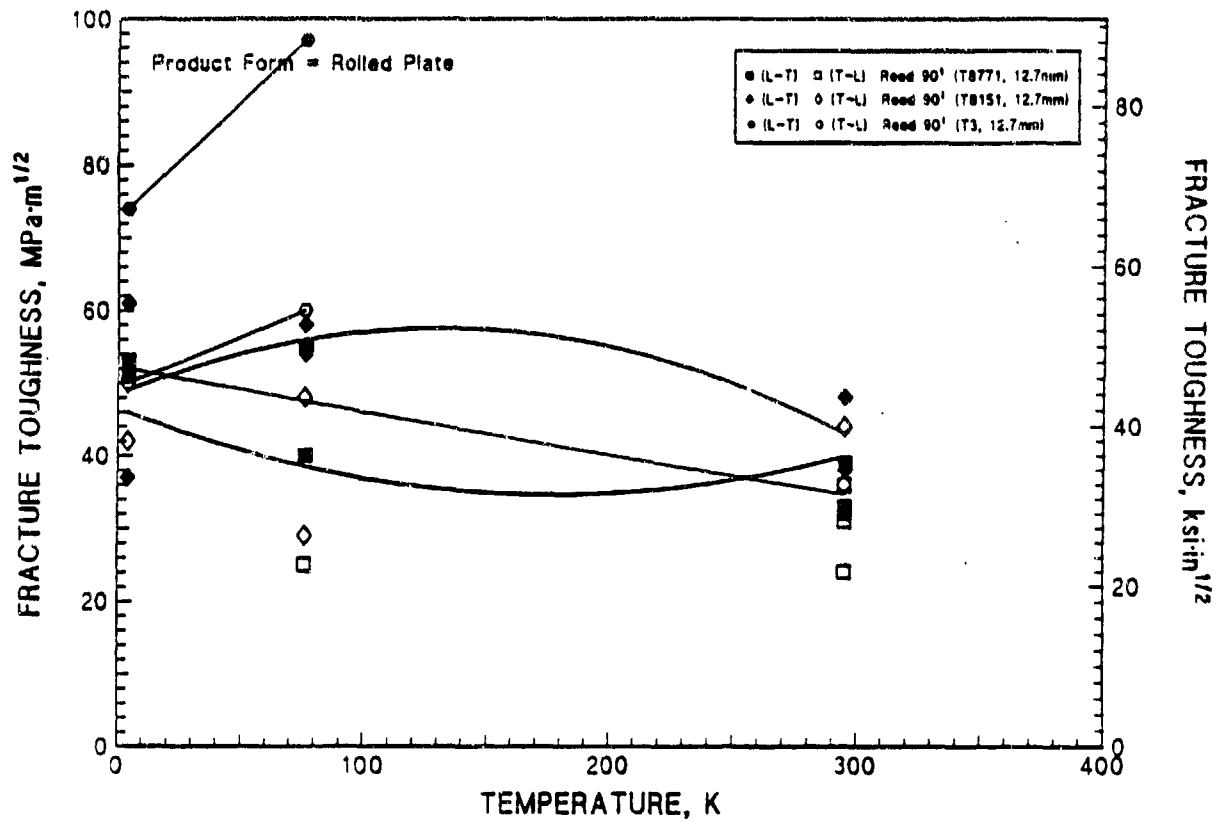
WL049

Figure 6.44 Fracture toughness (J-integral C(T) specimens)
versus temperature of various tempers and
orientations of Al-Li alloy WL049.

2219

Figure 6.45   Fracture toughness (J-integral, C(T) specimens)
versus temperature of various tempers and
orientations of alloy 2219.

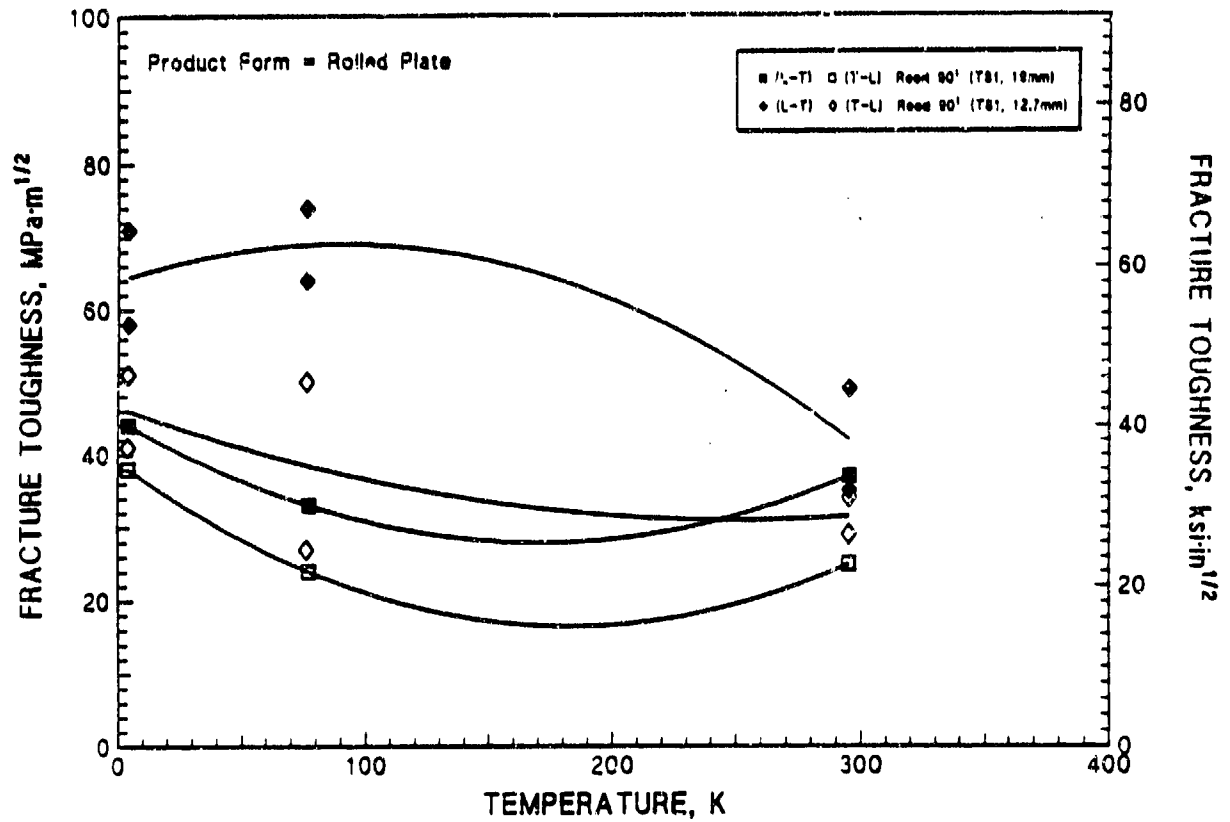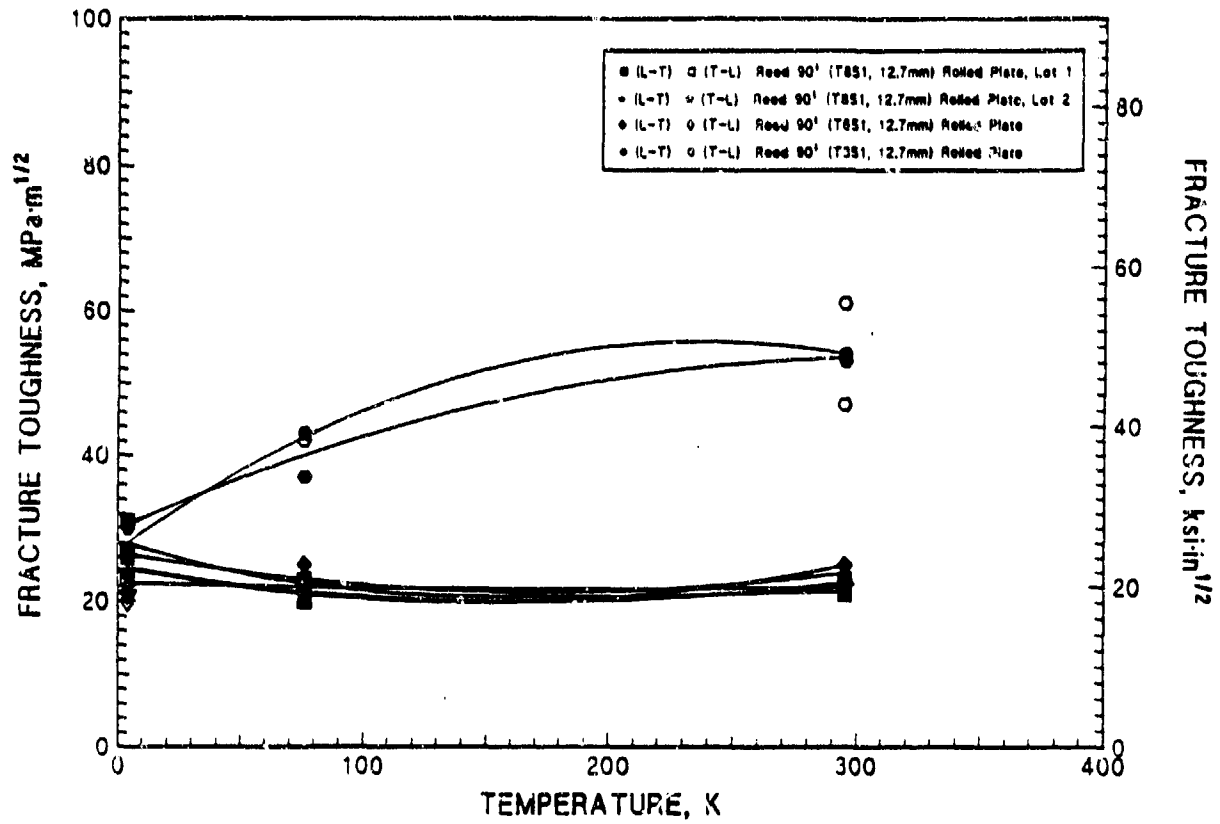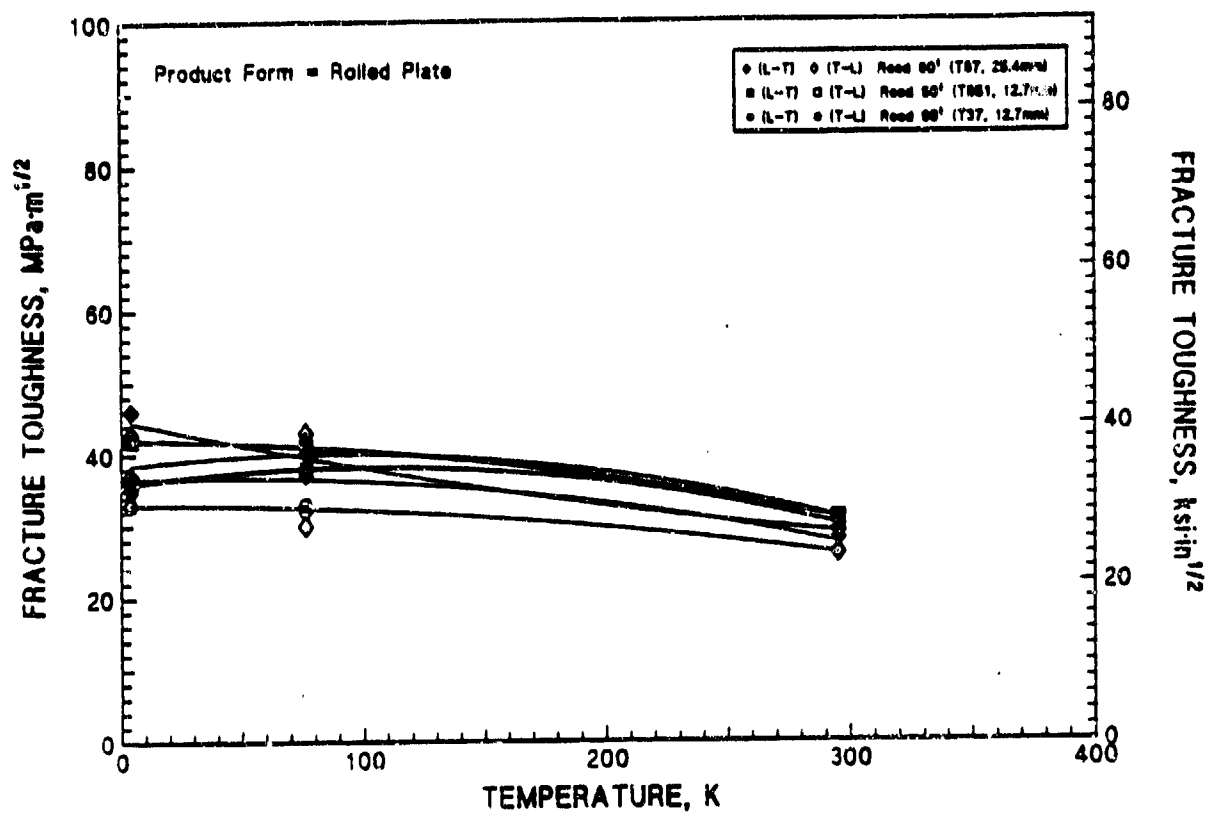## 6.2.2 Chevron-Notched Short-Bar Tests

Results of through-thickness, K_{Iv} measurements using the chevron-notched, short-bar specimen are plotted in Figure 6.46 for the S-L orientation and Figure 6.47 for the S-T orientation. The results are also contained in Table 6.1. The measurements are also discussed in another paper.[13]

The lowest toughness in these orientations is shown by 2090-T81, which has average values ranging from 8 to 13 MPa·$\sqrt{m}$. This very low toughness explains the ease of delamination in the rolling plane of other orientations of toughness and tensile tests. The highest toughness is exhibited by 2219-T851 at 4 K and by WL049-T351 at room temperature. The S-L and S-T toughness of the T8 temper alloys show little temperature dependence.

The through-thickness toughness in the S-L and S-T orientations are compared for 2090 and WL049 in Figure 6.48. The toughness of alloy 2090-T81 is clearly much lower. This lower toughness reflects a more-pronounced pancake-like grain structure. It is not clear why the toughness increases for the T851 temper of WL049 from 76 to 4 K. As indicated in Table 6.1, this increase at 4 K primarily reflects the contribution of the S-T orientation (31 MPa·$\sqrt{m}$ at 4 K, 18 MPa·$\sqrt{m}$ at 76 K). Other alloys do not show similar trends.

6.3 Fractography

In the course of the mechanical property studies, a limited number of photographs were taken of the Al-Li and 2219 tensile and fracture toughness specimens following failure. Both light microscopy and scanning election microscopy (SEM) were used. Many technical issues were not addressed in these limited studies; some of these will be studied in the future in association with technical papers and our continued program. Each alloy is discussed separately in this section.

Prior to this discussion, we point out the role played by intergranular delamination. In Figure 6.49, taken from Rao, Yu, and Ritchie,[14] the role of delaminations is schematically illustrated for each crack orientation. In our program, L-T, T-L, S-L and S-T orientations are included; therefore, we have no tests describing crack arrest effects. The delaminations are caused by the pancake-like grain structure of the Al-Li alloys. The effect of the delaminations in the crack divider and crack arrest orientations is to divert the crack and to reduce the thickness of the specimens that fracture in a shear mode. Crack diversion requires additional energy for crack redirection. Reduction in section thickness leads to plane stress conditions; failure under plane stress loading conditions results in higher toughness values. Thus, alloy 2090-T81 exhibits reduced toughness in the S-L and S-T orientations, but increased toughness in the L-T and T-L orientations. The increased toughness in the L-T and T-L orientations is caused by the increased ease of delaminations that serve to divide the crack.[14,15]

General fracture-surface topography observations, using light microscopy, are summarized in Tables 6.2 and 6.3 for tensile and fracture toughness, respectively.
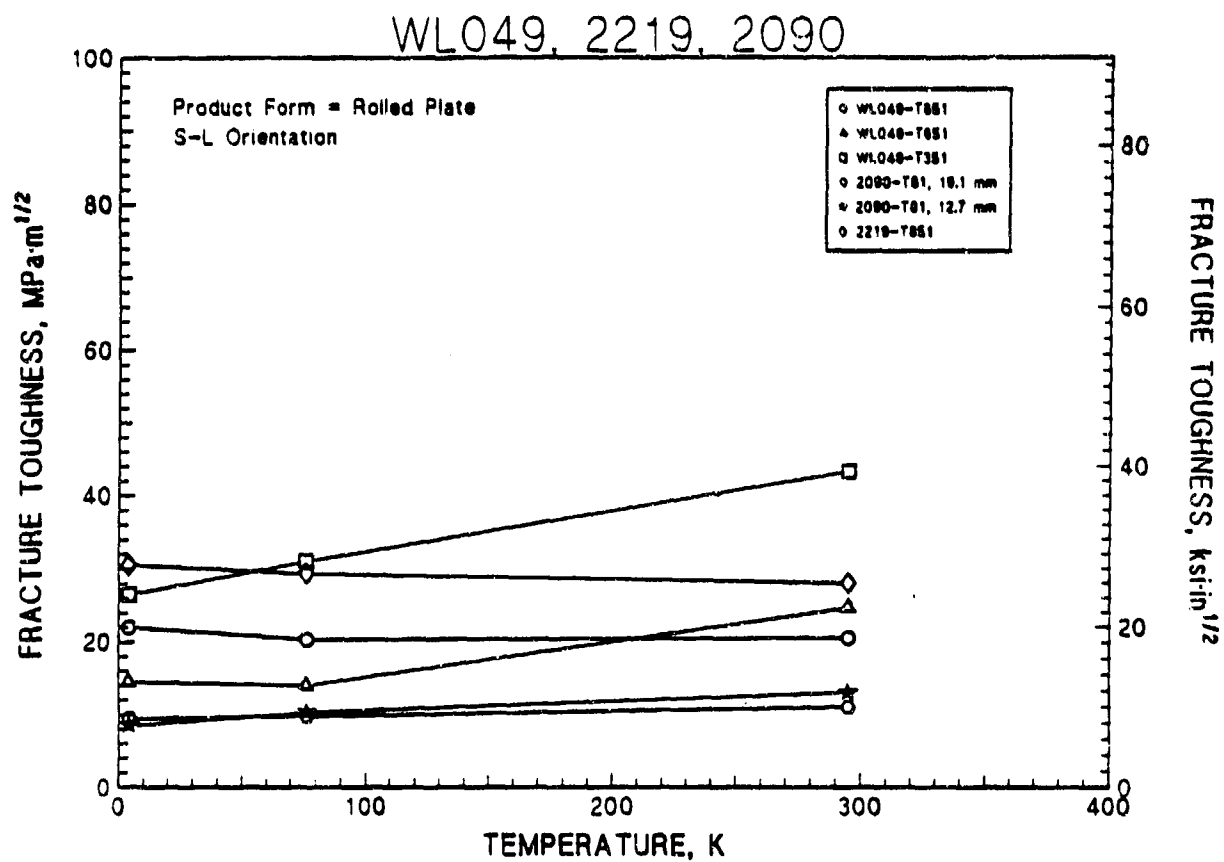
Figure 6.46   Fracture toughness (chevron-notched, short-bar)
versus temperature of S-L orientation of alloys
2090, WL049, and 2219 in various tempers.
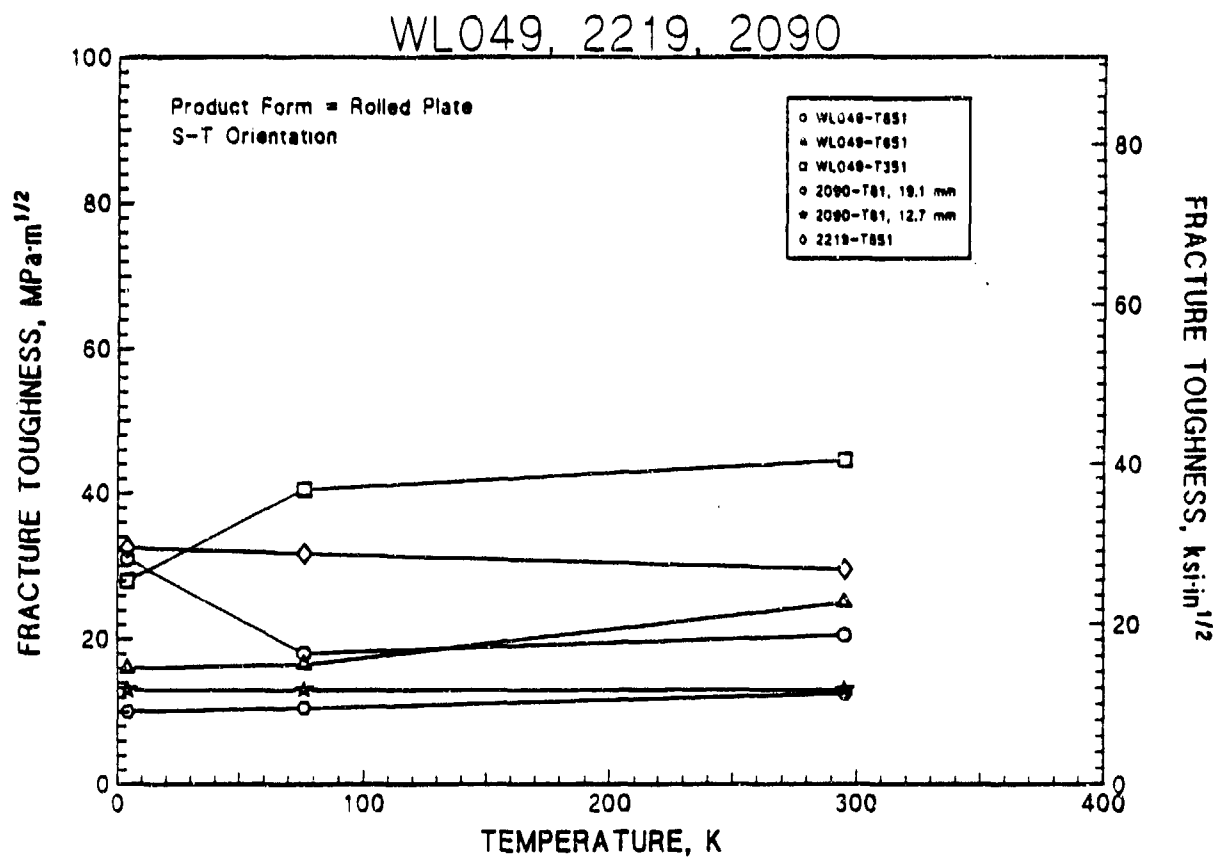
Figure 6.47   Fracture toughness (chevron-notched, short-bar)
versus temperature of S-T orientation of alloys
2090, WL049, and 2219 in various tempers.
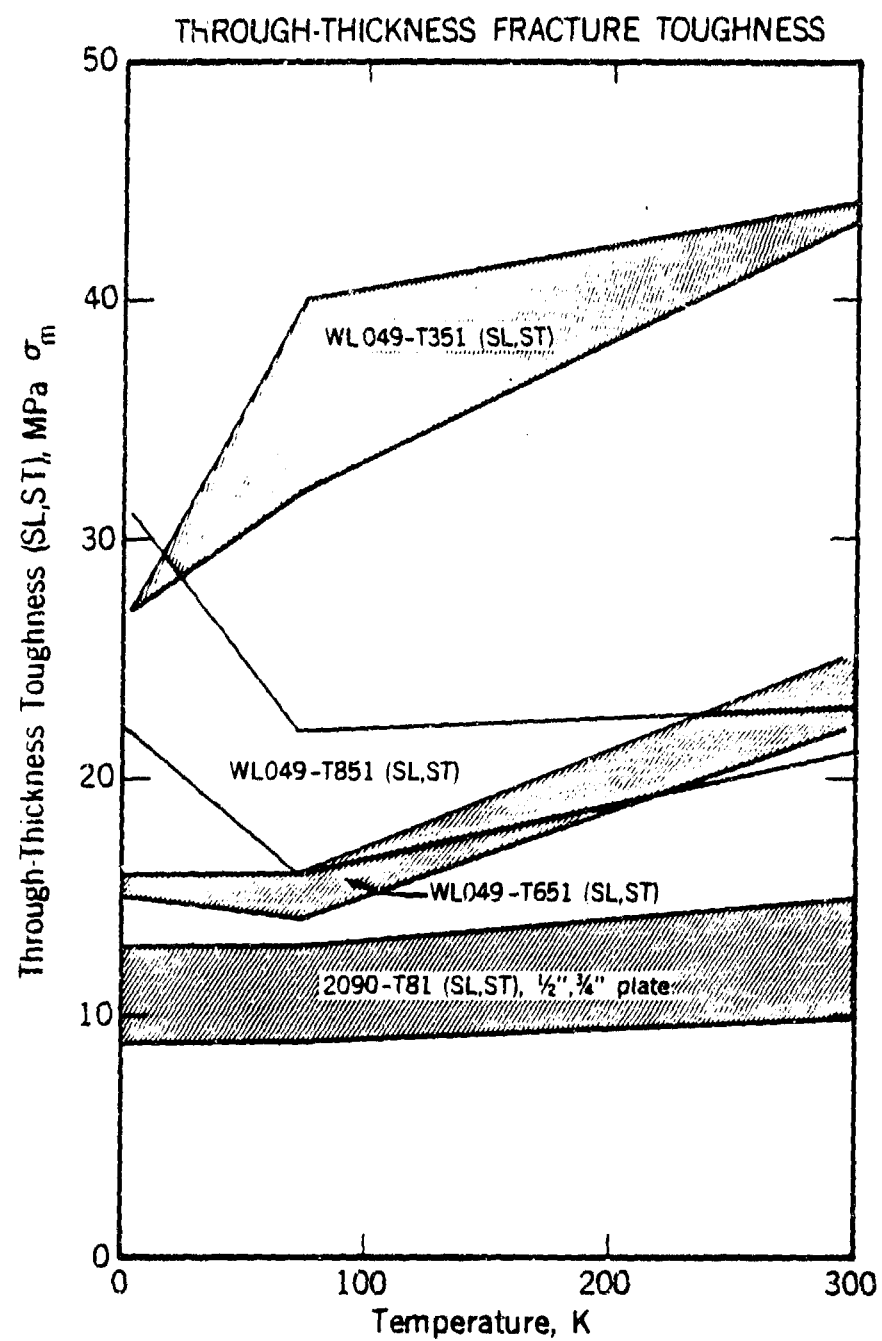
Figure 6.48   Comparison of 2090 and WL049 through—thickness
toughness as a function of temperature.
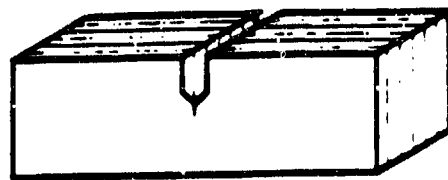
Crack
divider
(L-T,T-L)
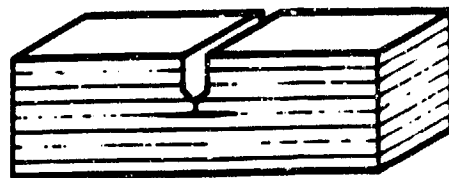
Crack
arrester
(T-S,L-S)

Crack
delamination
(S-L,S-T)

Figure 6.49   Schematic illustrating terminology and relationship
for each specimen orientation with plane of delamination
(from Rao, Yu, and Ritchie[14]).

95

Table 6.2 Failure–Mode Observations from Tensile Specimens.

Test Temperature

Material	295 K		76 K		20 K		4 K	
	T	L	T	L	T	L	T	L
2219–T37	S	S	d	M	M+d	M	M+d	M+S
2219–T851	M+S	M	M+S	M	S	M+S	M+S	S+M
2090–1/2"	d	d	d	d	d	d+S	d	d
2090–3/4"	D	d	d	D	d	D	d	D
WLD049–T3	S+d	S	d	S+d	d	S	d	S+d
WLD049–T6	S+d	S	d	d	d	d	d	d
WLD049–T8	d	S	d	S+d	d	S+d	d	S+d
8090–T3	S	S	d+S	S+d	d+S	S+d	d+S	S+d
8090–T8771	S+d	S	d	S	d	S+d	d	S
8090–T8151	d+S	S	S+d	D+S	S+d	S	S+d	S+d

M – microvoid coalescence, planar fracture
S – microvoid coalescence, shear fracture
d – intergranular, small delaminations
D – intergranular, big delaminations

96

Table 6.3 Failure-Mode Observations from C(T) Specimens.

	Test Temperature					
	295 K		76 K		4 K	
Material	T-L	L-T	T-L	L-T	T-L	L-T
2219-T37	M+d	M	M	M	M	M
2219-T8	M	M	M	M	M	M
2090-1/2 "	D	D	D	D	D	D
2090-3/4"	d	d	d	d	d	d
WLD049-T3	d+M	M	d	d+M	d	d
WLD049-T6	----	M+d	d	d	d	d
WLD049-T8	M+d	M	d	d	d	d
8090-T3	----	----	d	D	d	d
8090-T8771	D	D	d	d	--	d
8090-T8151	----	D	d	D	d	d

M - microvoid coalescence
d - small delamination
D - big delamination

6.3.1 Alloy 8090-T8771

Tensile fracture surfaces of T and L orientations from tests at 295, 76, and 4 K for 8090-T8771 are shown in Figure 6.50. The macroscopic failure mode is primarily shear. At low temperatures, specimens of the T orientation exhibit failures that are normal to the tensile axis, but examination of their fracture profiles (Figures 6.51 and 6.52) indicates the predominant presence of transgranular shear. In these specimens, the transgranular shear is interrupted periodically by intergranular delaminations (Figures 6.51 and 6.52). The L orientation specimen failures were always slanted (in profile), indicating a macroscopic shear mode. At the microscopic level, microvoid coalescence is their expected failure mode.

The fracture surfaces of 8090-T8771 CT fracture-toughness specimen are shown in Figure 6.53. At all temperatures (295, 76, 4 K) there is evidence of crack dividing from intergranular delaminations. On the surfaces of the specimens tested at 76 and 4 K, both precracking, R-curve, and final loading regions are clearly visible.

6.3.2 Alloy 2090-T81

Macrophotographs of 2090-T8 tensile specimens are shown in Figures 6.54 and 6.55. Profiles of the tensile fractures are included in Figure 6.56. The ductility of specimens in the T orientation is low, although failures at all temperatures are shear-like. In the T orientation, intergranular delaminations are present (see Figure 6.56) but do not act effectively as crack dividers. In contrast, there are extensive intergranular delaminations at low temperatures in tensile specimens oriented in the L direction. This indicates that the S-L fracture toughness must be lower than the S-T fracture toughness; this is borne out by the chevron-notched, short-bar data contained in Table 6.1 In specimens of L orientation, the very large delaminations divide the crack. The macroscopically visible delaminations are much more apparent in specimens from the 19 mm (0.75 in) thick plate, compared to the 12.7 mm (0.50 in) plate (see Figures 6.55 and 6.56). Specimens of L orientation from the 12.7 mm (0.50 in) thick plate delaminate more frequently than the T oriented specimens at low temperatures, but these delaminations are much smaller and do not serve to divide the crack. Therefore, in the 12.7 mm (0.50 in) plate, interpretation of the much larger ductility of the L oriented specimens must not be confined to delamination effects.

Figures 6.57 and 6.58 illustrate that tensile failure at low temperatures in 2090-T81 is composed of two primary microscopic modes: intergranular fracture and microvoid coalescence. Alternate zones of each type of failure mechanism are observed, using SEM, on the fracture surfaces. Referral to the fracture profiles of Figure 6.56, especially the T oriented specimens, indicates that the crack path frequently followed vertical paths (axial to the tensile direction). These vertical paths are grain boundaries.
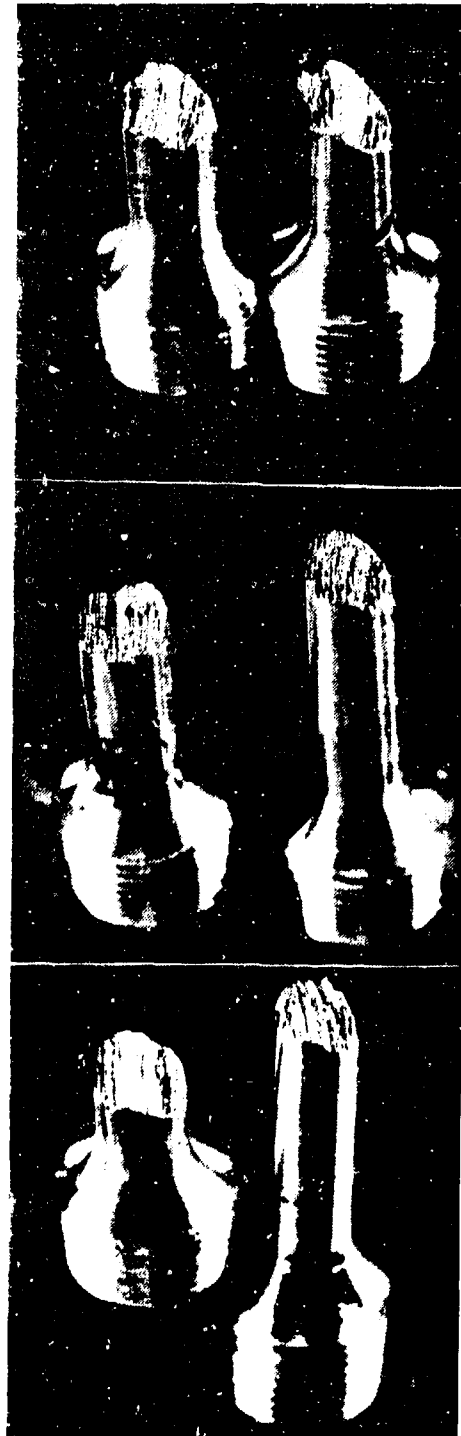
Figure 6.50   Fracture surfaces of 8090–T8771 tensile specimens,
T and L orientations, at 295, 76, and 4 K.

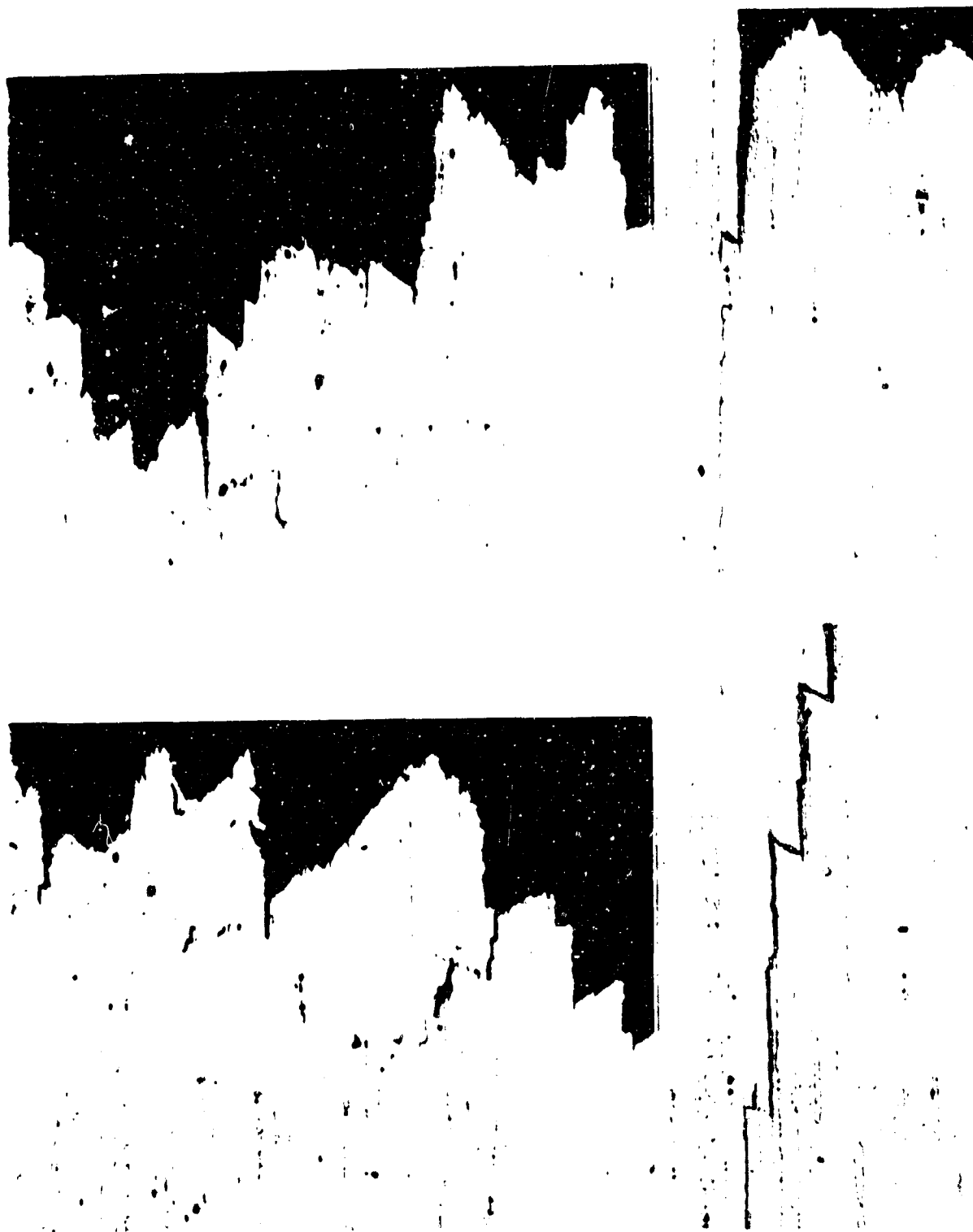Figure 6.51   Tensile fracture profiles of 8090–T8771 specimens at
4 K (50X–top, 200X–bottom).
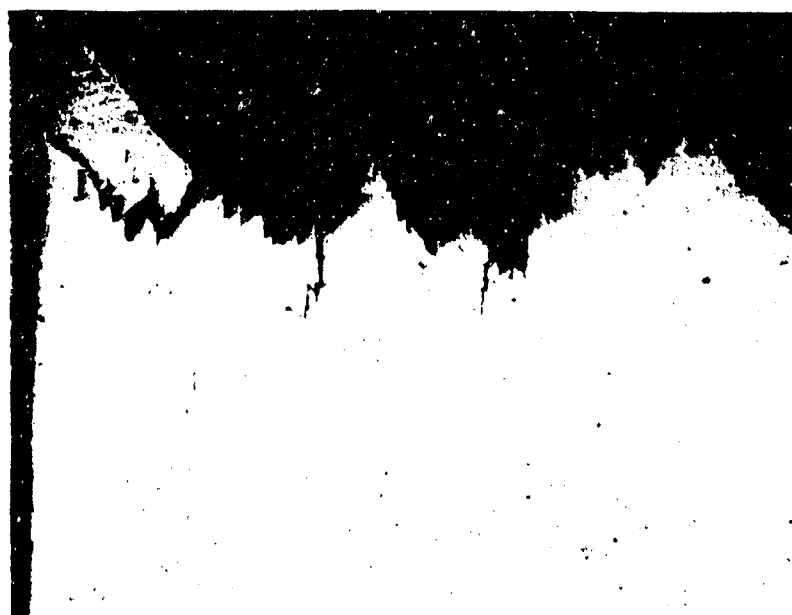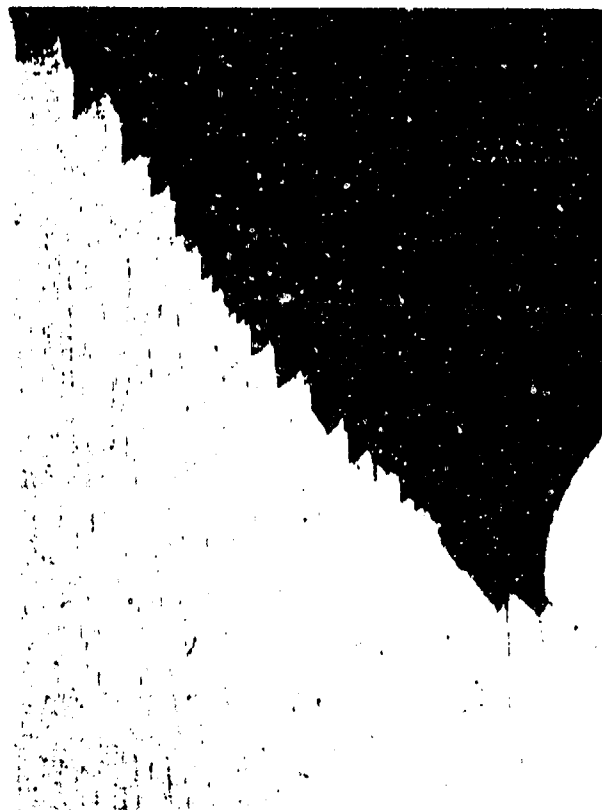
Figure 6.52   Tensile fracture profiles of 8090–T8771 specimens at
20 K (20X; L orientation–top; T orientation–bottom).
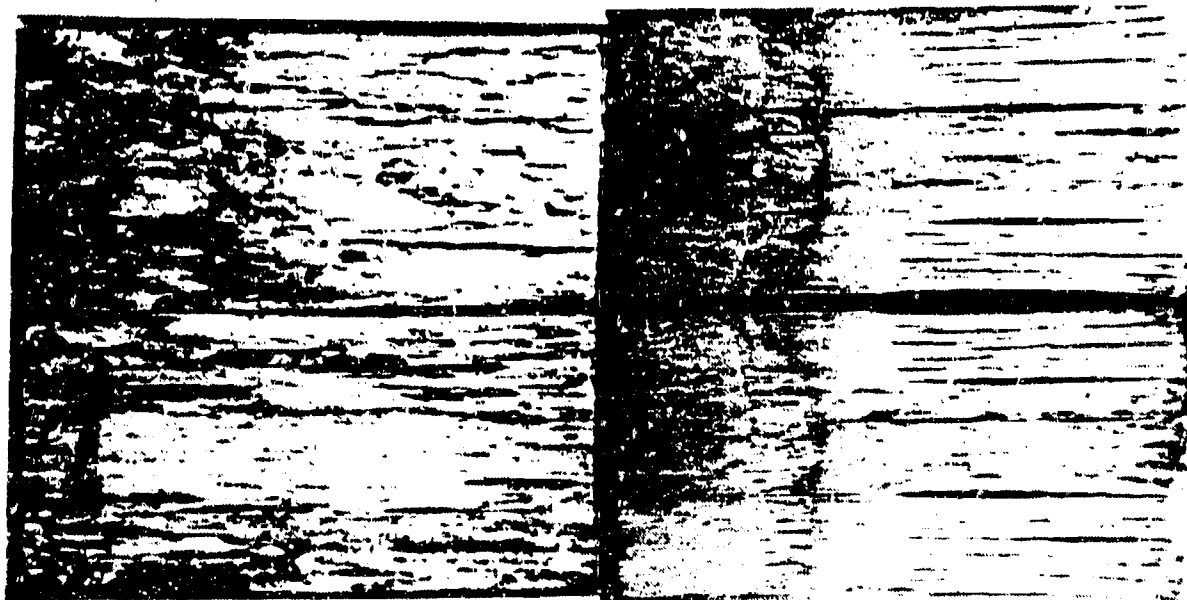
Figure 6.53   Fracture surfaces of C(T) fracture toughness specimens of 8090-T8771 (1.2X).
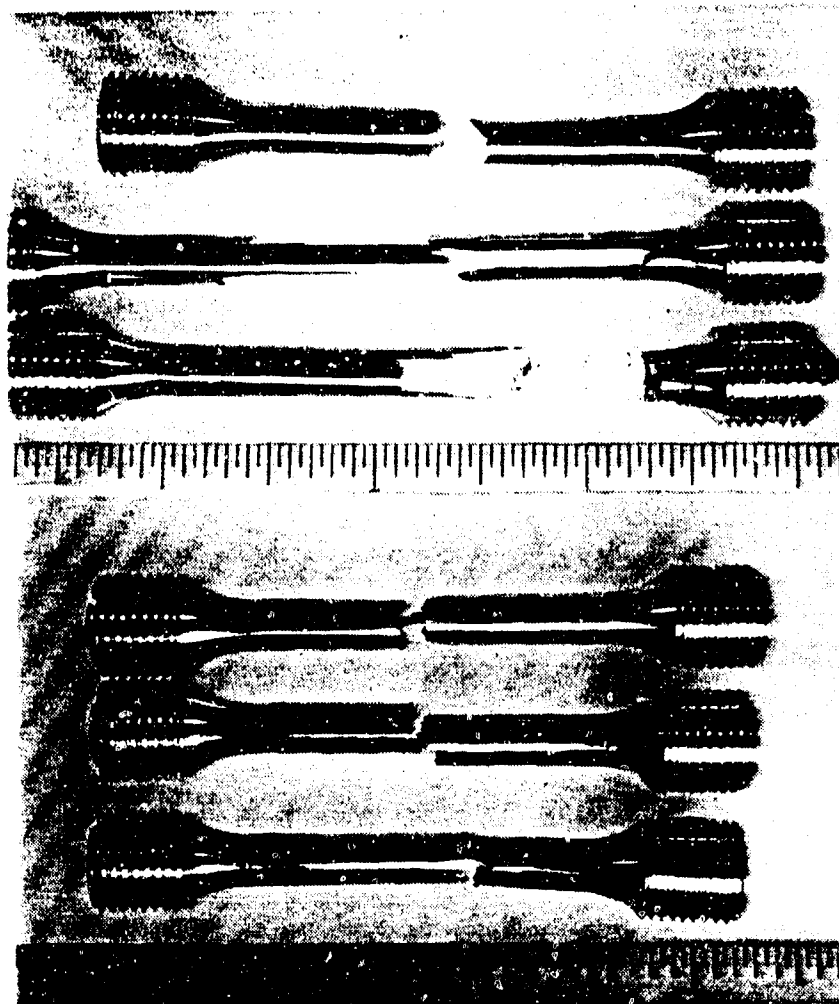
Figure 6.54   Tensile specimens of 2090-T81 (19 mm plate) in T and L
orientations, tested at 295, 76, and 4 K.

103

Figure 6.55(a)   Tensile specimens of 2090–T81 in T and L
                  orientations, tested at 295, 76, and 4 K.
                  From 12.7 mm plate.
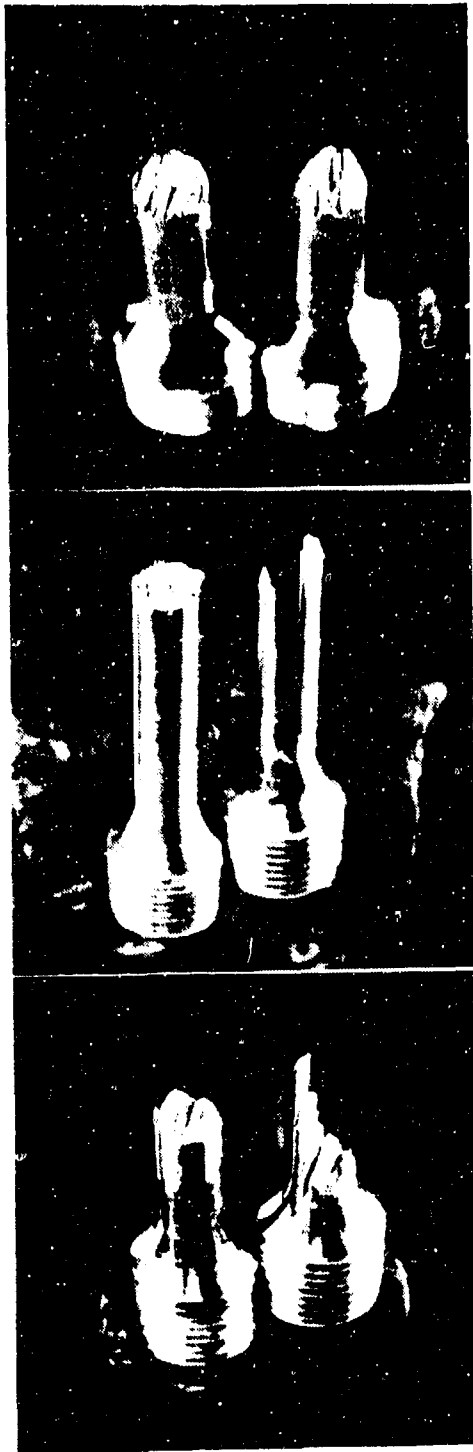
Figure 6.55(b)   From 19 mm plate.

Figure 6.56(a) Profiles of tensile specimens of 2090–T81 in T and
L orientations, tested at 295, 76, and 4 K.
From 12.7 mm plate.

Figure 6.56(b)   From 19 mm plate.

Figure 6.57   SEM photographs of fracture surface of 2090–T81
               (12.7 mm plate) tensile specimens, tested at 76 K.

108

Figure 6.58   SEM photographs of fracture surface of 2090–T81
(12.7 mm plate) tensile specimens, tested at 76 K.

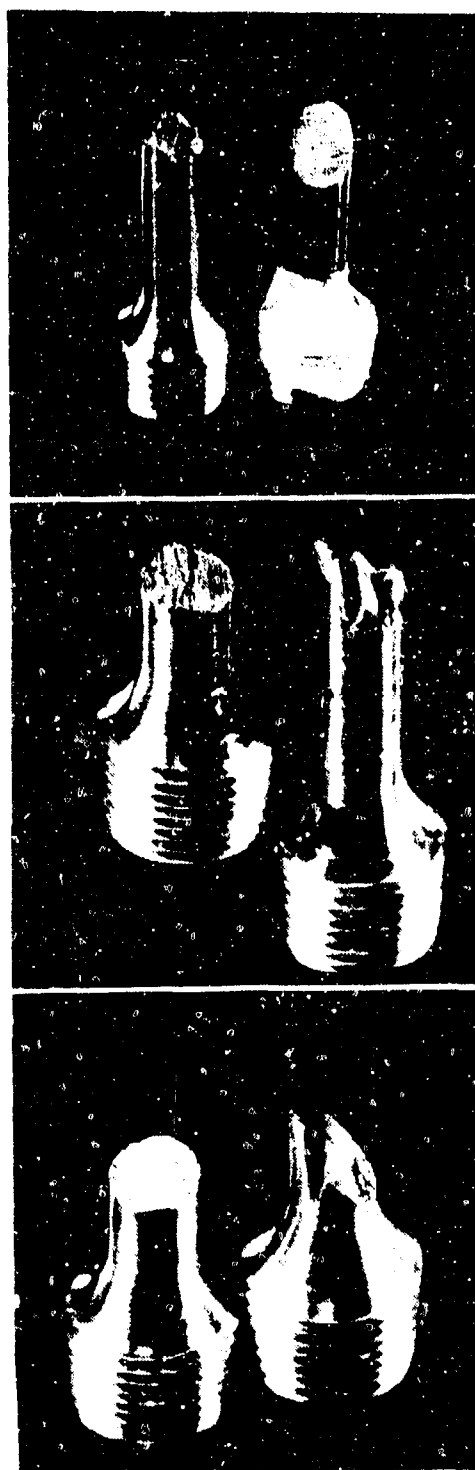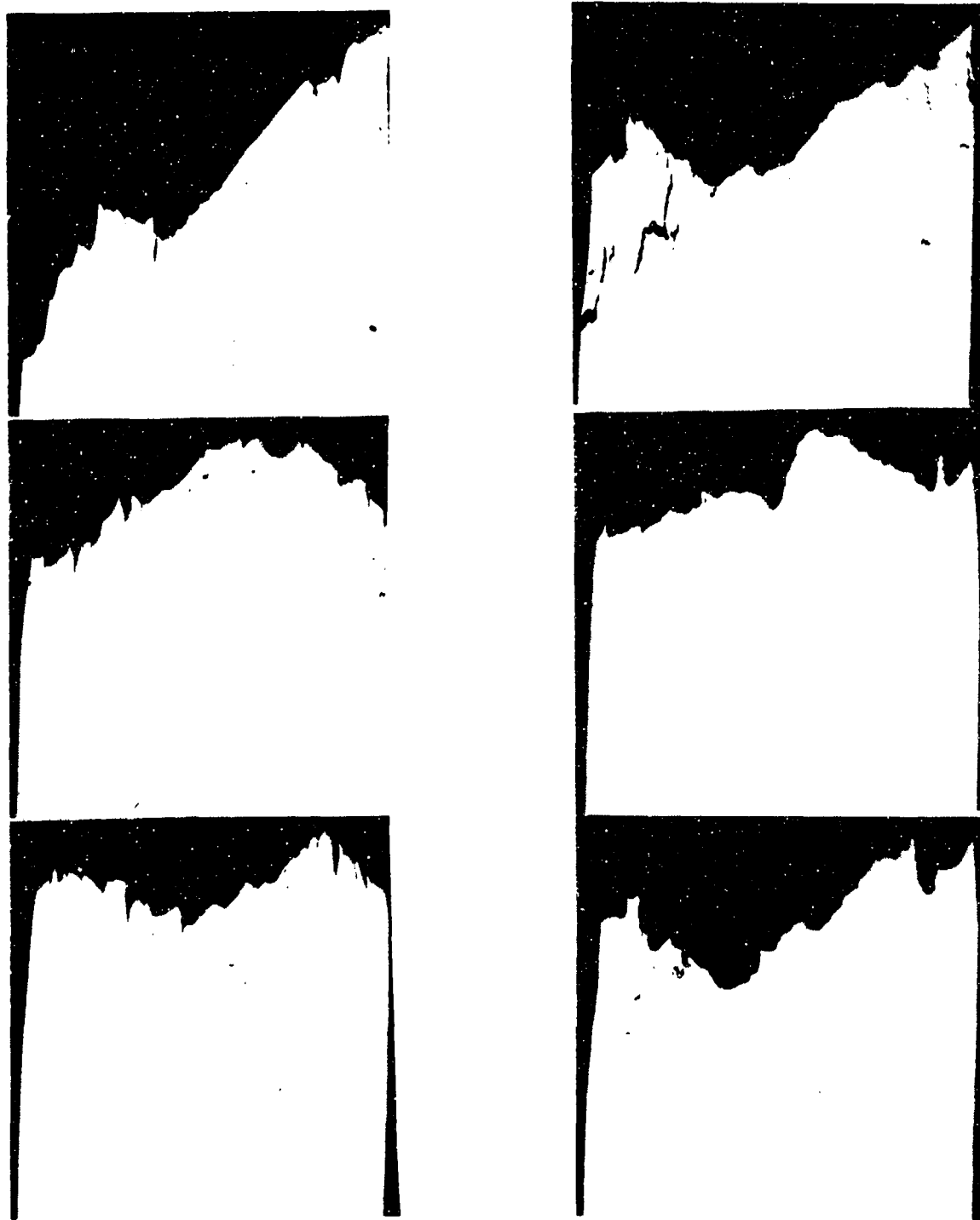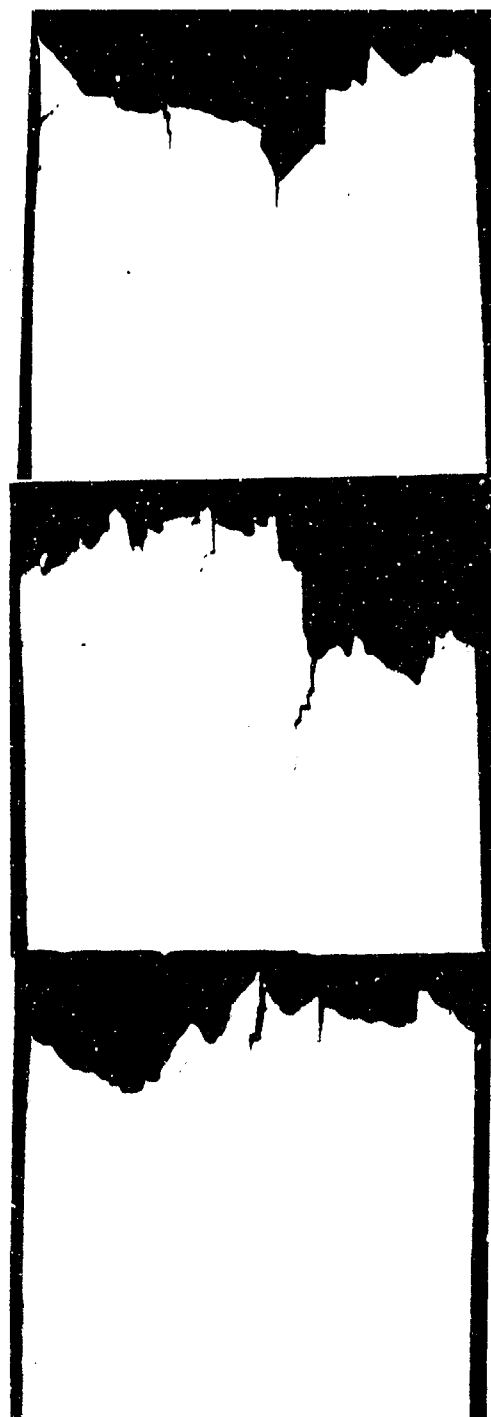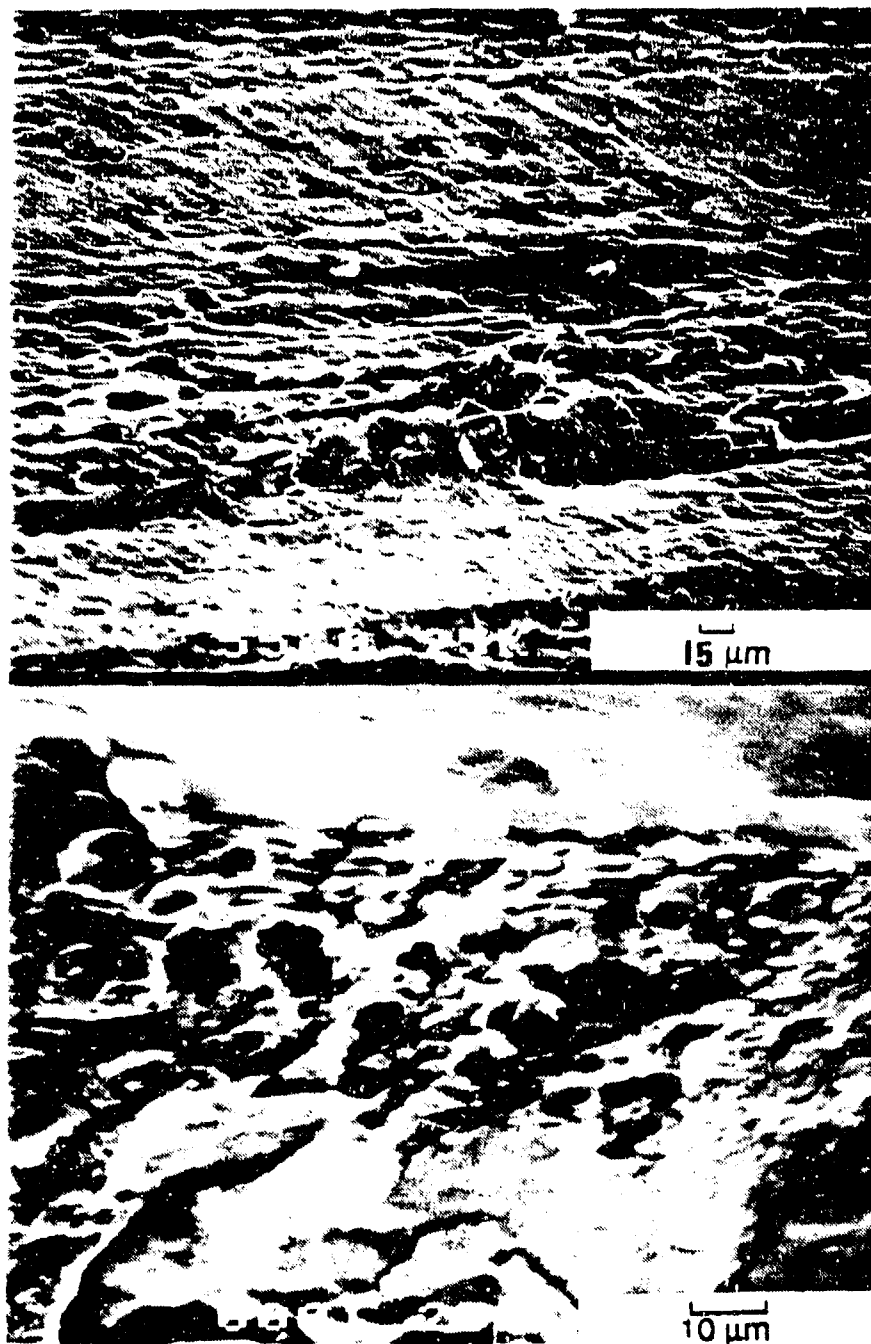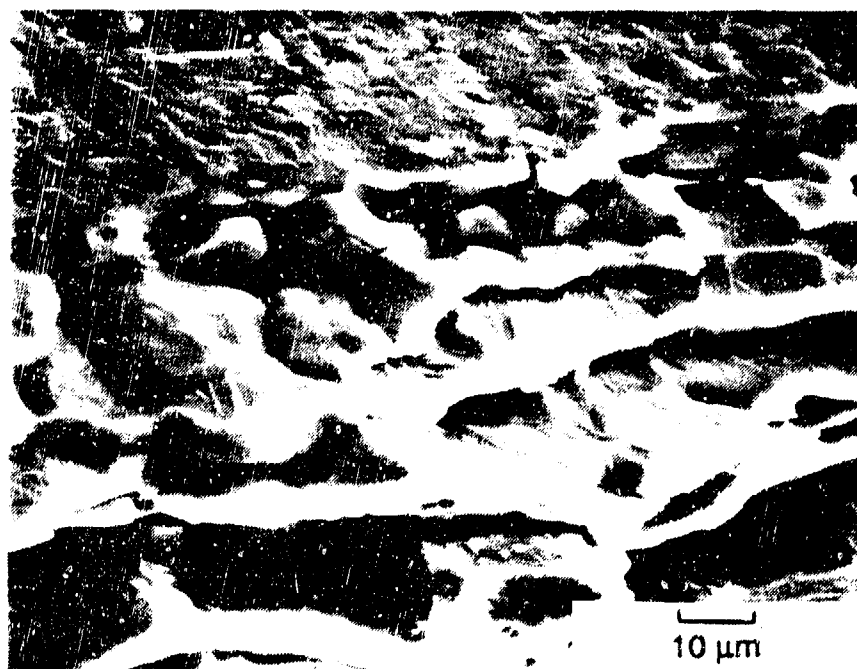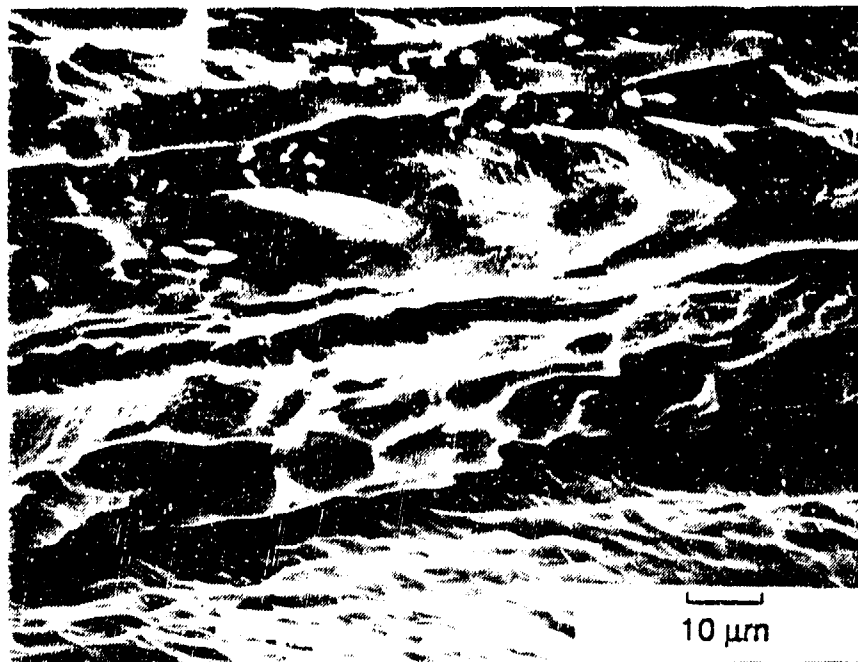In Figures 6.57 and 6.58, the small (2-3 μm) particles on the fracture surface are thought to be secondary constituent particles, aligned on grain boundaries. Delaminations in C(T) fracture toughness specimens from 19 mm (0.75 in) thick plate are more frequent than in specimens from 12.7 mm (0.50 in) plate, as illustrated in Figure 6.59 for 4 K tests. This reflects the smaller grain size in the thicker plate. However, within the considerable scatter of data for the T-L orientation, the increased frequency (or reduced grain size) has no effect on the fracture toughness. In fact, in the L-T orientation the fracture toughness is noticeably higher in the specimens that have larger grain sizes (thinner plate).

Fracture profiles in C(T) specimens are shown in Figure 6.60. In these specimens, the delamination depths are large. This ensures the diversion of cracks from their normal transgranular failure mechanism.

Fracture surfaces of T-L oriented, C(T) toughness specimens are shown in Figure 6.61. The transgranular shear failure mechanism is initiated by very small, microvoid sites that form on secondary constituent particles. The coalescence of the microvoids is relatively planar, probably reflecting the tendency toward shear deformation.

Chevron-notched specimens (S-L orientation) of 2090-T81 are very brittle at low temperatures and the fracture surface, illustrated in Figure 6.62, reflects this. Planar, cleavage-like surfaces are apparent; these surfaces likely represent grain boundaries. Grain boundaries in these orientations are very nearly planar. The small grain-like appearance visible on the fracture surface probably represents subgrain structure.

Striking photographs of the fracture surface of S-T oriented, chevron-notched, short-bar specimens of 2090-T81 from 12.7 mm (0.50 in) plate are shown in Figure 6.63. In the top photograph, the spherical-shaped upheavals are probably small recrystallized grains. In the lower photograph the rod-like, oriented shapes of the T_1 precipitates are visible on the fracture surface. The lower photograph was taken from the planar region shown in the upper photograph.

6.3.3 Alloy WL049-T851

Fracture profiles of WL049-T851 C(T) specimens, tested at 4 and 295 K are shown in Figure 6.64. No delaminations were observed at room temperature. Delaminations at low temperatures followed grain boundaries. There is evidence for larger dimples in the profile of the specimen tested at 295 K.

Fracture surfaces for T851 temper C(T) specimens tested at 4 and 295 K are compared in Figures 6.65 and 6.66. Comparison of these figures supports the conclusion from the profile examination that delaminations occur only at low temperatures. However, perusal of the higher magnification SEM pictures strongly suggests identical fracture micromechanisms at both 4 and 295 K: limited microvoid coalescence, infrequent small cracks normal to the fracture surface (intergranular cracking), and brittle failure of constituent particles or inclusions. The fracture surfaces are almost identical and both have many secondary constituent particles.

110

Figure 6.59(a)   Fracture surface of 2090–T81, C(T) fracture
                   toughness specimens, in T–L orientation that
                   were tested at 4 K.   From 12.7 mm plate,
                   top–30X, bottom–200X.

111
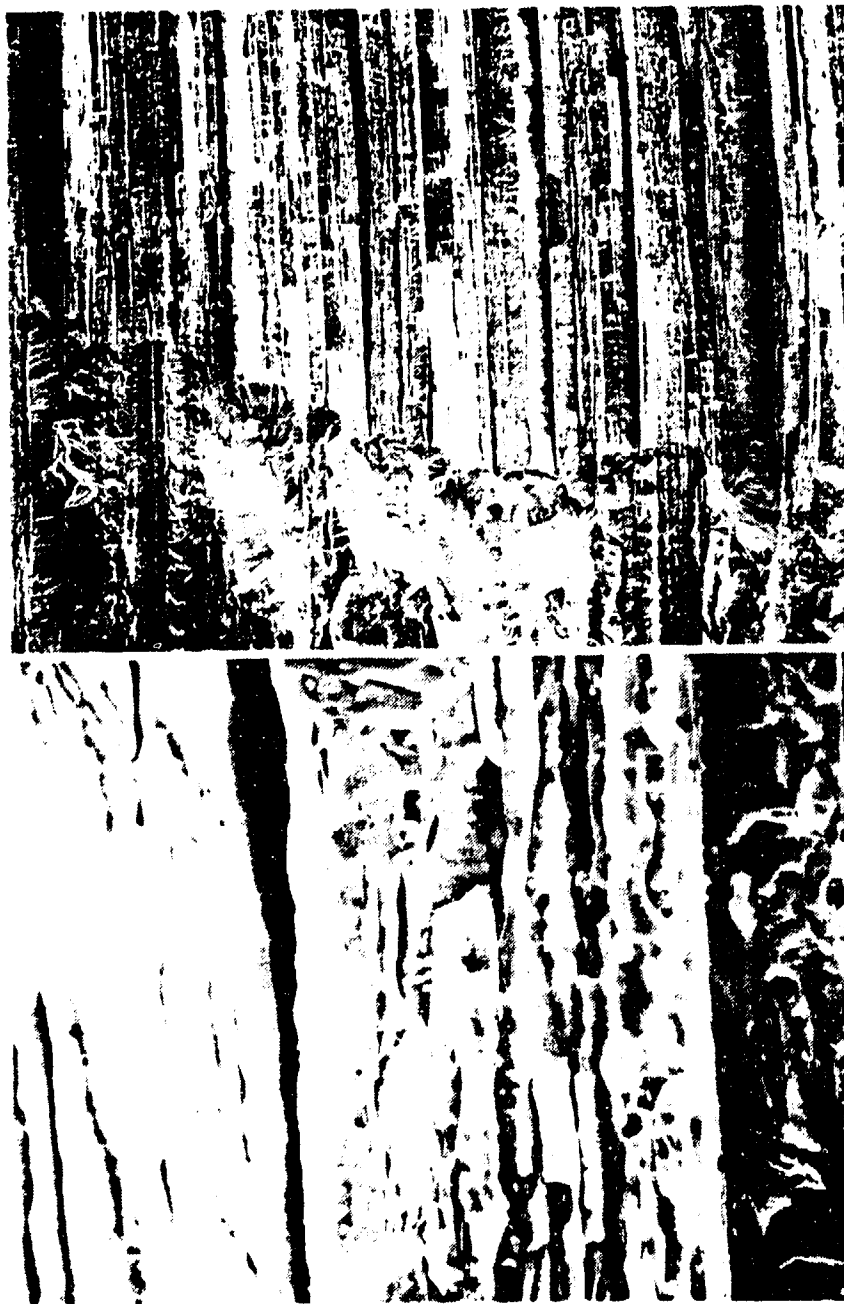
Figure 6.59(b)   From 19 mm plate, top-20X, bottom-500X.

112

Figure 6.60   Profile of C(T) specimen, alloy 2090–T81,
L–T orientation, 76 K, 50X.

Figure 6.61(a)   Fracture surface of 2090–T81, 12.7 mm plate,
T–L orientation, tested at 4 K.   250X.

114
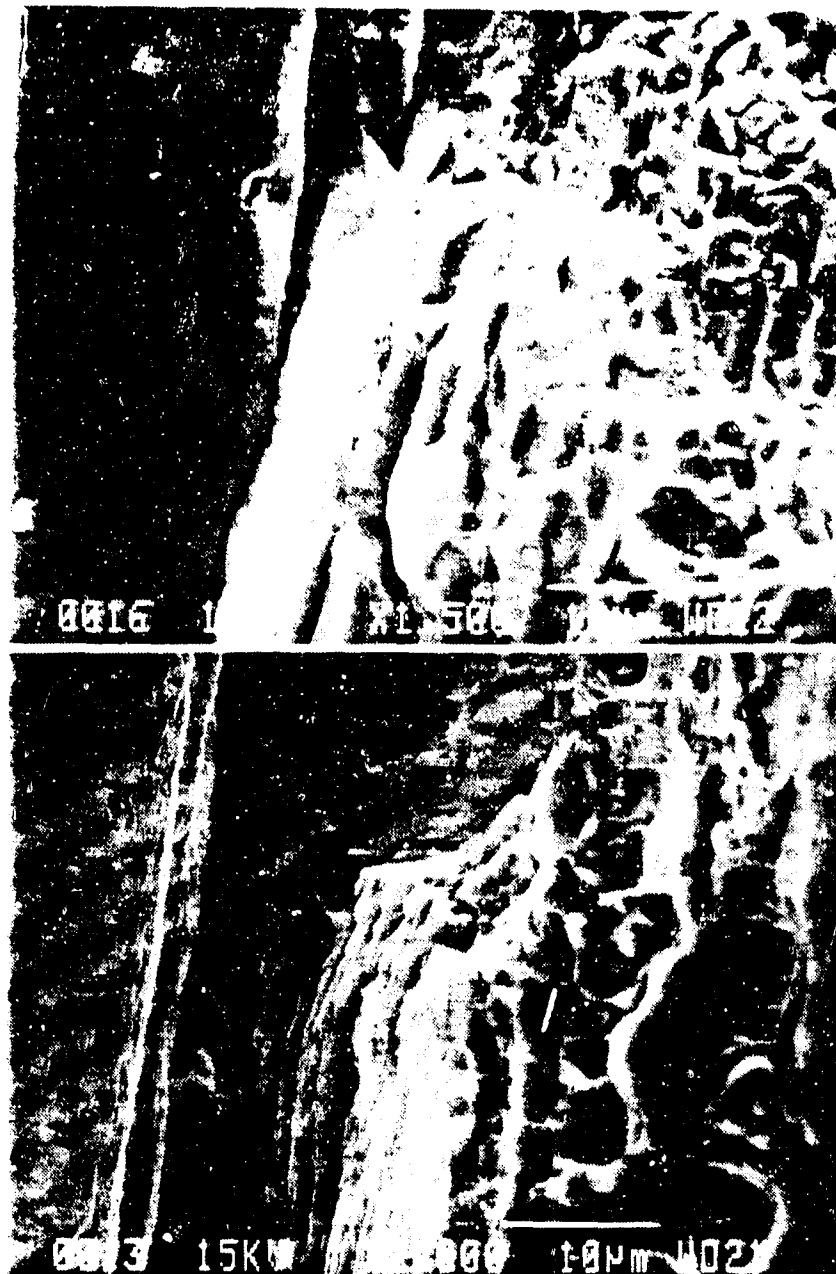
Figure 6.61(b)   Top—1500X, bottom—2000X.
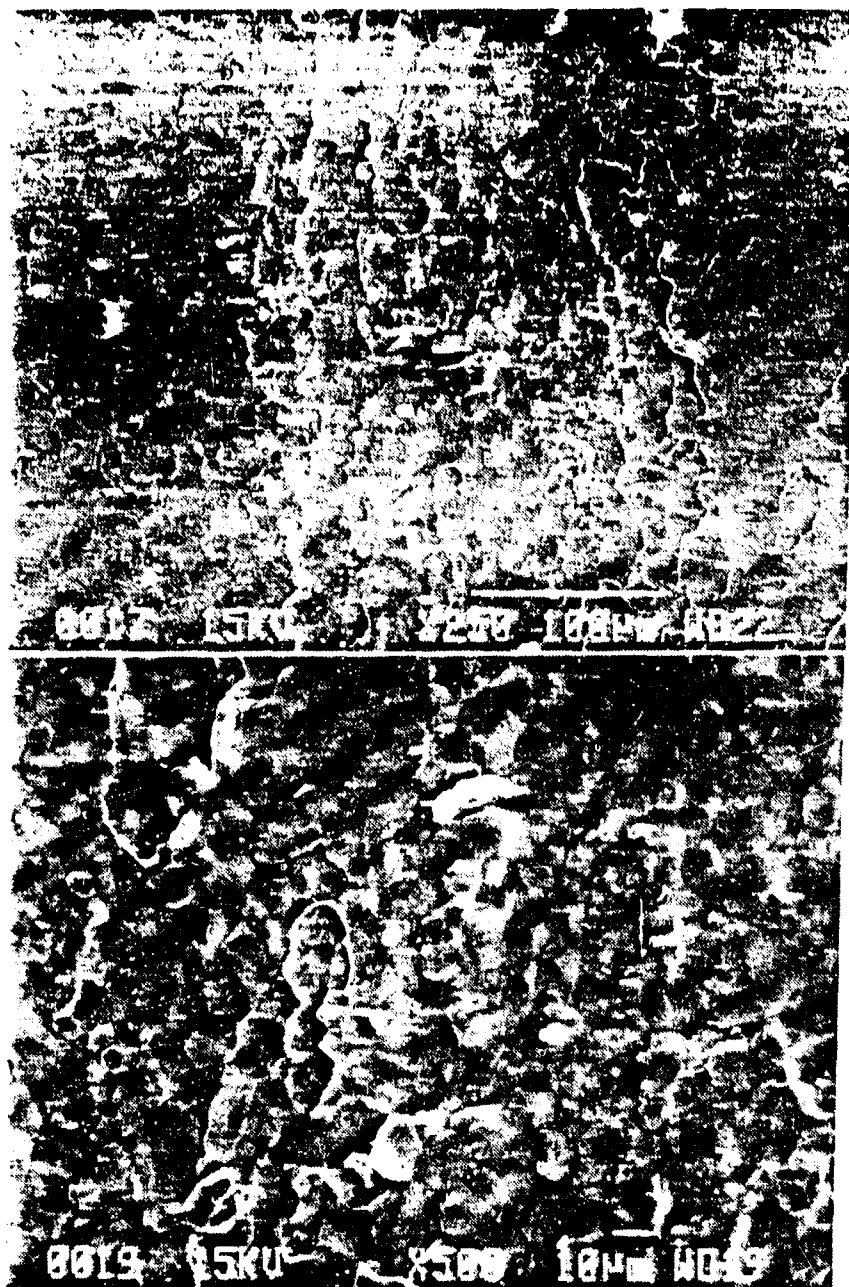
Figure 6.62(a)   Fracture surface, S–L orientation at 4 K of 2090–T81
chevron–notched, short–bar specimens from 12.7 mm
plate. Top–250X, bottom–500X.
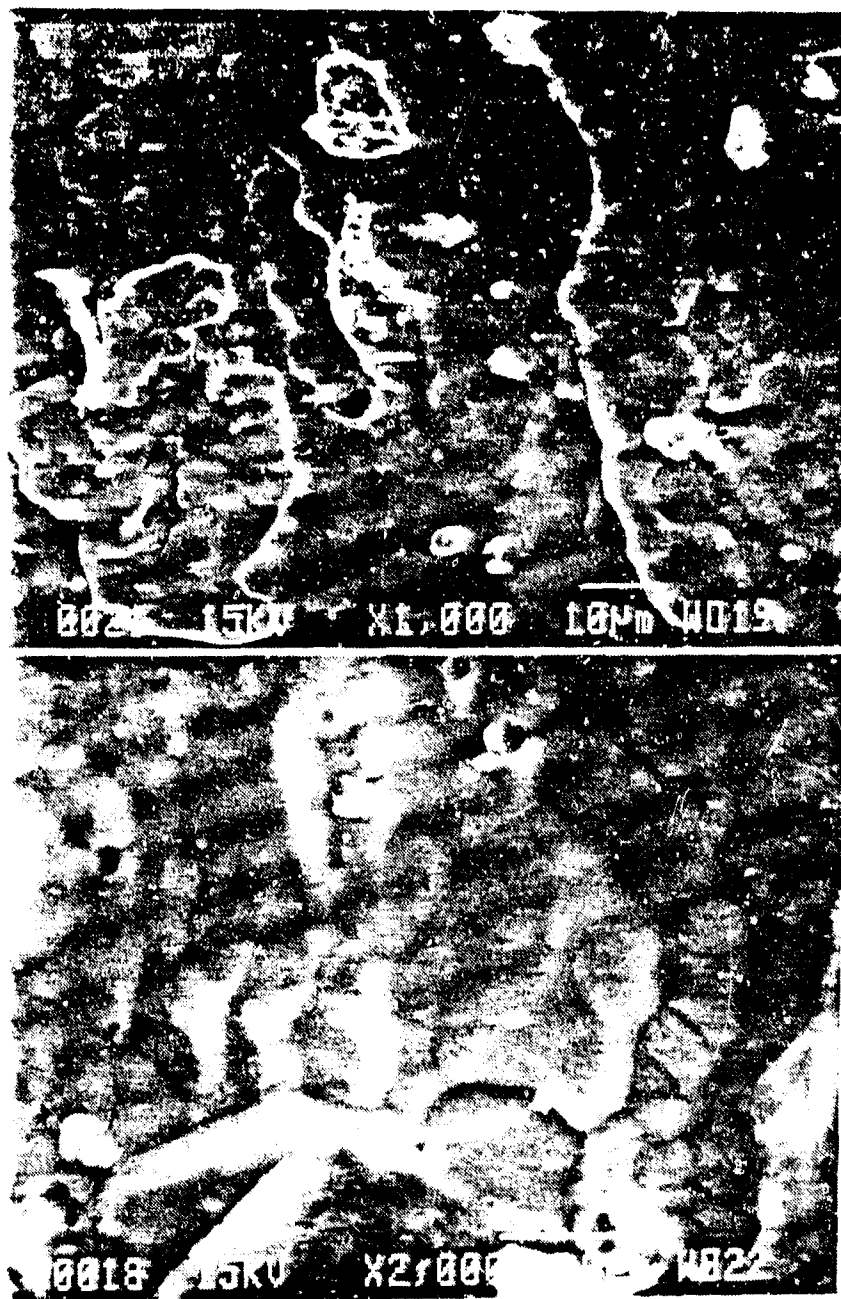
Figure 6.62(b)   Top-100OX, bottom-2000X.

117

Figure 6.63   Fracture surface, S-T orientation at 4 K, of
2090-T81 chevron-notched, short-bar specimens
from 12.7 mm plate. (a) top-1000X; (b) 3000X.

Figure 6.64   Fracture profile, T-L orientation of WL049-T851, of
               C(T) toughness specimens. (a) top left-50X, top
               right-500X at 4 K; (b) bottom left-500X at 4 K;
               (c) bottom right-500X at 295 K.

Figure 6.65   Fracture surfaces, T-L orientation of WL049-T851, of C(T) toughness specimens. (a) top-30X at 295 K; (b) bottom-30X at 4 K.

Figure 6.66   Fracture surfaces, T-L orientation of WL049-T851, of C(T) toughness specimens.   (a) top-500X at 295 K; (b) bottom-500X at 4 K.

Figure 6.67 confirms our earlier discussion of the fracture micromechanisms in WL049-T851. Microvoid coalescence is evident at all magnifications. Cracking normal to the fracture surface is evident in Figure 6.67 (a, top) and (b, top). Brittle constituent particles are very much in evidence in Figure 6.67(b).

The fracture surface of a chevron-notched, short-bar specimen, tested in the S-L orientation at 4 K, is shown in Figure 6.68. The surface appears similar to the 2090 specimen surface (Figure 6.62) as infrequent ridges are apparent in Figure 6.68. Extensive, small, constituent particles are shown on the fracture surface in Figure 6.68 (b, bottom).

6.3.4 Alloy 2219-T37

Alloy 2219-T37 has good toughness (51-57 MPa·√m) in the T-L orientation at 4 K and the fracture surface (Figure 6.69) shows that the primary micromechanism is microvoid coalescence. In the higher-magnification SEM picture (Figure 6.69) a high density of constituent particles are present, but no delaminations are observable.

The presence of many constituent particles and the evidence for the fibrous nature of the fracture surface are related. The ductile nature of the T37 temper, even at 4 K, permits a larger plastic zone, and therefore samples particles over a larger width along the crack path. The more jagged crack path and the appearance of an apparently larger density of particles are evidence that more particles nucleated microvoids that contributed to the fracture of this alloy.

6.3.5 Summary

The Al-Li alloys and alloy 2219 exhibit two primary macroscopic fracture paths: shear and planar (normal to applied stress axis). The microscopic fracture modes observed were microvoid coalescence, intergranular delaminations or cracking, and brittle failure of constituent particles or inclusions. Shear-like macroscopic fracture patterns were usually associated with good ductility and microscopic failure by microvoid coalescence. Intergranular delaminations usually divided the crack, promoted plane stress conditions, and increased toughness or ductility (in orientations normal to the delamination plane). Brittle failure of constituent particles, observed in WL049 C(T) toughness specimens, was associated with planar fracture patterns and low toughness. An excellent discussion of these failure mechanisms in Al-Li alloys is provided by Rao and Ritchie.[15] Our observations on tensile failure modes are provided in Table 6.2. Fracture toughness observations are summarized in Table 6.3.

122

Figure 6.67(a)   Fracture surfaces, T-L orientation of WL049-T851, of C(T) toughness specimens at 4 K. Top-200X, bottom-500X.

123

Figure 6.67(b)   Top-1500X, bottom-7000X.

124
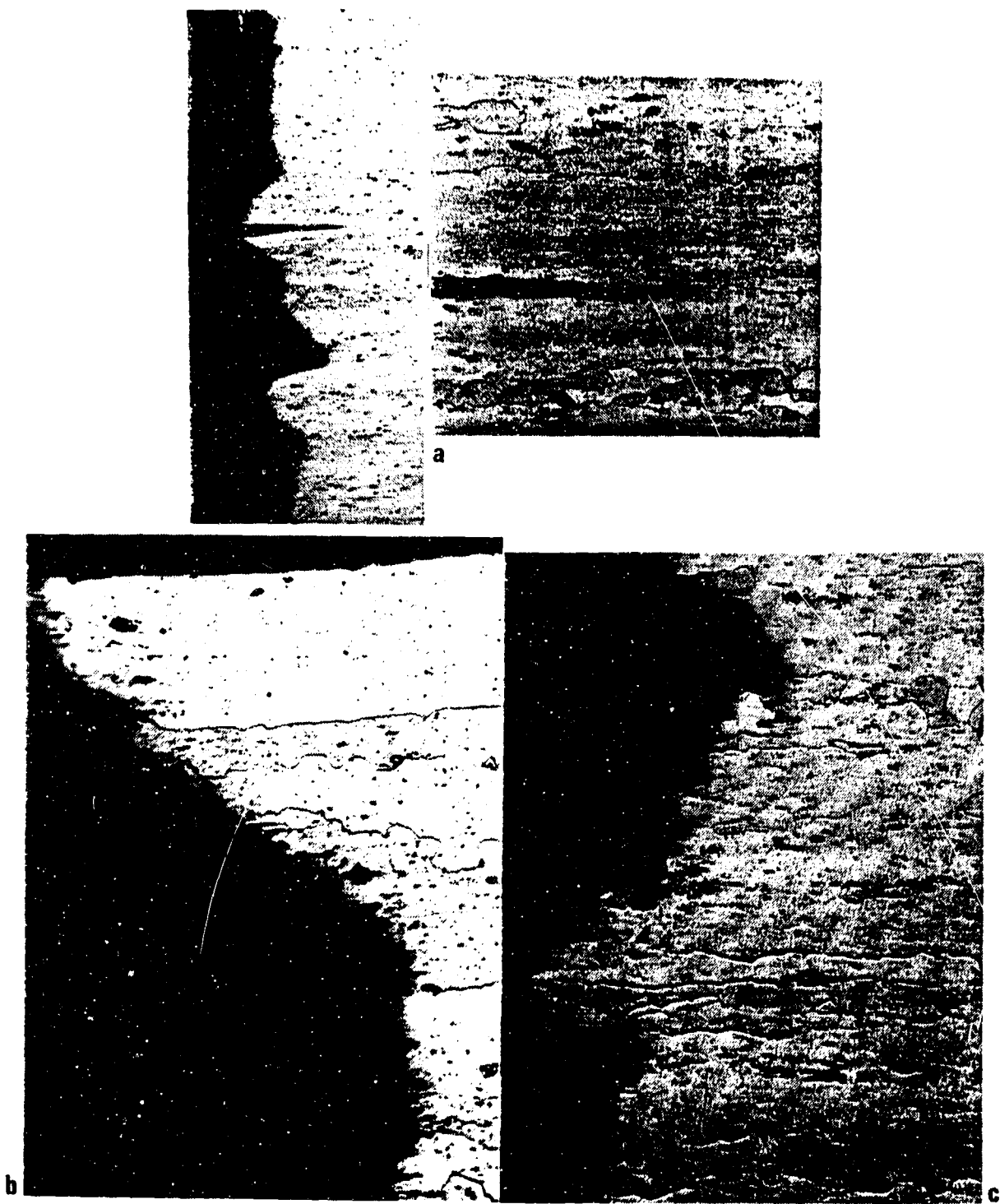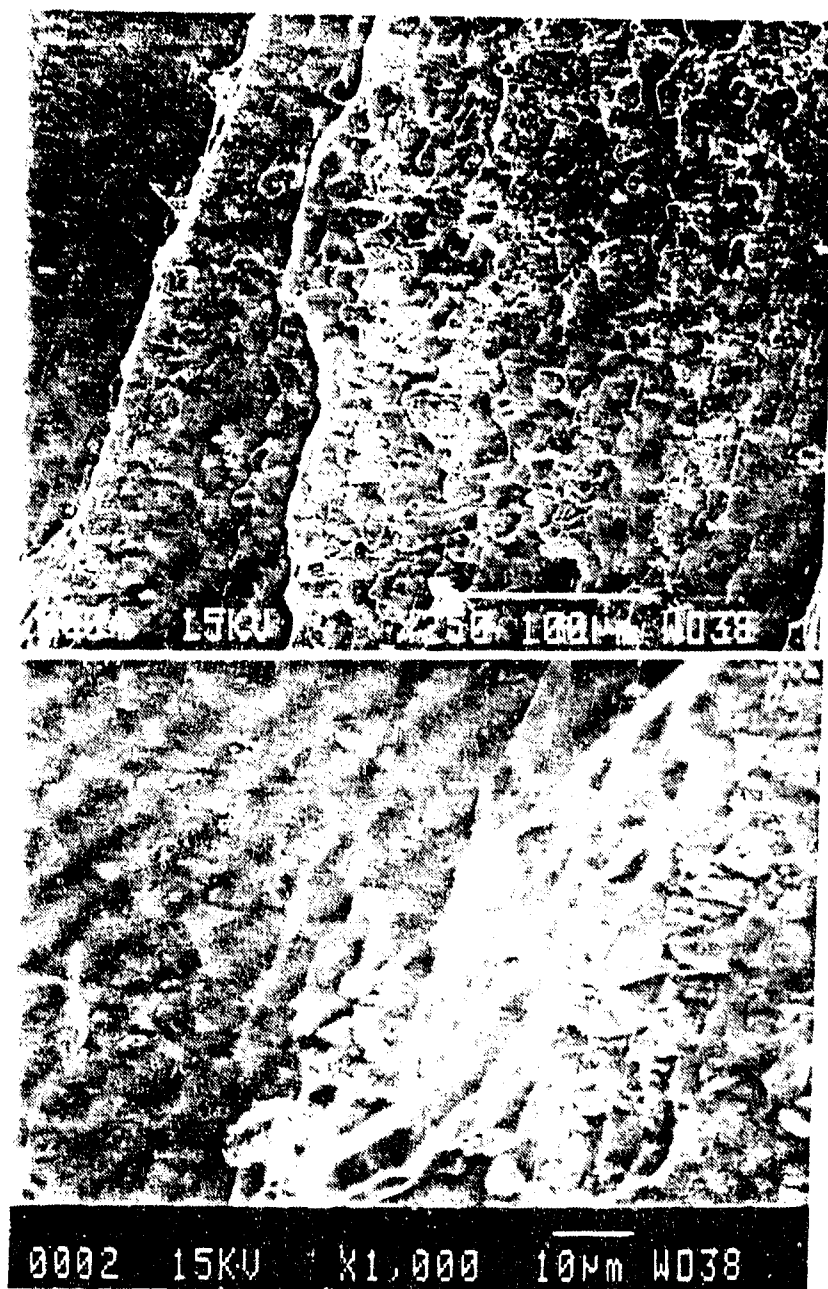
Figure 6.68(a)   Fracture surface, S-L orientation of WL049-T851,
of chevron-notched, short-rod specimen, tested at
4 K. Top-250X, bottom-1000X.

125
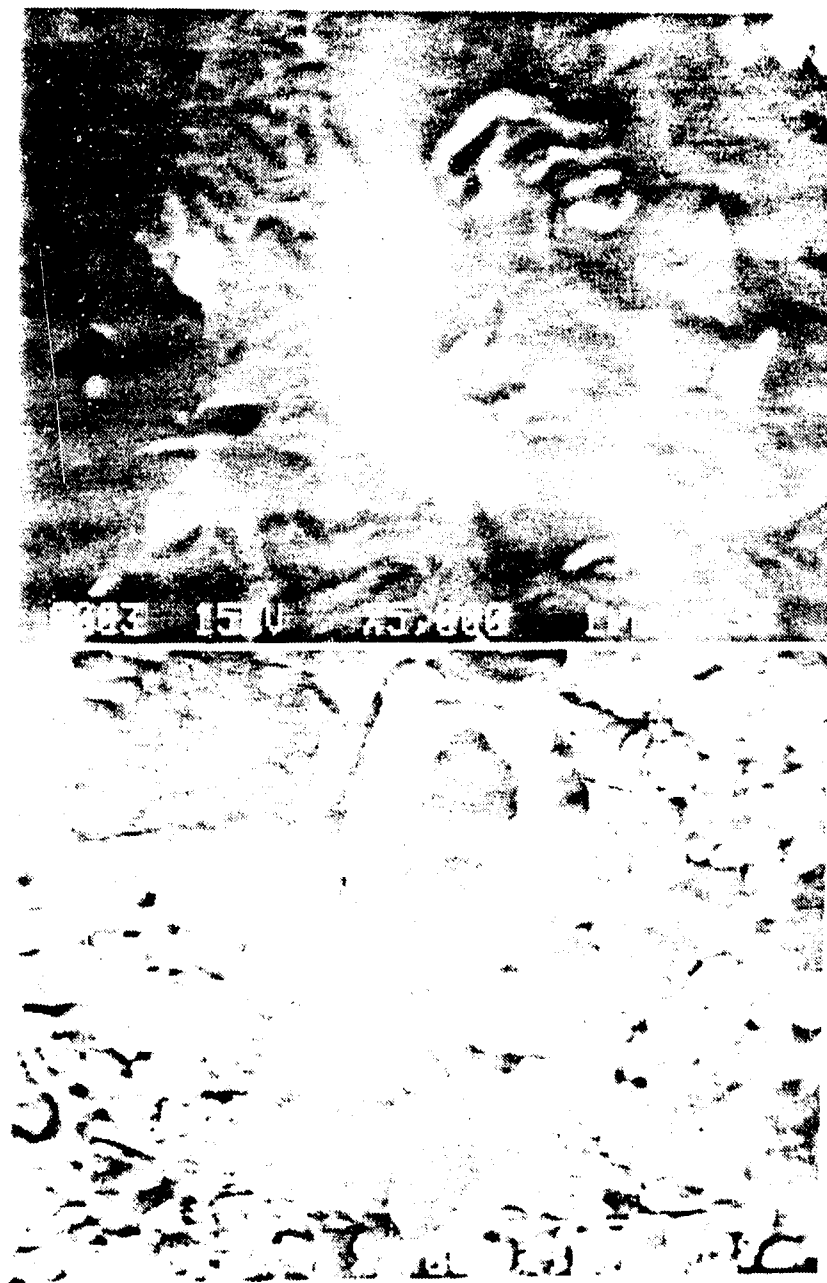
Figure 6.68(b)   Top-5000X, bottom-25000X.
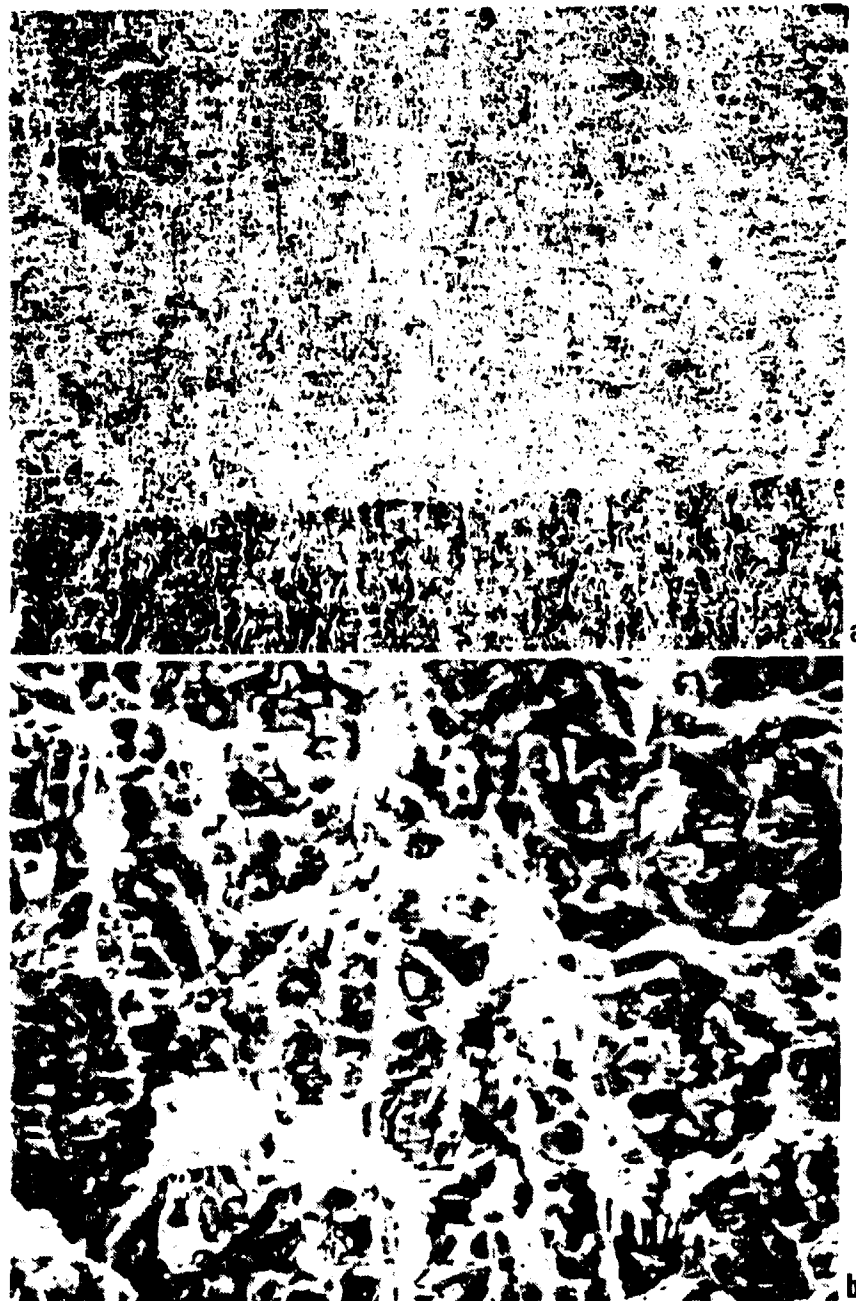
126

Figure 6.69   Fracture surface, T-L orientation of 2219-T37,
                     of C(T) toughness specimen tested at 4 K.
                     (a) top-30X; (b) bottom-500X.

7. GENERAL DISCUSSION AND SUMMARY

The two Al-Li alloys that are primary candidates for use in cryogenic tankage, 2090-T81 and WL049-T851, are compared in Table 7.1. The tensile yield and ultimate strengths of WL049-T851, compared to 2090-T81, are 10 to 20% higher at low temperatures. Conversely, the toughness in the T-L and L-T orientations of WL049-T851 is about 50% lower than that of 2090-T81. In the S-L and S-T orientation, WL049-T851 has much better toughness (about twice that of 2090-T81).

In cryogenic tankage, leak-before-break failure criteria are usually assumed. Leakage may be typically caused by crack growth in the T-S or L-S crack orientations (see Figure 5.3), since normal T-L or L-T crack orientations would have produced leakage during crack formation. Fracture toughness in the T-S or L-S orientations of 2090-T81 are expected to be strongly influenced by the tendency of the alloy to delaminate intergranularly. This delamination may result in arrest of cracks growing in the T-S or L-S orientations. Fracture toughness measurements in the T-S or L-S crack orientations were not included in this program. However, Rao, Yu, and Ritchie[14] report very limited data for the T-S orientation in 2090-T81. The fracture toughness of the T-S orientation is reported as 65 MPa√m (for specimens not meeting plane-strain thickness criteria). If bending versus tension loading considerations are not influential, this indicates that delaminations may indeed play an even larger role in affecting crack growth in these orientations. Allowable crack sizes, for linear-elastic, plane strain, are typically related to the ratio K_{Ic}^2/σ_y^2. Ratios of K_{Ic}^2/σ_y^2 for the two alloys are listed in Table 7.1, assuming T-L and L-T crack orientations. Alloy 2090-T81 is clearly superior under these premises.

However, under plane stress, expected to be encountered in thinner plate or sheet, the toughness normally scales with the strength. Under these conditions WL049-T851 is expected to be superior because of its higher tensile strength at low temperature. Thus, we recommend that a test program be undertaken to compare both alloys (WL049-T851 and 2090-T81) under test conditions more closely simulating operating conditions. This should include panel specimens with surface flaws, tested at cryogenic temperatures. In the primary test program, plate or sheet thicknesses should be chosen that most closely comply with current ALS design of cryogenic tanks. Variables that should be studied include panel thickness, crack aspect ratio and depth, and temperature.

Another method to assess the alloys of this program is to consider their strength-toughness relationship. At low temperatures, if the fracture mechanisms remain constant, most face-centered cubic alloys exhibit a linear, inverse dependence of fracture toughness (from J-integral measurements) on tensile yield strength. Graphs of toughness versus yield strength for each test temperature (295, 76, 4 K) are presented in Figures 7.1-7.3. To construct these figures, averages of T-L and L-T orientations of all tempers were used. Thus, the reader must consider that, perhaps, the figures are overly simplified.

128

TABLE 7.1

MECHANICAL-PROPERTY COMPARISON
RATIOS: WL049-T851/2090-T81

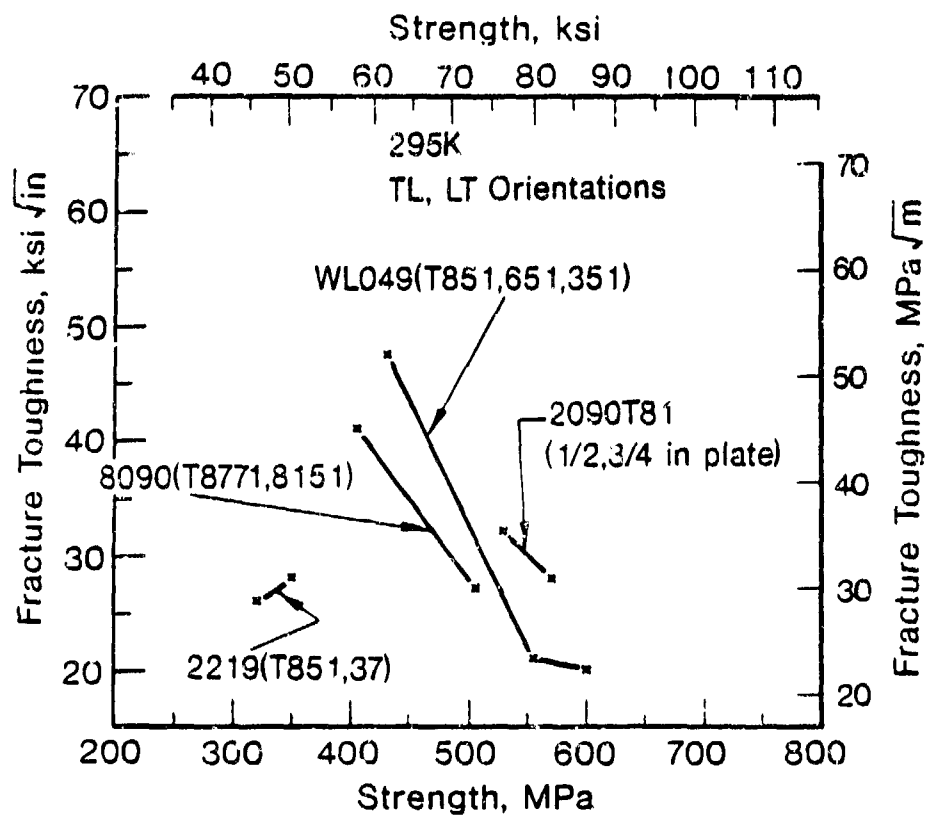| ORIENTATION	PROPERTY	TEST TEMPERATURES	
		4 K	295 K
T, L	TENSILE-ULTIMATE	1.10	1.10
	-YIELD	1.20	1.10
45°	TENSILE-ULTIMATE	1.10	1.10
	-YIELD	1.10	1.10
S	TENSILE-ULTIMATE	1.20	1.10
TL, LT	FRACTURE TOUGHNESS (CT)	0.60	0.50
SL, ST	FRACTURE TOUGHNESS (SB)	2.30	1.80
TL, LT	ALLOWABLE CRACK SIZE: K_{IC}^2/σ_Y^2	0.25	0.20

Figure 7.1   Strength-toughness relationships at 295 K for Al–Li alloys
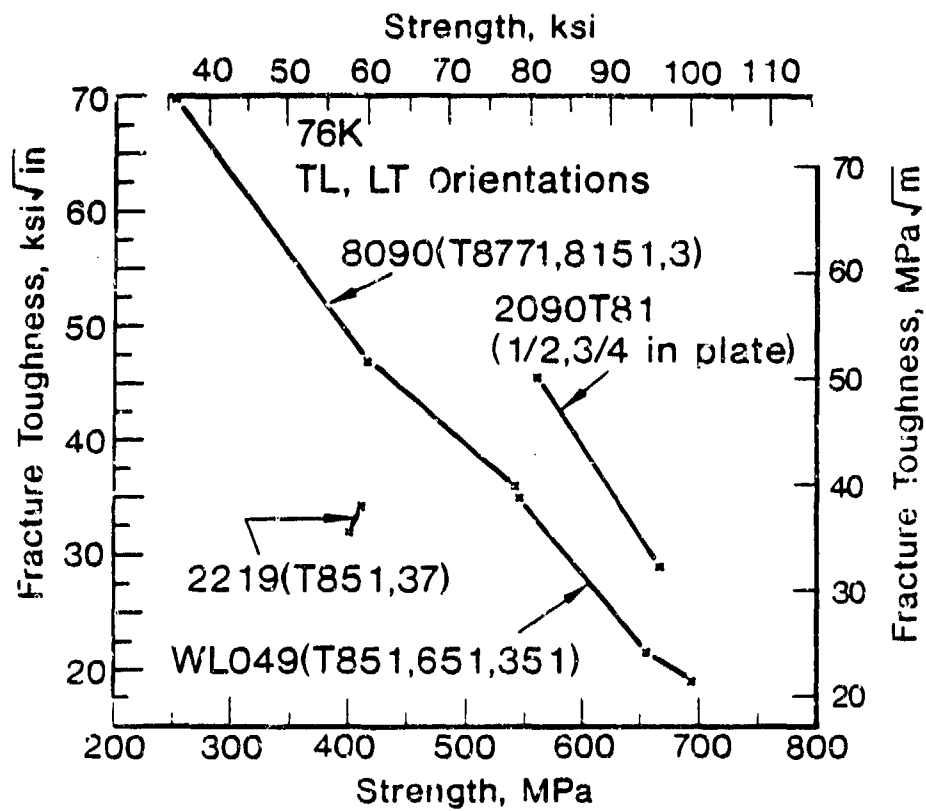and alloy 2219,T–L and L–T orientations.

Figure 7.2   Strength-toughness relationships at 76 K for Al-Li
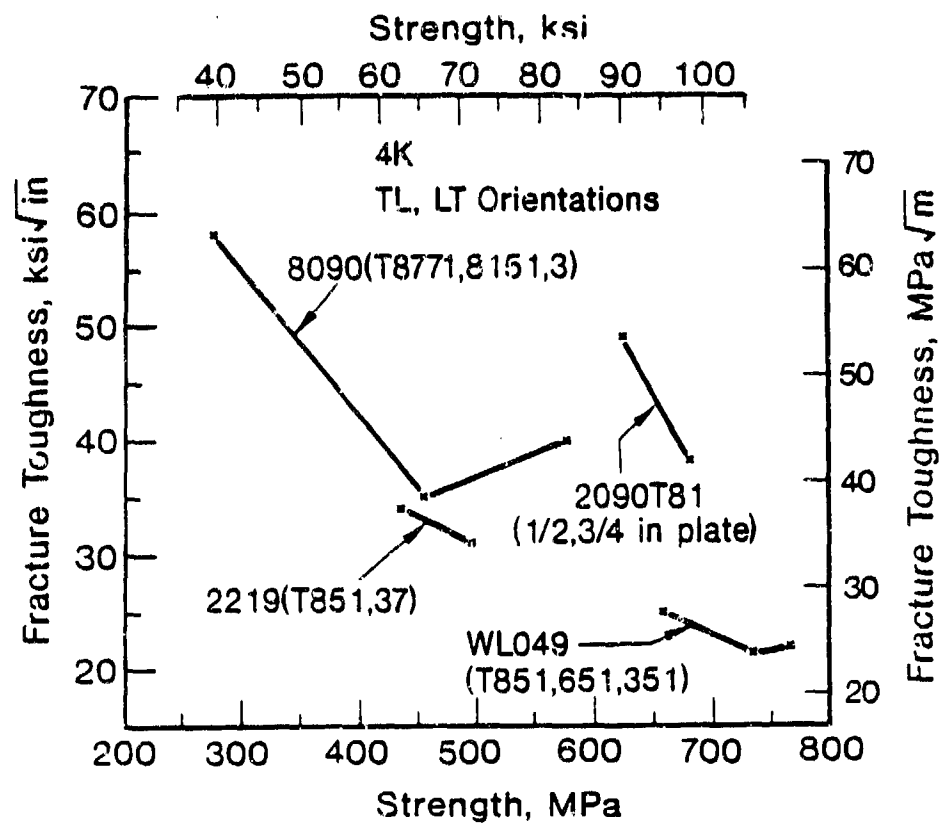   alloys and alloy 2219, T-L and L-T orientations.

Figure 7.3   Strength-toughness relationships at 4 K for Al-Li
alloys and alloy 2219 (T-L and L-T orientations).

132

To compare alloys at constant temperature, we use the empirical relationship: $K_{Ic}(J) \times \sigma_y$. We have called this term the Quality Index, since it represents an area under the $K_{Ic}(J)$ versus σ_y lines for each alloy. Efforts to improve the quality of alloys lead to an increased Quality Index; that is, movement of the $K_{Ic}(J)$-σ_y data points upward and/or to the right of the current trend lines. Plots of the average products of $K_{Ic}(J)$ versus σ_y for each alloy at each temperature are presented in Figure 7.4. Alloy 2090 shows the best combinations of strength and toughness, followed by 8090, then WL049, and, finally, 2219. Again, we emphasize that the data presented in Figure 7.4 represent averages of both T-L and L-T orientations and of all tempers that were indicated for each alloy in Figures 7.1 to 7.3. Also, the reader must consider that this relationship assumes equal design and service importance for σ_y and K_{Ic}. In many applications, including perhaps the ALS cryogenic tankage, strength is more important than toughness.

The fracture toughness was measured by two techniques: J-integral with compact-tension specimens and (2) chevron-notched, short bars. The results of both techniques are reported in Table 6.1, but only the results from J-integral tests (converted to linear-elastic-$K_{Ic}(J)$ values using Equation (3.1)) are included in Figures 7.1-7.4. It is of interest to compare the results from the two techniques; these results are presented for T-L and L-T specimen orientations in Figure 7.5. In this figure, ASTM E 813 represents the J-integral test procedure, ASTM E 1304 represents the chevron-notched, short-bar technique. In general, the chevron-notched, short-bar procedure results in higher toughness values than the J-integral technique. This trend is independent of test temperature. However, if extensive delaminations are present, then the J-integral results are higher. Comparison of the tests indicates large data scatter. Although there is a clear trend between the two toughness measurements, the band of data scatter is about ± 50%. This suggests that it is not practical to use, for example, the chevron-notched, short-bar test to produce fracture toughness data for Al-Li alloys at low temperature. Earlier, Brown [16] had conducted an extensive test series at room temperature to assess the relationship between the chevron-notched, short-bar and the compact-tension techniques for measurement of the fracture toughness of Al alloys. Alloys 7049, 7050, 7075, 7475, 2024, 2124, and 2419 in T6, T7, or T8 tempers were included in the program. Brown found good correlation between the two test methodologies, approximately ± 10% data scatter about a linear fit over the range of 20 to 40 MPa·/m at room temperature. A significant difference between our measurements and Brown's procedures was the thickness of the short-bar specimens. The specimen thickness of Brown's specimen was 25.4 mm, the thickness of our specimens was 12.7 mm. This suggests, combined with the fact that the chevron-notched, short-bar toughness results were higher, that plane-strain loading conditions were not present in our specimens. (Toughness is higher under plane stress conditions, compared to plane strain [17]). This is also discussed in a recent paper by Purtscher et al. [18]

Our comparison suggests the following: (1) In T-L and L-T orientations, plane-strain conditions may not be achieved in the chevron-notched, short-bar specimens; (2) delaminations play a significant role in producing a larger effective toughness; and (3) the two techniques produce sufficiently variant results that a claim of production of similar toughness data from each technique is not valid for Al-Li alloys.
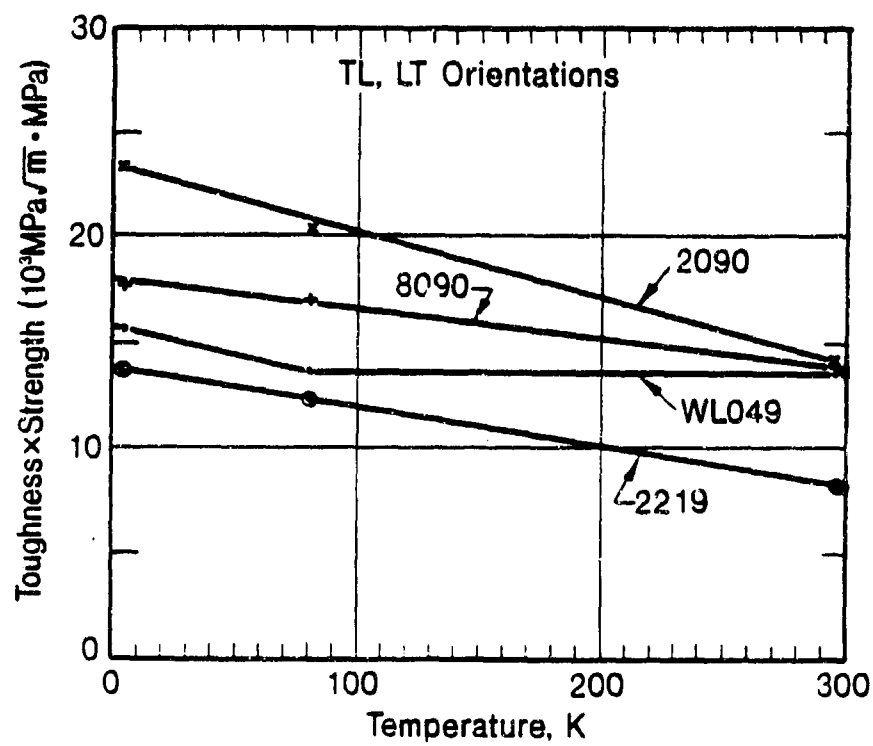
Figure 7.4   Temperature dependence of the product of σ_y x K_{Ic}(J)
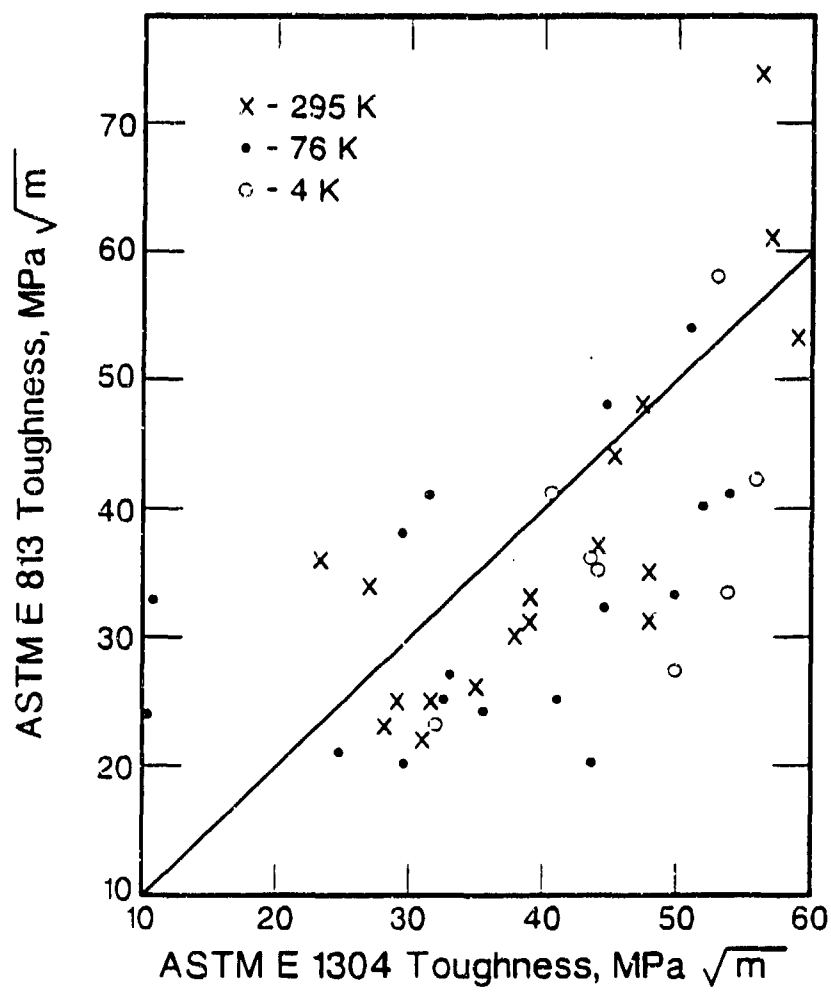for Al-Li alloys and alloy 2219.

Figure 7.5 Comparison of J-integral (ASTM E813) and chevron-notched,
short-bar (ASTM E1304) toughness data for Al alloys.

8. REFERENCES

1.(a) R. P. Reed, N. J. Simon, J. D. McColskey, J. R. Berger, C. N. McCowan, J. W. Bramford, E. S. Drexler, R. P. Walsh, Aluminum Alloys for Cryogenic Tanks: Oxygen Compatibility Vol. 1, AL-TR-90-063, Astronautics Lab (AFSC), Edwards AFB, CA (September, 1990).

1.(b) R. P. Reed, N. J. Simon, J. D. McColskey, J. R. Berger, C. N. McCowan, J. W. Bransford, E. S. Drexler, and R. P. Walsh, "Aluminum Alloys for Cryogenic Tanks: Oxygen Compatibility, Final Report: Vol. 2", AL-TR-90-063, Astronautics Lab (AFSC), Edwards AFB, CA (September, 1990).

2. N. J. Simon, E. S. Drexler, and R. P. Reed, "Review of Mechanical and Physical Properties of Al-Li Alloys and Alloy 2219," AL-TR-90-064, Astronautics Lab (AFSC), Edwards AFB, CA (September, 1990).

3. R. P. Reed, and R. P. Walsh, "Low Temperature Tensile Characteristics of Copper and Aluminum," Materials Studies for Magnetic Fusion Energy Applications at Low Temperatures, Vol. IX, NBSIR 86-3050, N.I.S.T., Boulder, CO (1986), pp 107-140.

4. ASTM Standard E 813-88, Standard Test Method for J^1_c, "A Measure of Fracture Toughness," American Society for Testing and Materials, Philadelphia, PA (1988).

5. ASTM Standard E 1304, "Standard Test Method for Plane-Strain (Chevron-Notch, Fracture Toughness of Metallic Materials," American Society for Testing and Materials, Philadelphia, PA (1988).

6. H. M. Ledbetter, unpublished data, National Institute of Standards and Technology, Boulder, CO (1990).

7. Metallic Materials and Elements for Aerospace Vehicle Structures, Vol. 1, Dept. of Defense, Washington, D.C., MIL-HDBK-5E (1987).

8. H. H. Wawra, "Einfluss der Werkstoffvorbehandlung auf die Elastizitatseigenschaften vol Aluminiumwerkstoffen", Aluminum 46, 805-811 (1970).

9. J. Glazer, S. L. Verzasconi, R. R. Sawtell, and J. W. Morris, "Mechanical Behavior of Aluminum-Lithium Alloys at Cryogenic Temperatures", Metall. Trans. A, 18A, 1695-1701 (1987).

10. R. G. Shewmon, "Diffusion", in Physical Metallurgy, J. Wiley & Sons, New York (1965), pp 365-383.

11. R. P. Reed and R. P. Walsh, "Tensile Strain-Rate Effects in Liquid Helium", Adv. Cry. Eng.-Maters. 34, 199-208 (1988).

12. R. P. Reed and N. J. Simon, "Discontinuous Yielding in Austenitic Steels at Low Temperatures", Cryogenic Materials 1988 (Shengang, China), eds. R. P. Reed, E. S. Xing, and E. W. Collings, International Cryogenic Materials Conference, Boulder, CO (1988), pp. 851-863.

13. P. T. Purtscher and E. S. Drexler, "Through-Thickness Mechanical Properties of High-Strength Aluminum Alloy Plates for Cryogenic Applications", Proceedings of TMS Symposium on "Lightweight Alloys for Aerospace Applications" (1991), submitted for publication.

14. K. T. V. Rao, W. Yu, and R. O. Ritchie, "Cryogenic Toughening of Commercial Aluminum-Lithium Alloys – Role of Delamination Toughening", Metall. Trans. A, 20A, 485-497 (1989).

15. K. T. V. Rao and R. O. Ritchie, "Mechanisms Influencing the Cryogenic Fracture-Toughness Behavior of Aluminum-Lithium Alloys", subm. to Acta Metall. (Nov. 1989), LBL Report 28125, U.Cal. Berkeley, CA (1989).

16. K. R. Brown, "The Use of the Chevron-Notched Short-Bar Specimen for Plane Strain Toughness Determinations in Aluminum Alloys", ASTM STP 855, Am. Soc. Test. Mats., Philadelphia, PA (1984).

17. R. T. Read and R. P. Reed, "Effects of Specimen Thickness on Fracture Toughness of an Aluminum Alloy", Int. J. Fracture 13, 201-213 (1977).

18. P. T. Purtscher, J. D. McColskey, and E. S. Drexler, "Comparison of Fracture Toughness Test Standards, ASTM E 813 and E 1304, for Aluminum-Lithium Alloys", to be published as ASTM STP Am. Soc. Test. Mats., Philadelphia, PA.